INFN Istituto Nazionale di Fisica Nucleare
LABORATORI NAZIONALI DI FRASCATI
SIS – Pubblicazioni

LNF–05/ 10 (Thesis)
June 1, 2005

Università degli Studi di Firenze

Facoltà di Scienze Matematiche Fisiche e Naturali
Dipartimento di Fisica

DAΦNE LATTICE WITH TWO LOW–BETA INTERACTION REGIONS

Tesi di Dottorato di

Gabriele Benedetti

Prof. Mario Calvetti, supervisore

Dott. Caterina Biscari, co-supervisore

Firenze, 2005

Abstract

This doctoral thesis is focused on the development of the DAΦNE lattice to collide in the second interaction point where the FINUDA detector was installed in 2003. Modelling of the second interaction region and of the modified wigglers are described in detail. The constraints to be fulfilled by the lattice and the agreement between the model and the beam measurements are discussed. A model dependent technique for beam based alignment has been implemented for the main rings. The developed procedure and its results are presented.

Contents

Chapter 1

Introduction

The Double Annular Φ-factory for Nice Experiments (DAΦNE) is an electron-positron circular collider at high luminosity working at the energy of the Φ mass resonance (1.020 GeV) [47, 48]. The design of the collider is based on two high current symmetric rings, 97 metres long, crossing at a horizontal angle in two interaction regions 10 metres long (the *low beta insertions*), which alternatively housedifferent experiments. The lattice of the rings consists of four achromatic arcs, each housing a 2 metres long, 1.8 T normal conducting wiggler magnet which doubles up the synchrotron radiation emitted in dipoles.

The major physics motivation for the construction of DAΦNE is the observation of direct CP-violation in K_L decays, i.e. the measurement of the parameter ϵ'/ϵ with accuracy in 10^{-4} range by the KLOE detector [21]. The other experiments which have been using the DAΦNE luminosity are FINUDA [20], for hypernuclear spectroscopy, and DEAR [19], for exotic atoms physics.

The KLOE detector, with its solenoidal field, has been installed on the first interaction region (IR1) since 1999. The second interaction region (IR2) has been shared between FINUDA, which has also a solenoidal field, and DEAR, which has external targets around the vacuum chamber, non interfering with the ring optics.

Two experiments can be installed contemporaneously in DAΦNE, but since the commissioning period of the collider (1998) it was clear that optimizing the luminosity in two interaction points was critical and the collider has always worked for one experiment per time, keeping the beam trajectories vertically separated at the non-colliding interaction point.

Many are the effects that can limit the luminosity in a multibunch collider: nonlinearities in the magnetic fields, parasitic crossings between the opposite beams, instability thresholds of the currents etc.

In the original design one key point was the crossing angle at the interaction point. DAΦNE, together with KEK-B, is the first collider originally designed with a horizontal crossing angle that allows to store up to 120 bunches per ring avoiding parasitic crossings between the outgoing bunches after collision and the incoming bunches of the opposing beam in the interaction region. However the crossing angle θ_x must be small enough to avoid synchro-betatron resonances (this condition is generally expressed by the Piwinski angle ϕ that must be kept small [35]: i.e. $\phi = \theta_x \cdot \sigma_x^*/\sigma_z \ll 1$, where σ_x^* and σ_z are the horizontal and longitudinal beam sizes at the collision point). The design value of the crossing angle chosen to fit this condition was $\theta = \pm 12.5$ mrad.

During the first years of operation, it has become clear that with respect to the original design the crossing angle could be increased and the beta functions at the interaction point squeezed with benefit for the parasitic crossing and the increase of luminosity [11]. In 2003 a modified design of the first interaction region (IR1) has been then realized, changing the original FDF quadrupole triplet scheme of the low beta insertion in a DF doublet which is more flexible to vary the crossing angle in a wider range and to decrease the beta functions.

Another specific feature of DAΦNE from the point of view of the lattice are the wigglers, which in a low-medium energy collider as a Φ-factory are needed to shorten

the damping times of transverse and longitudinal oscillations and to raise the instability thresholds. The operation of the collider showed that wiggler magnets were sources of strong nonlinearities (sextupolar, octupolar and higher order field components). The evidence of those effects was pointed out experimentally observing the betatron tune shifts when the beam orbit along the wigglers was varied with horizontal closed bumps [33]. Simulations confirmed that such nonlinearities in wigglers were responsible of limitations both in the dynamic aperture and in the energy acceptance, i.e. in the transverse area where the particle motion is stable and the energy range within which a particle is not lost from the beam. Such effects resulted in a reduction of the beam lifetime and luminosity performances.

In order to correct the non linear components in the wigglers, in 2003 the surface of the wiggler poles has been modified in a curved shape which generate a flat behaviour of the magnetic field in a larger range along the horizontal coordinate [37].

The work discussed in this PhD thesis concerns the study and the development of the DAΦNE main ring lattice for two experiments (KLOE and FINUDA) I have carried out from 2002 to 2004 at DAΦNE, with special attention to the linear optics model.

After a presentation of the general design of the collider, a discussion about the parameters that determine the luminosity performances in DAΦNE is introduced (Chapters 2 and 3). My major activity has been the update of the model that describes the DAΦNE main rings with the optics program MAD developed at CERN [26]. In this framework I have completely modelled the second interaction region, where the FINUDA experiment was installed in 2003, and the modified wigglers from the magnetic measurements of the field performed on each magnetic element (Chapter 4). With this model I calculated the new ring optics for FINUDA with the required parameters: lower emittance (from 0.8 to $0.4{\cdot}10^{-6}$ m·rad), lower vertical beta function at the interaction point (from 4 to about 2 cm), optimized betatron phase advance between the magnetic elements

etc. (Chapter 5).

The new DAΦNE model has been validated by comparing its predictions with the beam measurements both for the linear optics (beta functions, betatron tunes, dispersion function, closed orbits) and for nonlinear effects (chromaticity, dynamic aperture etc.). In the framework of this optics study, I have also implemented a beam based alignment procedure for the quadrupoles magnets (Chapter 7). Thanks to such model dependent measurements we were able to easily find large misalignments of the quadrupoles and also to check the correct operation of the other magnets in the first days of running after a long machine shutdown.

Chapter 2

General design of the Φ-factory

The layout of the DAΦNE complex is shown in Fig. 2.1 and the parameters of the accelerator are listed in Table 2.1. In this chapter the main components of the factory are presented and the design of the collision rings on which this thesis is focused is described in more detail.

2.1 DAΦNE

The luminosity in a circular collider is given by:

$$\mathcal{L} = f_{coll}\frac{N_b^+ N_b^-}{A}; \tag{2.1}$$

where $f_{coll} = f_{rev}n_b$ is the frequency of collisions with n_b the number of bunches, N_b^+ and N_b^- the number of particles of the colliding bunches and A the overlap function. The transverse area A and the number of particles per bunch are determined by the characteristics of the collider. Eq. (2.1) shows that to enhance the luminosity, in addition to shrink A and increase N_b as much as possible, the frequency of collisions f_{coll} can be raised by increasing the number of bunches n_b per beam. In DAΦNE it is possible to store

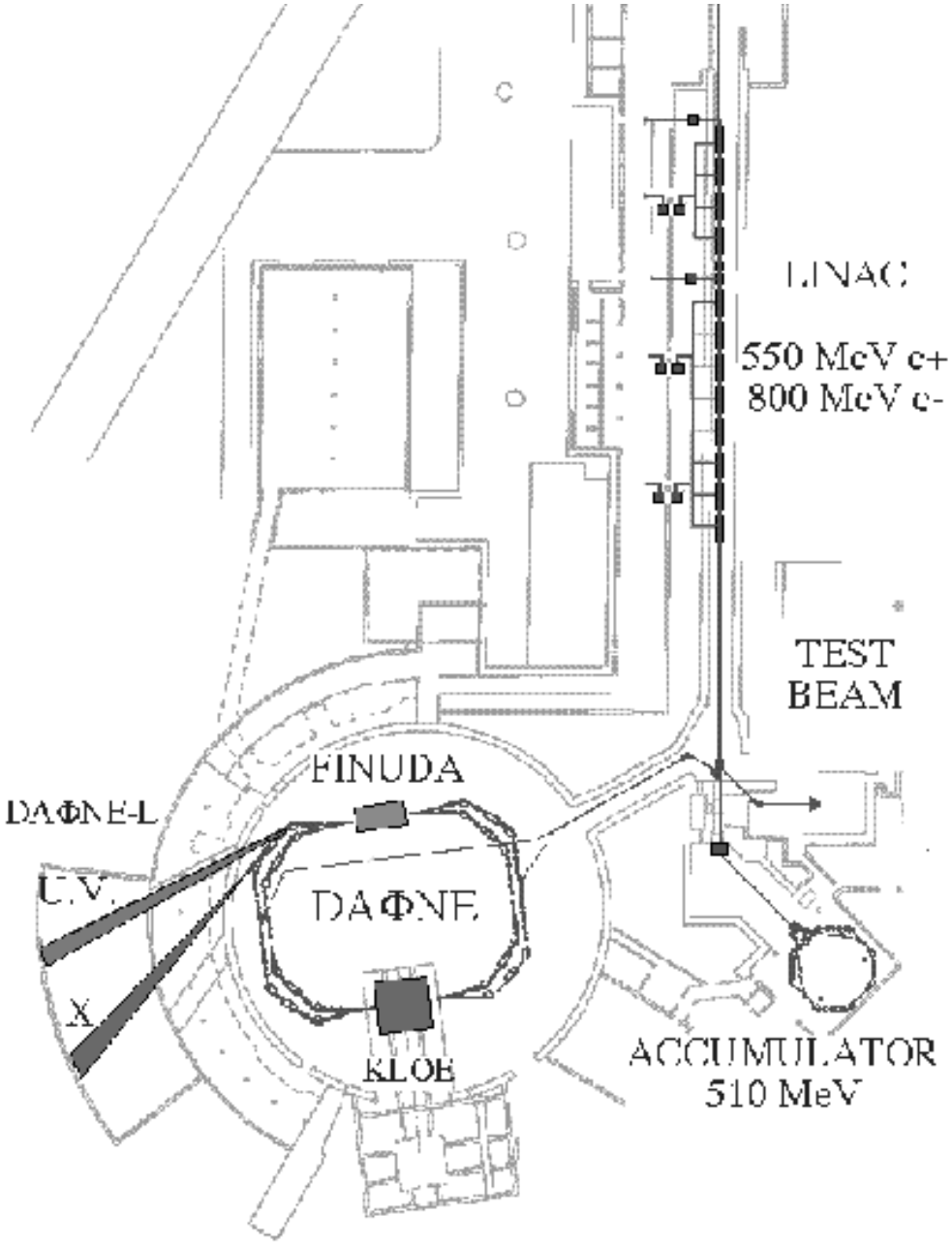

Figure 2.1: Layout of the DAΦNE complex.

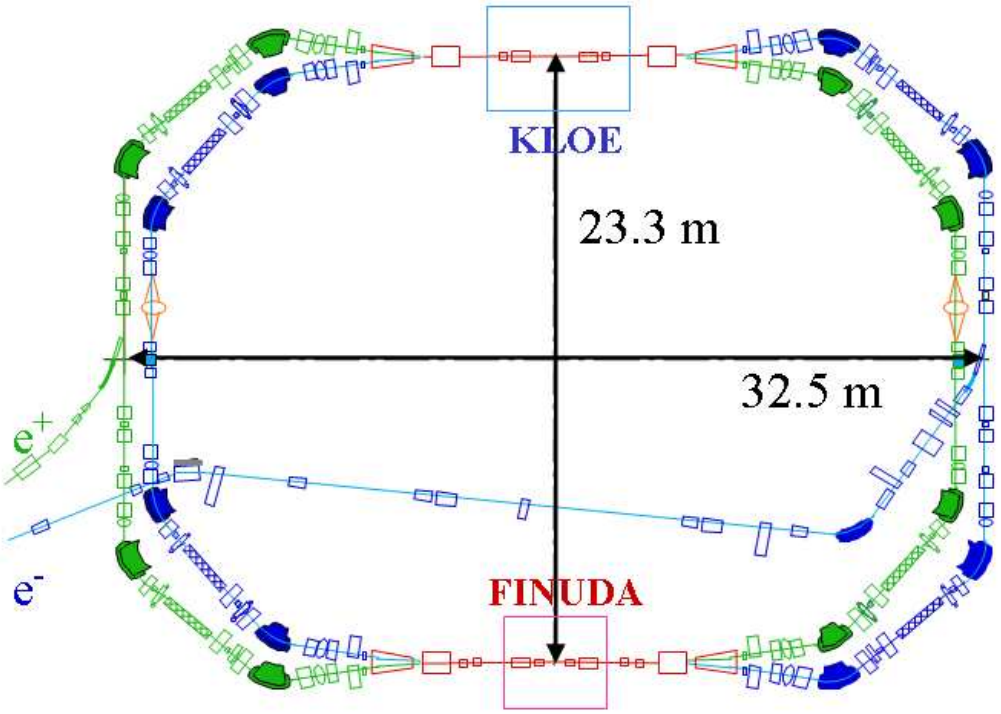

Figure 2.2: Layout of the DAΦNE main rings.

up to 120 bunches without increasing the number of crossing points, because electrons and positrons circulate in two separated rings, laying on the same horizontal plane and sharing two interaction regions where the experimental detectors are installed.

The layout of the DAΦNE main rings is shown in Fig. 2.2: two storage rings 97 metres long, one for electrons and the other for positrons, crossing each other in two interaction regions 10 metres long, where the opposing beams travel in the same vacuum chamber. Each ring has an outer section, called *Long*, and one inner section, *Short*, both consisting of two quasi achromatic arcs and a straight section. The four sections (Long and Short) are connected to the interaction regions through four splitter magnets. A challenging feature of the DAΦNE design is that there is no symmetry in the magnetic structure all along the rings: this results in a more complicated handling of the optics functions. In order to have the maximum flexibility in the set up of the ring optics, each of the 43

quadrupoles per ring is individually powered.

The position of the beam along the rings is measured with 47 beam position monitors (BPM) and can be steered and controlled with 31 horizontal and vertical corrector dipoles per ring.

2.1.1 Definition of the coordinate system

Before presenting the design of the main rings of DAΦNE in more detail, the coordinate system used throughout this thesis to describe the particle motion is introduced. The position of a particle along a ring is located by means of the azimuth coordinate s (Fig. 2.3). A local 3-dimentional coordinate system (x, y, z) is used to identify the particle position with respect to the ideal reference. The transverse coordinates x and y measure the horizontal and vertical displacement from the ideal trajectory passing through the center of perfectly aligned quadrupole magnets, while the longitudinal coordinate $z = s - v_0 t$,

Parameter		Design	Present	
Beam energy	E_0	510.0		MeV
Peak luminosity	$\mathcal{L}_{max}$	$5 \cdot 10^{32}$	$1.3 \cdot 10^{32}$	$cm^{-2}s^{-1}$
Ring length	L	97.68		m
Emittance	ϵ_x/ϵ_y	1.0/0.01	0.4/0.002	$mm \cdot mrad$
Beta function at IP1	β_x^*/β_y^*	4.5/0.045	2.0/0.018	m
Beta function at IP2	β_x^*/β_y^*	4.5/0.045	2.0/0.025	m
Beam-beam tune-shift	ξ_x/ξ_y	0.040/0.040	0.020/0.016	
RF frequency	f_{RF}	368.263		MHz
Harmonic number	h	120		
Revolution frequency	f_{rev}	3.0688		MHz
Particle per bunch	N_b	$8 \cdot 10^{10}$	$4 \cdot 10^{10}$	
Natural energy spread	σ_ε/E_0	$3.96 \cdot 10^{-4}$		
Natural bunch length	σ_s	3.0	1.7	cm
Energy loss	U_0	9.3		$keV/turn$
Damping time	τ_ε/τ_x	17.8/36.0		ms
RF voltage	V_{RF}	250		kV

Table 2.1: Parameters of the DAΦNE collider

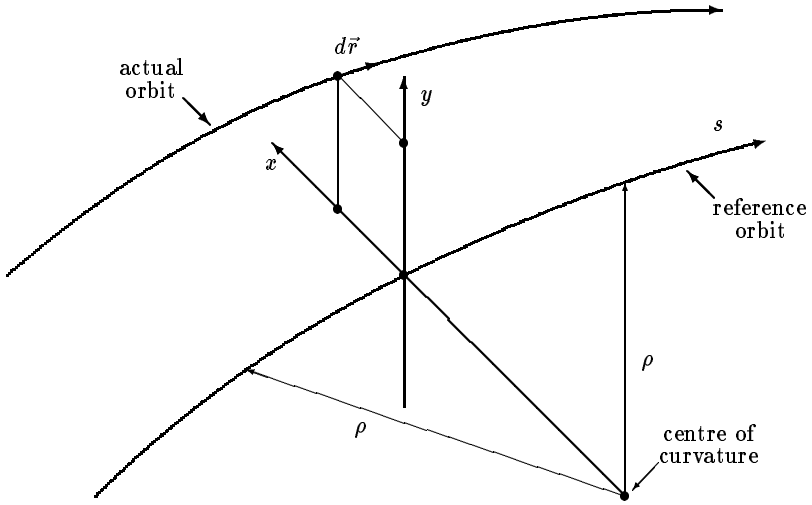

Figure 2.3: The coordinate system employed to describe the particle motion.

where v_0 is the velocity of a particle with nominal energy and t is the time, locates the longitudinal position with respect to an ideal particle with nominal energy E_0 at the bunch centre. Deviations of particle energy E with respect to E_0 are measured with the coordinate $\delta = (E - E_0)/E_0$ and variations in slope of particle trajectories are denoted as $x' = dx/ds$ and $y' = dy/ds$.

The beam transport between two positions in the ring is expressed in matrix notation as:

$$\begin{pmatrix} x \\ x' \\ y \\ y' \\ z \\ \delta \end{pmatrix}_{out} = \begin{pmatrix} R_{11} & R_{12} & R_{13} & R_{14} & R_{15} & R_{16} \\ R_{21} & R_{22} & R_{23} & R_{24} & R_{25} & R_{26} \\ R_{31} & R_{32} & R_{33} & R_{34} & R_{35} & R_{36} \\ R_{41} & R_{42} & R_{43} & R_{44} & R_{45} & R_{46} \\ R_{51} & R_{52} & R_{53} & R_{54} & R_{55} & R_{56} \\ R_{61} & R_{62} & R_{63} & R_{64} & R_{65} & R_{66} \end{pmatrix} \begin{pmatrix} x \\ x' \\ y \\ y' \\ z \\ \delta \end{pmatrix}_{in} ; \tag{2.2}$$

where "in" and "out" stand for incoming and outgoing beam through the lattice section of interest. The values of the R_{ij} matrix elements can be expressed in terms of the lattice

Twiss functions (the betatron functions $\beta_x(s)$, $\beta_y(s)$, the dispersion function $D_x(s)$ and their derivatives) as in every optics textbook (see for example [22, 49]).

2.1.2 Interaction regions

The interaction regions of DAΦNE (referred to as IR1 and IR2) are two sections 10 metres long with a magnetic structure symmetric with respect to the *interaction point* (IP1 and IP2) designed to produce low beta-functions at the IPs, for this reason the sections where experiments are housed are called *low-beta insertions*. The electron and positron beams travel off axis in the vacuum chamber of the interaction regions with opposite direction and they cross each other with a design angle in the horizontal plane of ±12.5 mrad (Fig. 2.5), at the centre of the IR.

The strong focusing is provided by a couple of quadrupole doublets located symmetrically with respect to the interaction point. In the free space between the interaction point and the closest D quadrupole[1] the vertical beta-function is given by:

$$\beta_y \approx \frac{d^2}{\beta_y^*}; \tag{2.3}$$

where β_y^* is the vertical beta-function at the interaction point and $d = f_y$ is the distance between the interaction point and the closest quadrupole equal to the quadrupole focal length. Large beta-functions in the lattice result in large chromatic aberrations that must be carefully corrected using sextupoles magnets located along the ring. Particles with different energies are focused differently since the strength of the quadrupoles depends on the particle momentum. The *natural chromaticity* (chromaticity only from quadrupoles)

[1] F and D refer to as focusing and defocusing quadrupoles in the horizontal plane and the converse in the vertical plane.

of a magnetic lattice is expressed as:

$$\xi = \frac{1}{4\pi} \int \beta(s) K(s) ds; \tag{2.4}$$

where $K(s)$ is the strength (normalized gradient) of the quadrupoles:

$$K = \frac{1}{B\rho} \frac{\partial B}{\partial y}; \tag{2.5}$$

and $B\rho = p/e$ is the magnetic rigidity of the particle. The drawback of the correction of chromaticity is the reduction in the *dynamic aperture*[2] of the ring due to the nonlinearities in the particle motion introduced by the sextupoles.

With typical values for DAΦNE of $\beta_y^* \approx 2$ cm (higher than the bunch length σ_z as explained in Chapter 3) and a maximum β_y of the order of 50 m compatible with a reasonable chromaticity, the distance between the IP and the closest D quadrupole comes out to be 1 m, meaning that the low-beta quadrupole doublets must be housed inside the experimental detector. The only way to fit quadrupoles inside a detector was to use permanent quadrupole magnets (otherwise supeconducting technology should be used).

In DAΦNE when the beams are colliding in one interaction point, they are separated with a vertical closed bump of the orbit in the opposite interaction point.

The two interaction regions of the experiments KLOE and FINUDA are presented below. KLOE has been in operation since 1999, while FINUDA has completed the first phase of its program in a six month run during 2003.

Studies and tests carried out in 2001 and 2002 [8, 9, 11] lead to the decision to modify the design of the interaction regions to a new quadrupole configuration that allows a better flexibility for the collider operation. After a six month stop in 2003, the new interaction

[2]The 2-dimensional dynamic aperture is defined as the area in the transverse space (x, y) where the particle motion is stable. Generally it is calculated by tracking codes as the maximum x and y values that can have a particle without being lost after a "large" number of turns.

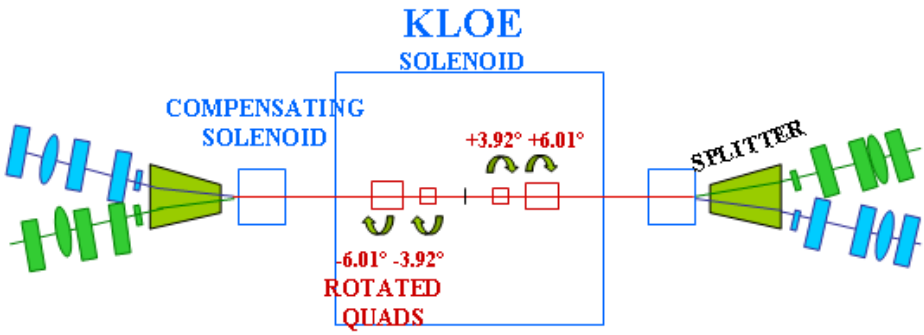

Figure 2.4: Schematic view of the present KLOE interaction region (IR1).

regions were installed and a new beam optics has been designed and tested first for the FINUDA run with good achievements, then in 2004 for KLOE with further very good performances.

IR1: the KLOE interaction region

The KLOE interaction region is a low-beta insertion with two permanent quadrupoles doublets symmetric with respect to the IP housed inside the experimental detector. The KLOE superconducting solenoid magnet is 0.6 Tesla × 4 metres. Such a magnetic field is a strong perturbation to the particle motion, because the integrated field of the solenoid (2.4 Tm) is of the same order of magnitude of the magnetic rigidity $B\rho = 1.7$ Tm of an electron with an energy of 510 MeV. The effect of the solenoid field is focusing and coupling the betatron motions tilting the transverse section of the beam by an angle proportional to the integral of the field along the particle trajectory [4] ($\theta_{rot} \simeq 40°$):

$$\theta_{rot} = \frac{1}{2B\rho} \int_{solen} B_z(s) ds \tag{2.6}$$

The correction system of the coupling is realized zeroing the rotation of the transverse beam section at the interaction point and outside the interaction region by compensating

the integrated field with two solenoids of 1.2 Tesla × 1 metre (*Compensators*) whose field is opposite the KLOE one. The compensating magnets are installed between the detector and the splitters. Finally each quadrupole is rotated around its longitudinal axis following the rotation of the beam.

The present KLOE interaction region is based on a DF quadrupole doublet (the former one being based on a FDF focusing lattice). Its novel features are:

- the inner F quadrupole was removed and the third one strengthened by 50% installing beside another F permanent quadrupole;

- stepping motors remotely controlled that can vary the quadrupole roll angles in a ±45° range;

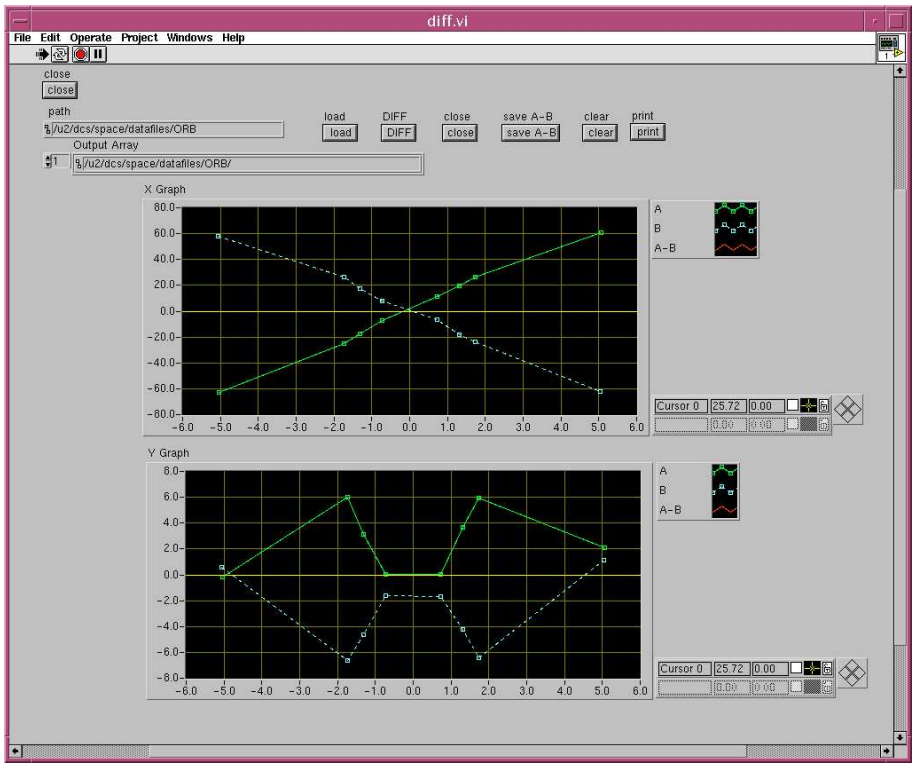

Figure 2.5: Horizontal and vertical trajectories of the electron and positron beams along IR1 as they are shown by the DAΦNE control system, for beams colliding in IP1.

- two printed circuit (PCB) quadrupoles to measure beta-functions near IP1.

This modified lattice has several advantages concerning the optics that will be discussed in Chapter 5, the more important being the wider range within which the horizontal crossing angle at IP can be varied, moreover the new rotation equipment allows to correct the betatron coupling for different values of the KLOE solenoidal field.

The beam trajectories along IR1 are controlled adjusting the currents of the splitter magnets and using four dipole correctors outside the interaction region. The position of the beams is measured with six beam position monitors located symmetrically with respect to IP1. In Fig. 2.5 the horizontal and vertical position measurements at the monitors are shown as they are visualized by the DAΦNE control system.

When the beams are colliding in FINUDA, the beam trajectories are vertically separated at IP1, the KLOE solenoid is turned off, the roll angles of the permanent quadrupoles are rotated to zero and IR1 is still a low-beta.

The beta functions and the beam trajectories in IR1 are described in Chapter 5.

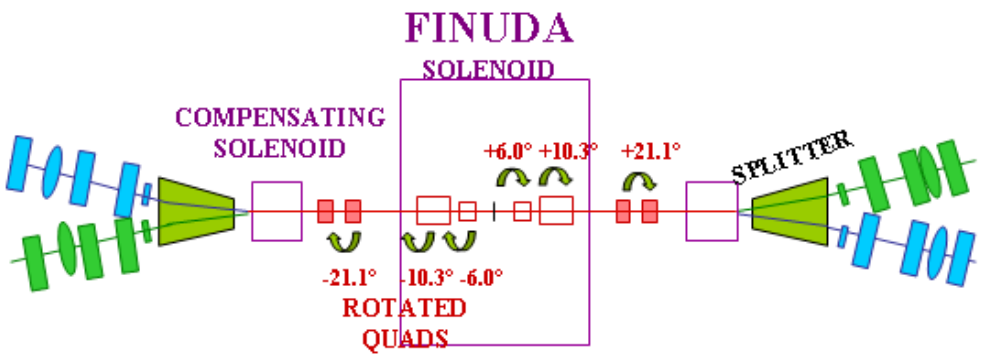

Figure 2.6: Schematic view of the FINUDA interaction region.

IR2: the FINUDA interaction region

The set up of the second interaction region for FINUDA was realized in 2003. The FINUDA detector is only 2 metres long, so that two further electromagnetic quadrupole doublets are positioned outside the detector (see Fig. 2.6). The same correction system as KLOE (compensating solenoids and rotated quadrupoles) is employed for the coupling arising from the experimental solenoid that has shorter dimensions but a stronger field (1.0 T $\times$ 2.4 m) than the KLOE one. The quadrupoles (both the permanent and the electromagnetic ones) are rotated with stepped motors.

During the KLOE run, the FINUDA apparatus with the four permanent quadrupoles is rolled off and replaced with a simple straight pipe line: in this case the beta functions are "detuned" by using the other four electromagnetic quadrupoles and the second interaction region is not a low-beta insertion anymore.

The beta functions and the beam trajectories in IR2 are described in Chapter 5.

The modelling of the FINUDA interaction region for the MAD program [26, 30] is the subject of Chapter 4.

2.1.3 Arc cells and dispersion function

The structure of each DAΦNE collision ring consists of four achromatic arcs[3]. Each arc is delimited by two bending magnets and houses a 1.8 T wiggler magnet, three quadrupoles, two sextupoles to correct the chromaticity of the ring, two dipole correctors and one skew quadrupole.

The wiggler magnet is aimed at varying the horizontal emittance and increasing the synchrotron radiation emission; this effect is needed in a low energy ring as DAΦNE, where the betatron transverse damping time is $\tau_x \approx 100000$ turns with the wigglers turned on.

[3] An achromatic cell is a section where both the dispersion function and its derivative vanish at the ends. This lattice can be obtained with a proper combination of the bending magnets and the quadrupoles.

Particles in a bunch with different energy are bent differently by dipoles because the bend angle of a magnet depends on the particle momentum. The orbit displacement for a theorical energy deviation $\delta = \Delta E/E_0 = 1$ is the *dispersion function* $D(s)$. The arc cells are the sections of the ring where the dispersion function is different from zero. Many important parameters of the ring are determined by the dispersion function.

The *natural beam emittance*[4] is generated by the emission of synchrotron radiation in a region with non-zero dispersion. The dependence from the dispersion function is expressed by the equation [32]:

$$\epsilon_x = C_q \frac{\gamma^2 \langle \mathcal{H}/|\rho|^3 \rangle}{\mathcal{J}_x \langle 1/\rho^2 \rangle}; \tag{2.7}$$

where $C_q = 3.83 \cdot 10^{-13}$ m, γ is the particle energy in units of the rest mass, $1/\rho$ is the orbit curvature, $\langle ... \rangle$ stands for the average all over the ring, $\mathcal{J}_x$ is the horizontal damping partition number and the $\mathcal{H}$-function depends on the lattice design as:

$$\mathcal{H} = \gamma_x D_x^2 + 2\alpha_x D_x D_x' + \beta_x {D_x'}^2; \tag{2.8}$$

with β_x, α_x and γ_x the horizontal Twiss parameters. In straight sections $\mathcal{H}$ is an invariant, while it is not invariant through dipoles.

Another important parameter depending on the dispersion is the path lengthening of a particle motion due to the beam energy spread, which is measured by the *momentum compaction* factor:

$$\alpha_c = \frac{1}{L} \oint \frac{D_x(s) ds}{\rho}; \tag{2.9}$$

[4]The emittance is a beam parameter expressing the average amplitude and divergence of the particle motion and, together with the energy spread, determines the transverse dimension of the beam:

$$\sigma_x = \sqrt{\epsilon_x \beta_x + (D_x \delta)^2}.$$

In flat rings there is no vertical dispersion and the vertical emittance ϵ_y is generated by the betatron coupling.

where L is the length of the ring. The natural bunch length is proportional to α_c according to (see for instance [22, 49]):

$$\alpha_c = \frac{2\pi c}{f_{rev}} \sqrt{\frac{2\pi|\alpha_c|E_0}{heV_{cav}\cos\phi_s}} \frac{\sigma_\epsilon}{E_0}; \tag{2.10}$$

where $V_{cav}\cos\phi_s$ is the RF voltage slope.

The technique to modulate or change ϵ_x and α_c is thus varying the lattice functions in the arc regions in order to obtain the wanted beam parameter values.

2.1.4 Long, Short and "Y" straight sections

The structure of each ring is completed by four so called "Y" sections between the splitters and the arcs and by two straight sections: the Long one where the beam is injected, and the Short one where the RF cavity and the feedback system are positioned.

Each "Y" section houses three quadrupoles, one harmonic sextupole employed to enlarge the dynamic aperture, one skew quadrupole and two dipole correctors to adjust the horizontal and vertical beam trajectory along the interaction region.

The feedback is a system that acts on the single bunches and is aimed at damping the longitudinal and transverse beam instabilities generated by the interaction of the charged beam with the walls of the vacuum chamber.

The focusing strength of the 7 quadrupoles positioned in the Short are usually employed for a fine correction of the betatron tunes of the machine.

The Long sections contain 10 quadrupoles and 3 sextupoles. The two injection kickers are symmetrically positioned with respect to the injection septum.

2.1.5 The injection system

DAΦNE has an injection system that provide electron and positron beams. Electrons are generated with a gun. Positrons are extracted from an electromagnetic shower by electrons impinging on a tungsten target. The injection system includes a LINAC that accelerates electrons or positrons up to 510 MeV and injects the particles in a damping ring (*Accumulator*) at a maximum frequency of 50 Hz (equal to the inverse of the damping time $\tau_{x,acc}$ of the Accumulator). Here the emittance is reduced to the proper value through the radiation damping of particles bent by dipole fields, and the beam is bunched to a RF frequency 8 times the revolution frequency in DAΦNE. After $5 \cdot \tau_{x,acc}$ the beam is extracted and sent to the main rings through two different transfer lines for electrons and positrons. The production of electrons and positrons is not simultaneous. The injection of both beams takes about 10 minutes, while a typical beam lifetime in DAΦNE is of the order of 1 hour. In order to have the highest possible integrated luminosity, electrons and positrons are reinjected when the instantaneus luminosity $\mathcal{L}$ is lower than the average luminosity $\langle\mathcal{L}\rangle$ (*topping up*).

Chapter 3

Theory of the DAΦNE luminosity performances

Besides the energy, the luminosity is the primary parameter for a particle factory. The basic theory of the DAΦNE luminosity performance is presented. The effects limiting or reducing the luminosity are discussed and their implications on the design of the rings and on the lattice set-up are pointed up.

3.1 Design luminosity of DAΦNE

The luminosity is the ratio between the event rate and the cross section of an event of interest. For a test particle crossing head-on a bunch of charge N_b, the luminosity is proportional to the bunch charge and inversely proportional to the effective transverse beam area. For two beams with n_b bunches each, colliding at the revolution frequency f_{rev}, the luminosity $\mathcal{L}$ is given by the geometrical convolution given by the particle distribution overlapping:

$$\mathcal{L} = f_{rev} n_b N_b^2 \int dx\, dy\, \rho_+(x,y)\, \rho_-(x,y); \tag{3.1}$$

where $\rho(x, y)$ is the normalized particle distribution in the transverse plane and the indexes $+$ and $-$ refer to positron and electron beam respectively. It is assumed here that the colliding bunches have the same spot sizes, charge and zero longitudinal length (short bunch approximation).

For Gaussian beams with σ_x and σ_y transverse RMS beam sizes, the transverse particle distribution is:

$$\rho(x, y; \sigma_x, \sigma_y) = \frac{1}{2\pi\,\sigma_x\sigma_y} \exp\left(-\frac{x^2}{2\sigma_x^2} - \frac{y^2}{2\sigma_y^2}\right); \tag{3.2}$$

If there are no relative transverse tilt between the two distributions, the integral of Eq. (3.1) gives the well-known expression for the luminosity of circular colliders:

$$\mathcal{L} = \frac{f_{rev} n_b N_b^2}{4\pi\,\sigma_x^*\sigma_y^*}; \tag{3.3}$$

where σ_x^* and σ_y^* are the RMS beam sizes at the interaction point. In the more general case of colliding beams with different transverse dimensions and charge the luminosity reads:

$$\mathcal{L} = \frac{f_{rev} n_b N_b^+ N_b^-}{2\pi\,\Sigma_x^*\Sigma_y^*}; \tag{3.4}$$

where $\Sigma_{x,y}^{*^2} = \sigma_{x,y+}^{*^2} + \sigma_{x,y-}^{*^2}$ are the effective beam sizes at the interaction point.

The assessment of the design luminosity continues in the next section introducing several advanced effects that affect the actual performances of DAΦNE and put some constraints on the beam parameters.

3.1.1 Hourglass effect

The expression of Eq. (3.3) overestimates the luminosity because it does not take into account the effects related to the finite bunch length. In fact the transverse sizes around

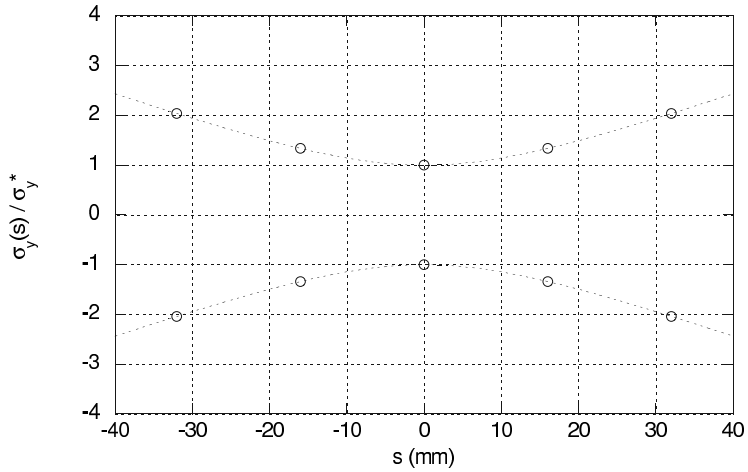

Figure 3.1: Relative vertical beam envelope (hourglass shaped) around the interaction point calculated for DAΦNE with $\beta_y^* = 18$ mm neglecting the beam-beam interaction.

the focusing point depend on s as:

$$\frac{\sigma_{x,y}^2(s)}{\sigma_{x,y}^{*2}} = 1 + \frac{s^2}{\beta_{x,y}^{*2}}; \tag{3.5}$$

thus for bunch lengths σ_z comparable with the beta function β_x^* or β_y^*, the transverse beam size growth around the focusing point reduces the luminosity. This effect is called the *hourglass effect* because of the longitudinal beam profile around the interaction point (see Fig. 3.1). The hourglass effect is a strong constraint for the minimum achievable β_y^* since the bunch cannot be shortened as we want due to the bunch lengthening effect which occurs at high current [18, 53].

Equation (3.1) can be generalized to the 4-dimentional (x, y, z, t) case [24] and the luminosity reduction due to the hourglass effect must be calculated taking into account the longitudinal motion of the two beams. The luminosity reduction factor when $\beta_{x,y+}^* = \beta_{x,y-}^*$ is:

$$R_h = \frac{\mathcal{L}}{\mathcal{L}_0} = \int_{-\infty}^{+\infty} \frac{du}{\sqrt{\pi}} \frac{e^{-u^2}}{\sqrt{1 + \frac{\Sigma_z^2 u^2}{\beta_x^{*2}}}\sqrt{1 + \frac{\Sigma_z^2 u^2}{\beta_y^{*2}}}}; \tag{3.6}$$

where u is a dummy integration variable proportional to s and $\Sigma_z^2 = \sigma_{z+}^2 + \sigma_{z-}^2$.

For the DAΦNE case $\sigma_z^2/\beta_x^{*^2} \approx (0.02/2)^2 \ll 1$, the first factor in the denominator of the integral in Eq. (3.6) can be neglected, while in the vertical plane DAΦNE is working at present at the hourglass limit $\sigma_z^2/\beta_y^{*^2} \approx 1$. Numerical integrations [1] give an hourglass reduction factor R from 0.93 to 0.83 depending on the peak values of the current per bunch (and thus on the bunch lengthening). At present β_y^* cannot decrease below 1.7 cm equal to the bunch length.

3.1.2 Beam-beam interaction

When two bunches are in collision the particles of one beam interact with the electromagnetic field generated by the opposing bunch. A test particle traveling through a Gaussian flat beam ($\sigma_y \ll \sigma_x$) undergoes an electric field in the bunch frame system given by the Bassetti-Erskine formula [3]:

$$E_x = \frac{eN_b\lambda(z)\ x}{2\pi\epsilon_0(\sigma_x^2 - \sigma_y^2)} \int_{\sigma_y/\sigma_x}^{1} \exp\left[\frac{x^2}{2(\sigma_x^2 - \sigma_y^2)}(t^2 - 1) + \frac{y^2}{2(\sigma_x^2 - \sigma_y^2)}(1 - \frac{1}{t^2})\right] dt; \qquad (3.7)$$

$$E_y = \frac{eN_b\lambda(z)\ y}{4\pi\epsilon_0(\sigma_x^2 - \sigma_y^2)^2} \int_{\sigma_y/\sigma_x}^{1} \frac{1}{t^2} \exp\left[\frac{x^2}{2(\sigma_x^2 - \sigma_y^2)}(t^2 - 1) + \frac{y^2}{2(\sigma_x^2 - \sigma_y^2)}(1 - \frac{1}{t^2})\right] dt; \quad (3.8)$$

here $\epsilon_0 = 8.8542 \cdot 10^{-12} F/m$ is the permittivity of vacuum and $N_b\lambda(z)$ is the linear charge density along $z = s \pm ct$. Figures 3.2 show as an example the force experienced by a test particle due to the electromagnetic field generated by a bunch. Because of the behavior of the Coulomb interaction, the beam-beam force for particles at large betatron amplitude is highly nonlinear. However near the bunch centre ($x < \sigma_x,\ y < \sigma_y$) the beam-beam interaction behaves linearly with respect to the transverse displacement of the test particle and acts as a quadrupole focusing the beams in both the horizontal and the vertical plane

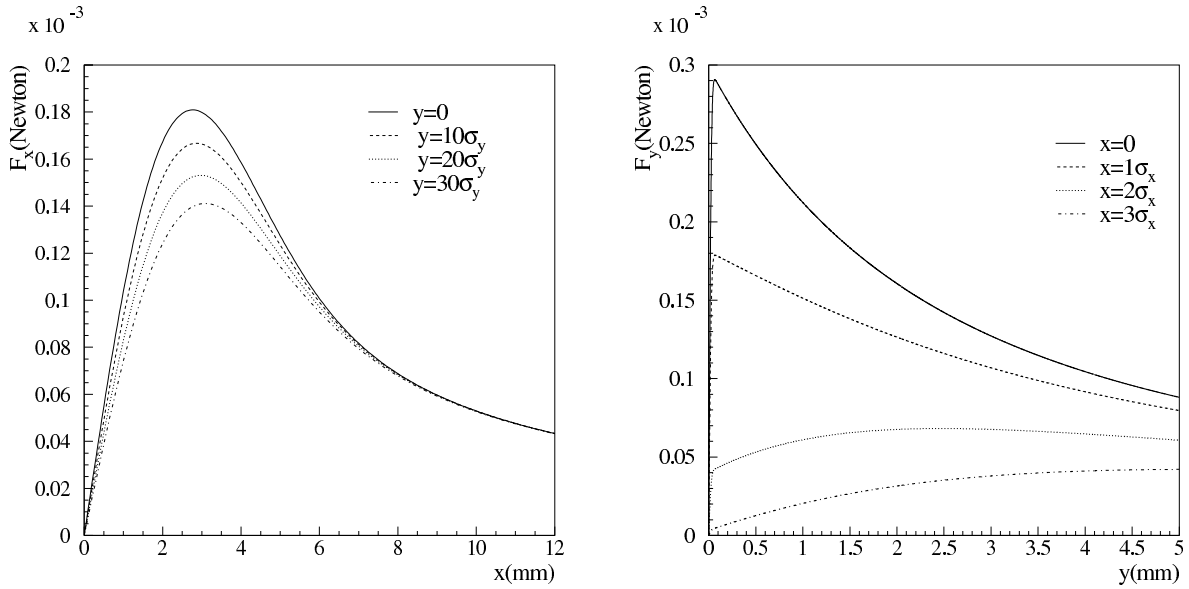

(a) (b)

Figure 3.2: Beam-beam integrated force experienced by a horizontal (a) and vertically (b) displaced particle at different vertical and horizontal positions with DAΦNE parameters ($\sigma_x = 2.1\ mm, \sigma_y = 2.1\ \mu m$) (from [17]).

with different focal lengths $f_{x,y}$:

$$\frac{1}{f_{x,y}} = -\frac{2r_e N_b}{\gamma\sigma_{x,y}(\sigma_x + \sigma_y)}. \tag{3.9}$$

For flat beams, $\sigma_y \ll \sigma_x$, the strength is stronger in the vertical plane. The effect of the mutual focusing in both planes results in a positive shift of the betatron frequencies given by:

$$\xi_{x,y} = \frac{r_e}{2\pi}\frac{N_b\beta^*_{x,y}}{\gamma\sigma_{x,y}(\sigma_x + \sigma_y)}. \tag{3.10}$$

The *beam-beam tune shifts* ξ_x and ξ_y measure the linear part of the beam-beam force and they are of primary interest for a collider because they also specify the strength of the beam-beam nonlinearity (felt by particles at $x > \sigma_x$ or $y > \sigma_y$) that gives a limit to the

maximum current (or the maximum transverse density of the beam) can be stored in the rings. In fact when either ξ_x or ξ_y exceeds a certain value, characteristic of the specific collider, the nonlinear part of the beam-beam interaction is so strong that instability and beam blow-up occur and the luminosity and the beam lifetime are dramatically reduced. If the beams collide in more interaction points per turn, the beam-beam effects add up and the luminosity performances are further limited.

The tune shift limit of a collider can not be theorically predicted, however there is experimental evidence from previous and existent e^+e^- machines that for all colliders the tune shift limit is reached at $\xi \approx 0.06 - 0.07$ [43]. The estimate of the DAΦNE tune shift limit is $\xi_{lim} = 0.04$ [54].

Since at present DAΦNE is not limited by the tune shift (the largest limitations in multibunch configuration coming from a longitudinal quadrupole instability cured with the feedback system), the emittance has been gradually decreased from the design value of $1{\cdot}10^{-6}$ m rad to $0.45{\cdot}10^{-6}$ m rad in order to reduce the beam size and increase the luminosity with several benefits for the beam lifetime, the detector background, and the parasitic crossings.

3.1.3 Crossing angle

Another geometrical reduction effect comes from the non-zero crossing angle between the colliding beams. In DAΦNE the two opposing beams collide with a horizontal crossing angle ϕ to avoid parasitic crossings between the outgoing bunches after collision and the incoming bunches of the opposing beam. Parasitic crossings can reduce the luminosity if the trajectories of the opposing beams are not properly separated. On the other hand the crossing angle must be small to avoid both synchro-betatron resonances (the Piwinski condition [35]: $\phi\sigma_x/\sigma_z \ll 1$) and reduction in luminosity because of the overlapping reduction with respect to the head-on collision. For $\sigma_y \ll \sigma_x$ and $\sigma_z \ll \beta_y^*$ (i.e. neglecting

the hourglass effect) the reduction in luminosity from the crossing angle is related in first approximation to the widening of the effective horizontal dimension, because the projected beam size along the interaction region increases, and the reduction factor can be expressed as [29]:

$$R_c = \frac{\mathcal{L}}{\mathcal{L}_0} \approx \left[1 + \left(\frac{\sigma_z}{\sigma_x}\tan\phi\right)^2\right]^{-1/2}; \tag{3.11}$$

The crossing angle ϕ must be chosen as a compromise between the parasitic crossing perturbation, which profits from large ϕ, the synchro-betatron resonances and the geometrical reduction in luminosity.

The original low-beta regions of DAΦNE with two FDF triplets allowed working with $\phi = 12.5$ mrad, little enough to fit the Piwinski condition. The new design with two doublets FD allows increasing the crossing angle until 16.5 mrad (see Chapter 5) improving the beam separation as the machine operation demonstrated that the collider was still below the synchro-betatron limit.

3.1.4 Numerical simulations of the DAΦNE luminosity: choice of the working point

The luminosity of a circular collider is strongly dependent on the working point of (i.e. the betatron tunes values Q_x and Q_y) and at DAΦNE the luminosity at different working points has been estimated from numerical simulations that take into account all the aforementioned effects as well as the nonlinearities of the magnetic lattice of the Main Rings [54]. During the collider commissioning the working point (0.15, 0.21) was chosen for collisions as the best trade-off between high luminosity and other requirements (dynamic aperture, low second order chromaticity terms, low sensitivity to magnetic element errors...). At present the positron ring is tuned at this working point in every configuration (collision in IP1 or IP2). However we had to shift the working point of the electron

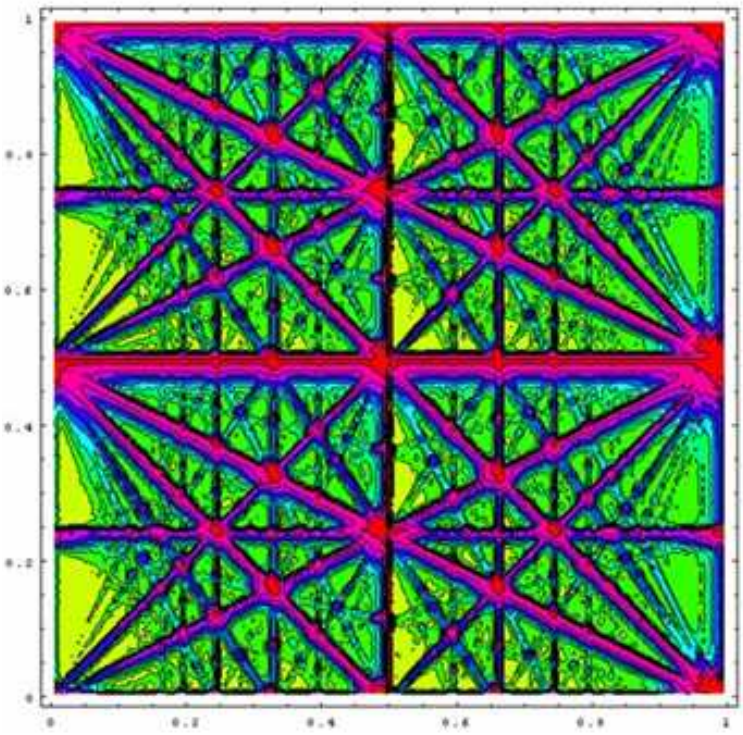

Figure 3.3: The single bunch luminosity in the (Q_x, Q_y) plane. The clearer areas are those with higher luminosity, the dark regions correspond to the lower luminosity near resonance lines.

ring to (0.10, 0.14) because at high currents a strong vertical instability in the positron ring is transmitted to the electron ring if the betatron tunes are equal in the two rings. Separating the tunes the instability is eliminated by the so called Landau damping due to the nonlinear beam-beam interaction. Studies and tests for the quest of new working points closer either to the integer or to half the integer are always under investigation.

Chapter 4

Development of the DAΦNE optics model

After a presentation of the general frame of the main ring model, the modelling of the FINUDA interaction region and of the modified wiggles developed in 2002-2003 is discussed in this chapter.

The optics model has been developed by the DAΦNE team for the code MAD [26] and it has been optimized and updated gradually during the machine operation [10, 34]. MAD describes the beam optics in accelerators and is able to solve several kinds of problems: simulation of the optics parameters of a lattice (beta-functions, dispersion, betatron tunes, emittance, damping parameters...), lattice matching, transfer matrix matching, calculation of closed orbits... MAD represents a ring as a sequence of physical elements: magnetic as dipoles, quadrupoles etc. and non magnetic as drift sections, RF cavities, monitors etc. Each element is defined by proper physical parameters as the element length, the field strength etc. that determinate the effects on the beam dynamics.

Table 4.1: Nominal parameters of the main ring dipoles used in MAD. L is the magnetic length, *gap* the heigh of pole gap, α the bending angle, ρ the curvature radius of the trajectory through the magnet, e_1/e_2 the angle in the horizontal plane the trajectory enters/exits with respect to the pole face (Fig. A.1), *fint* the first integral of the normalized field.

Type	L_{mag} (m)	*gap* (cm)	α (^{o})	ρ (m)	e_1/e_2 (^{o})	*fint*
Sector Short	0.990	7.56	40.50	1.401	0.00/0.00	0.5292
Rectangular Short	0.990	7.56	40.50	1.401	20.25/20.25	0.5756
Sector Long	1.210	7.56	49.50	1.401	0.00/0.00	0.5431
Rectangular Long	1.210	7.56	49.50	1.401	24.75/24.75	0.6208
Splitter	1.450	7.53	8.75	9.495	-0.25/9.00	0.3000

4.1 Lattice model of the main rings for MAD

Bench measurements on every magnetic element of DAΦNE were performed before the installation using two different systems [31]:

- maps (steps of 1 cm or less) of the magnetic field components B_y or B_x on the mid-plane of bending dipoles, splitters and correctors was measured with a Hall effect Digital Teslameter on a 5-axes movement device;

- integrated multipole field components of quadrupoles, sextupoles and octupoles were measured with an automatic rotating coil Multipole Measurement System.

The modelling of the magnetic elements has been deduced from these measurements as is described in the following sections.

4.1.1 Bending dipoles and splitters

The design parameters of the four bending dipole families (two of sector type and two of rectangular type) and of the splitters [14, 13, 12, 16] are reported in Table 4.1. The

effective magnetic length of a magnet is defined by:

$$L_{mag} \cdot B_0 = \int_{-\infty}^{+\infty} B(s)ds; \tag{4.1}$$

where B_0 is the field in the middle of the magnet and the *fint* parameter is defined [30]:

$$fint = \int_{-\infty}^{+\infty} \frac{B_y(s)(B_0 - B_y(s))}{g \cdot B_0^2} ds; \tag{4.2}$$

where g is half the pole gap. The $fint$ is a corrective term of the vertical focusing generated by end-fields.

From the measured map the magnetic field can be interpolated at every point on the dipole mid-plane of the magnet and the multipolar components have been fitted[1]. A detailed discussion on the problems concerning the DAΦNE dipole modelling (focusing effects due to the entrance/exit angles, sextupolar terms in the fringing regions...) was done in [5].

The DAΦNE splitters are special magnets set up by two adjacent dipoles with different coils, that generate opposite field in the adjacent regions. The two pole gaps are separated by a septum that divides the electron vacuum chamber from the positron one (Fig.4.1). A refinement of the splitter model has been done taking into account the focusing effect due to the sextupole term in the fringing region. In fact the vertical component of the field B_y is strongly dependent on the horizontal position because of the asymmetry of the magnet. As shown by measurements plotted in Fig. 4.2, towards the interaction region where the trajectory passes at 6 cm from the splitter axes the beam undergoes a field

[1]If one have n transverse points for every longitudinal position along the design trajectory, the polynomial coefficients of the field expansion to the $n-1$ order in x can be calculated. For instance, the expansion of B_y along the longitudinal coordinate z with respect to the transverse coordinate x is:

$$B_y(x,0,z) = B_0(z) + B_1(z)x + B_2(z)x^2 + \cdots$$

where $B_0(z)$ corresponds to B_y along the nominal trajectory, $B_1(z)$ to the quadrupole term $\partial B_y/\partial x$, $B_2(z)$ to the sextupole term $\frac{1}{2}\partial^2 B_y/\partial x^2$ and so on.

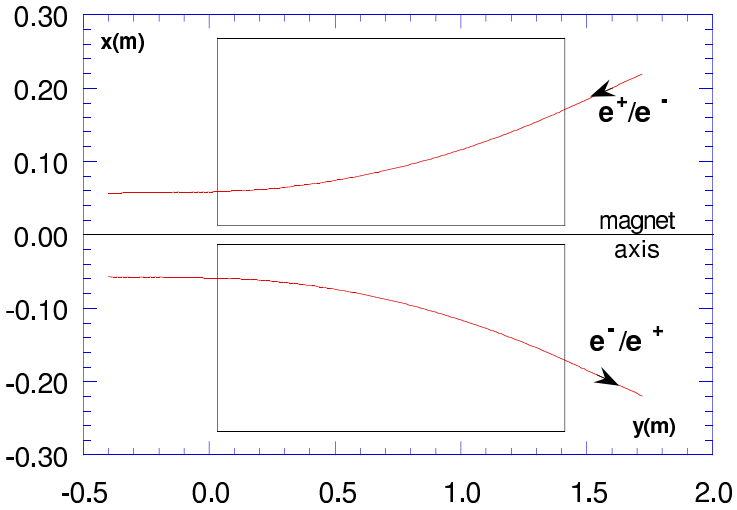

Figure 4.1: Nominal beam trajectories through the splitter magnet (in this figure y denotes the longitudinal coordinate which is usually indicated with z.)

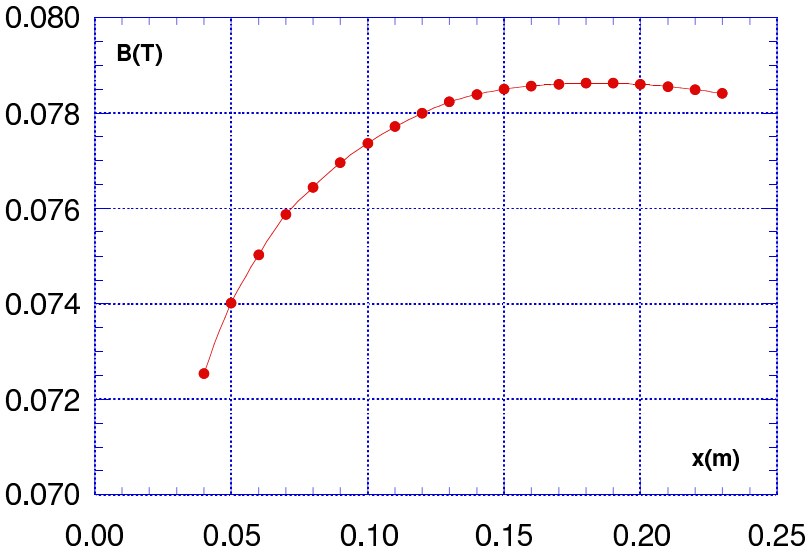

Figure 4.2: B_y transverse scan measured near the splitter edge (at $y = -4.5$ mm in Fig. 4.1).

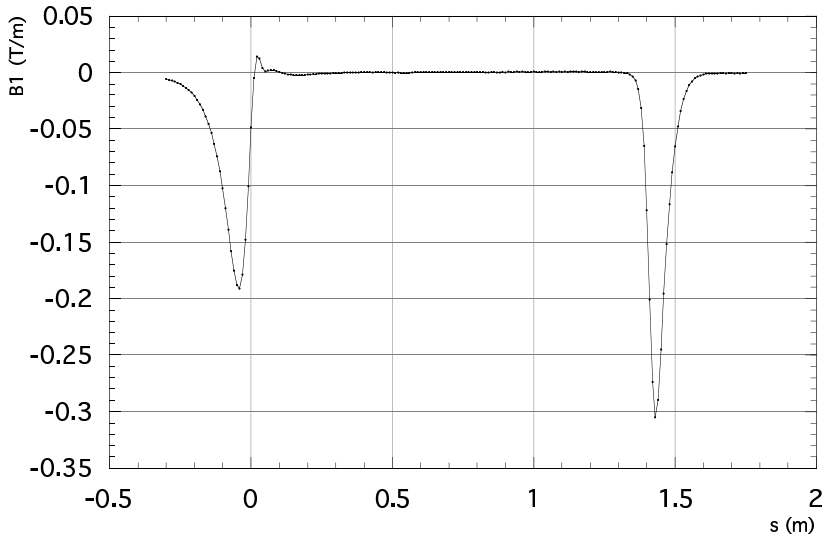

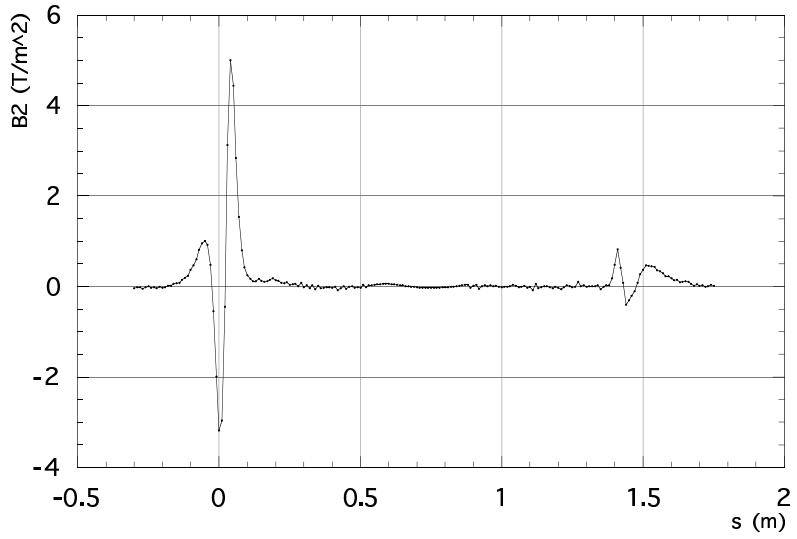

Figure 4.3: First order coefficient $B_1(s)$ (quadrupolar gradient) of the transverse field expansion of the splitter around the nominal trajectory.

Figure 4.4: Second order coefficient $B_2(s)$ (twice the sextupolar gradient) of the transverse field expansion of the splitter around the nominal trajectory.

gradient, while in the opposite side towards the "Y" section where the trajectory passes at about 18 cm the field behaviour is flat. In Fig. 4.3 shows the first order coefficient $B_1(s) = \partial B_y/\partial x$ (quadrupolar gradient) of the transverse field expansion around the nominal trajectory through the magnet. The peak at the splitter entrance ($s = 0$), which in an ideal rectangular magnet with entrance angle -0.25° should be negligible, is generated by the transverse gradient next to the coil in the end-field region, while the peak at the exit ($s = 1.45$ m) is due mainly to the angle of 9° between the pole face and the beam trajectory (Fig. 4.1) as expected in a rectangular dipole.

The additional focusing strength (not coming from the geometry) from this effect has been modelled embedding the splitter between two thin lenses with integrated normalized gradient 0.0123 m^{-1} and 0.0025 m^{-1}.

4.1.2 Quadrupoles, sextupoles and octupoles

The magnetic length and the bore diameter of the quadrupoles, sextupoles and octupoles of DAΦNE are reported in Table 4.2. The radius of the good field region for all multipoles is 3 cm but for the large aperture quadrupoles it is 6 cm. The field quality is $\Delta B/B \leq 5 \cdot 10^{-4}$.

The characteristic magnetic gradients of every family of multipole are modelled with a hard-edge profile and they are calibrated with respect to the powered current [27]. The behaviour of the field is linear with respect to the current at the usual operation values. In the MAD deck file the normalized multipole coefficients are defined in terms of the power supply currents, so that the ring lattice can be easily simulated as a function of different current data sets.

In the model the multipole strength:

$$K_n = \frac{1}{B\rho}\left|\frac{\partial^n B_y}{\partial x^n}\right|; \tag{4.3}$$

	Quadrupole type			Sextupole type		Octupole
	Large	*Small*	*Large ap.*	*Large*	*Small*	
Number per ring	14	25	6	12	8	3
Magnetic length (cm)	29.0	30.0	38.0	15.0	10.0	10.0
Bore diameter (cm)	10.8	10.0	20.0	10.8	10.8	10.0
Max current (A)	175	585	585	250	336	120
Max curr. below satur. (A)	123	304	380	150	336	100
C_1 (MeV A^{-1} m^{-2})	16.96	9.128	3.979	51.18	19.74	
C_2 (MeV m^{-2})	5.62	4.53	2.72	49.34	32.8	
C_3 (MeV A^{-1} m^{-3})						8.388

Table 4.2: The characteristic parameters of the DAΦNE multipole magnets.

are expressed as a function of powered currents as:

$$\begin{aligned} K_1\ [m^{-2}] &= (C_1 \cdot |I|\ [A] + C_2)/E_0\ [MeV]; \\ K_2 L_{sxp}\ [m^{-2}] &= (C_1 \cdot |I|\ [A] + C_2)/E_0\ [MeV]; \\ K_3 L_{oct}\ [m^{-3}] &= C_3 \cdot |I|\ [A]/E_0\ [MeV]; \end{aligned} \tag{4.4}$$

with the calibration constants C_1, C_2 and C_3 tabulated in Table 4.2.

4.2 Modelling of the FINUDA IR from magnetic measurements

The FINUDA interaction region has been modelled similarly to the KLOE one. The IRs are the sections modelled in the most detailed way of all the rings, the main feature of the model is the representation of the four permanent quadrupoles immersed in the solenoid field of the detector. The superposition of a transverse field gradient and a solenoid field

is simulated as a sequence of thick solenoid slices alternated with thin lenses (zero length) of varying strength representing the longitudinal dependence of the quadrupole field:

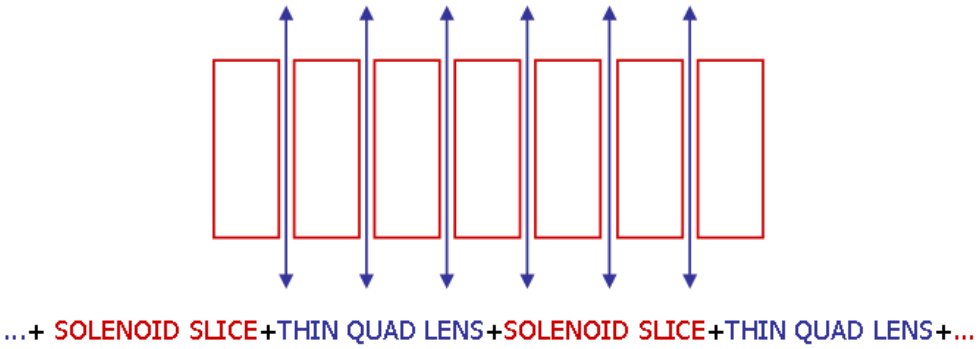

The other four electromagnetic quadrupoles and the two compensators are positioned outside the detector and they are represented individually.

4.2.1 FINUDA and compensating solenoids

The solenoid field of FINUDA and of the two compensators is known along the longitudinal axes of the magnets with steps of 1 cm. In the model the solenoid magnets are represented as a sequence of 3 cm slices with the field averaged on the segment. Figure 4.5 shows the longitudinal dependence of the field.

4.2.2 Permanent and electromagnetic quadrupoles

The magnetic field of the permanent and electromagnetic quadrupoles with large aperture for the second interaction region has been measured both with the rotating coil system and with the Hall probe on the horizontal plane [36, 15]. The field gradient (and the small higher multipole coefficients) is known all along the magnetic axes with a resolution of 1 cm.

The gradient of the permanent quadrupoles, that are inserted inside the FINUDA

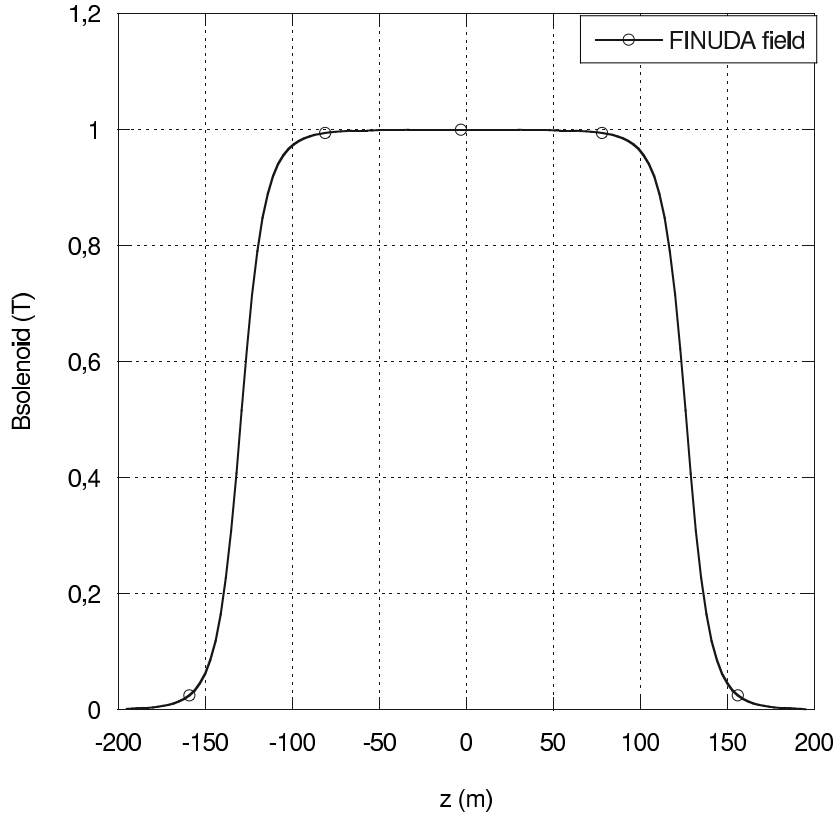

Figure 4.5: The measured FINUDA solenoid field along the longitudinal axis.

solenoid, has been integrated every 3 cm and the integrated value is inserted in the MAD definition of a thin lens representing a segment of quadrupole. Each thin lens is also rotated around the longitudinal axes, the roll angles of the IR quadrupoles are tabulated in Table 4.3.

	Permanent		Electromagnetic	
	QPM001	QPM002	QUAI2001	QUAI2001
Magnetic length (cm)	15.8	30.0	38.0	38.0
Bore diameter (cm)	12.0	12.0	20.0	20.0
Nominal gradient (T/m)	9.433	10.802	2.254	3.383
Roll angle (°)	6.75	12.80	19.80	19.80

Table 4.3: The IR2 quadrupole parameters.

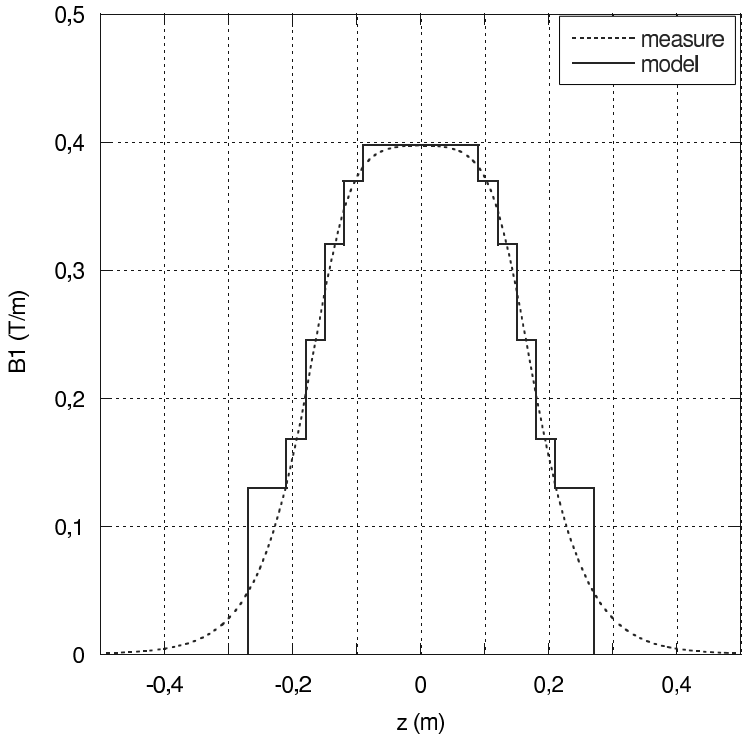

Figure 4.6: Decomposition of the actual large aperture quadrupole field profile into segments of hard edge quadrupole.

The large aperture quadrupoles are special electromagnetic magnets designed for the IR vacuum chamber installed between FINUDA and the compensators. The magnetic length is 38 cm, less than twice the diameter of the bore aperture equal to 20 cm. In this case the field profile has long tails outside the quadrupole and the customary parameters L_{mag} and k_0 of the hard-edge model used for the quadrupoles of the ring, where $L_{mag} = \frac{1}{k_0}\int k(s)ds$ and k_0 is the actual quadrupole strength at the middle of the magnet, give an unsatisfactory approximation of the transfer matrix of the quadrupole magnet [7, 49] resulting also in a betatron tune shift of about 0.002 with respect to the actual matrix. In this case it is better to decompose the quadrupole in thin slices of varying strength, treating these segments as short hard-edge quadrupoles the full transfer matrix is the product of the matrices for all segments. In Figure 4.6 is plotted the decomposition of

the actual large aperture quadrupole field profile into segments of hard edge quadrupoles as it has been done in the MAD model.

4.3 Hard-edge model of the modified wigglers

The DAΦNE wigglers magnets are a row of seven alternately deflecting bending magnets which do not introduce a net deflection on the beam. Wigglers are in general sources of non linear fields in the lattice of a ring because of the transverse width of the pole comparable with the aperture gap, resulting in a fast roll-off of the dipole field in the transverse direction. In 2003 the pole shape of the DAΦNE wiggler have been modified in order to reduce the high order multipoles and thus increase the dynamic aperture of the ring.

The modified wiggler magnets of the Main Rings have been modelled as a 2 m long sequence of hard-edge dipoles alternated with drift sections describing the behaviour of the magnet for the linear beam optics. Each pole is embedded in two additional thin lenses per pole which reproduce the non-linear terms of the field. The physical parameters of the model are based on the measurement of the field By versus the position (x,z) in the horizontal midplane of the central pole and on the two terminal poles, which has been taken on the modified wiggler in 2003 [37].

Total length (m)	2.00
Magnetic field (T)	1.73
End pole length (cm)	20.0
Inner pole length (cm)	32.0
Pole gap (cm)	3.70
Pole width (cm)	14.0

Table 4.4: DAΦNE wiggler parameters.

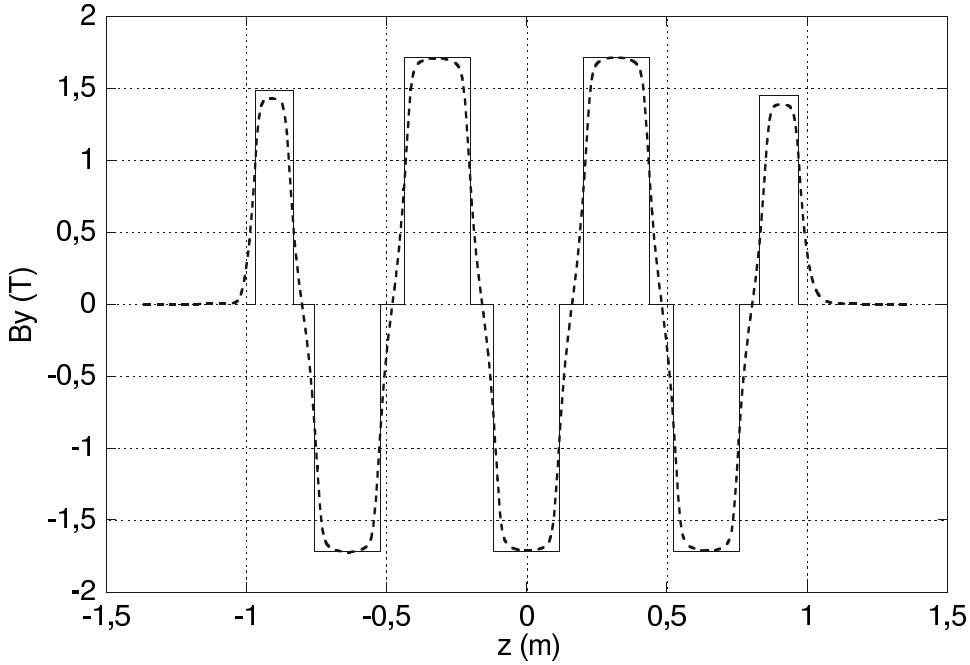

Figure 4.7: The wiggler field along the longitudinal z axis: the dashed line is the measured field and the full line the hard-edge model.

4.3.1 Linear properties

For the proper linear modelling of wiggler magnets two conditions require to be fulfilled. The deflection angle and the length of each modelled pole must be the same of the actual trajectory. Similarly the edge focusing described in the model (the fint parameter used by MAD) must be the same felt by a particle travelling around the nominal trajectory. The corrections to the linear optics due to the wiggling trajectory through multipole field components is considered in a following step and added to the model as thin lenses.

Wiggling trajectory of the nominal particle

The first step is the calculation of the trajectory of the nominal particle along the whole wiggler. The magnetic field on the horizontal midplane ($y = 0$), where the trajectory lies, has only the vertical component $B_y(x, 0, z)$, while $B_{x,z}(x, 0, z) = 0$. In the reference system

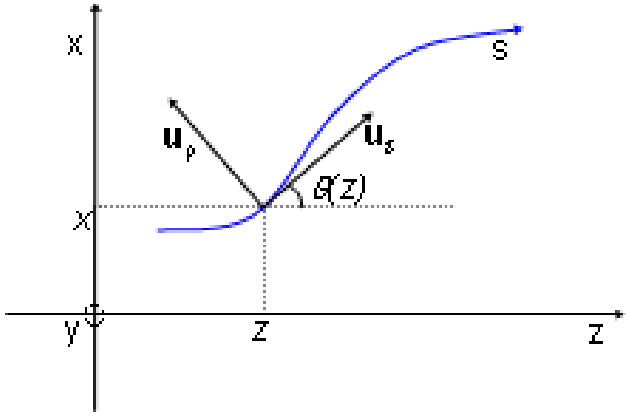

Figure 4.8: The global and the local coordinate systems along the trajectory.

in Fig. 4.8 the particle velocity is: $\dot{\mathbf{r}} = c\mathbf{u}_s$ and the magnetic field: $\mathbf{B}(x,z) = B_y(x,z)\mathbf{u}_y$. Thus a charged particle undergoes the Lorentz force according to:

$$\begin{aligned} \ddot{x} &= -\tfrac{e}{p_0}\dot{z}B_y(x,y); \\ \ddot{z} &= \tfrac{e}{p_0}\dot{x}B_y(x,y); \end{aligned} \tag{4.5}$$

which gives:

$$\begin{aligned} \ddot{x} &= -\tfrac{e}{p_0}c^2 B_y(x,y)\cos\theta; \\ \ddot{z} &= \tfrac{e}{p_0}c^2 B_y(x,y)\sin\theta; \end{aligned} \tag{4.6}$$

with $\tan\theta = dx/dz$. The derivatives in the system above are done with respect to the time variable t, while the magnetic field $B_y(x,z)$ is known from measurement as a function of the position in the midplane as well as $\theta(z)$ is expressed as a function of the longitudinal position z. Therefore z is the most suitable variable for numerical integration. Considering

$cdt = ds = [1 + (dx/dz)2]^{3/2}dz$, the second derivative is expressed according to:

$$\begin{aligned} \ddot{x} \equiv \frac{d^2x}{dt^2} &= c^2\frac{d^2x}{ds^2} = c^2\frac{1}{\sqrt{1+\left(\frac{dx}{dz}\right)^2}}\,\frac{d}{dz}\left[\frac{1}{\sqrt{1+\left(\frac{dx}{dz}\right)^2}}\right] = \\ &= c^2\frac{1}{\left(1+\left(\frac{dx}{dz}\right)^2\right)^2}\frac{d^2x}{dz^2} = c^2\cos^4\theta\frac{d^2x}{dz^2}; \end{aligned} \tag{4.7}$$

and after the variable change the trajectory equation becomes:

$$\cos^3\theta(z) = -\frac{e}{p_0}B_y(x,y); \tag{4.8}$$

and eventually:

$$\frac{d^2x}{dz^2} = -\frac{1}{B\rho}\left[1+\left(\frac{dx}{dz}\right)^2\right]^{3/2}B_y(x,y). \tag{4.9}$$

Eq. 4.9 is the differential equation that has been numerically integrated from the table of field measurements with a recursive algorithm with start path $x(z) = 0$. The spacing between the points in the data table is 1 cm, both longitudinally and horizontally. The field $B_y(z)$ is first fitted with a series of cubic polynomials connected together (*cubic spline*) and then integrated with 1 mm longitudinal steps. The integration converges after few iterations (2-3) since within the 12.5 mm horizontal range, where the trajectory oscillates, B_y has little and smooth variations and dx/dz is sufficiently small ($\Delta B/B_0 < 2\cdot 10^{-3}$ and $dx/dz < 0.12$). Once the trajectory is known, the path length is calculated from:

$$L_{traj} = \int_{wiggler} ds = \int_{wiggler}\sqrt{1+\left(\frac{dx}{dz}\right)^2}dz. \tag{4.10}$$

The wiggler in Figure 4.9 is the trajectory along the magnet, for the nominal particle launched at the entrance to the pole A with $x = -12.5$ mm and $x' = 0$ rad as is calculated by the model. The length of the wiggling path comes out to be 6.62 mm longer than the

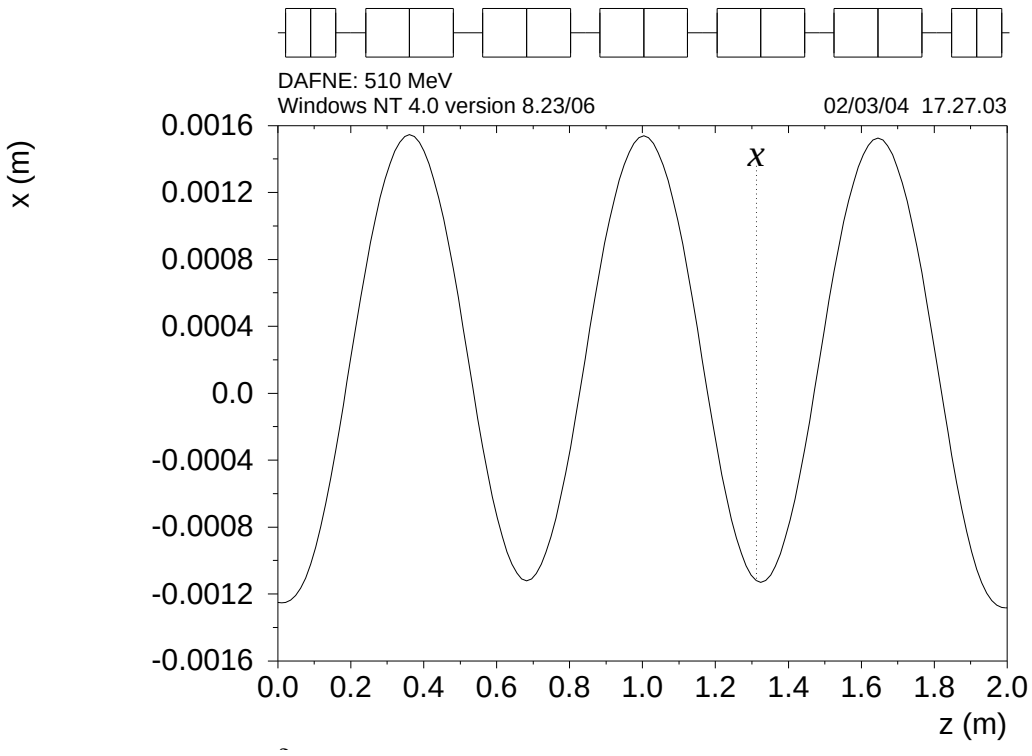

Figure 4.9: The wiggling trajectory: the particle launched from the terminal pole A.

longitudinal straight line along the axis.

Choise of the modelling parameters

Once the amplitude, the deflection angle and the length of the trajectory are known, the wiggler can be modelled pole by pole. Each pole is represented by a single parallel-end hard-edge dipole with length L_h (Figure 4.7) embedded in two drift sections with length L_d: the total length of the pole $L_p = L_h + 2\ L_d$ is fixed equal to the nominal particle path length integrated along the pole. The modelling problem consists in the choice of the effective L_h.

Once the wiggling trajectory was known, the transfer matrix of each single pole has been calculated from the table of the field measurements.

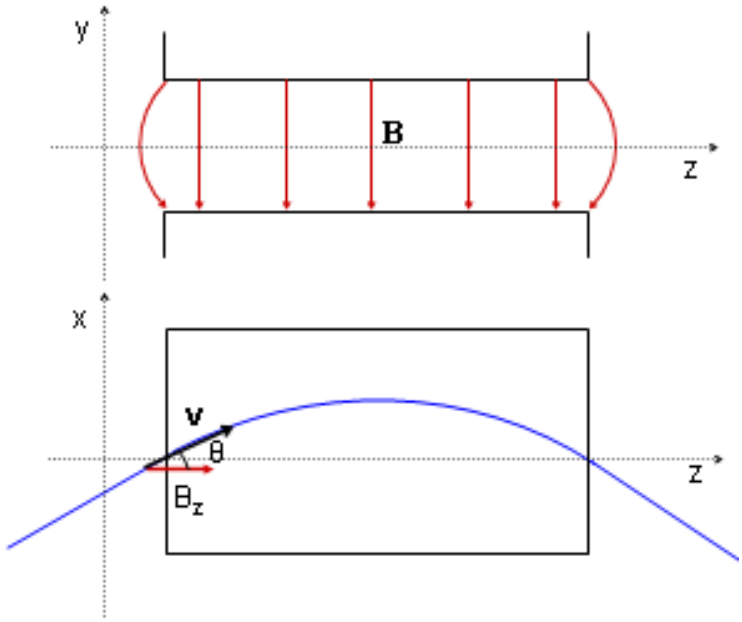

Figure 4.10: Schematic y-z and x-z projections of a parallel-end dipole showing the fringe field.

Linear Transfer Matrix

On the horizontal midplane of each pole the field is everywhere vertical (Figure 4.10) therefore in a parallel end dipole (neglecting at the moment the finite horizontal width of the magnet) there is no focusing effect on the horizontal plane. The scenario changes for a particle displaced vertically. In this case it undergoes the longitudinal component Bz of the field in the fringing region, which is responsible of the edge vertical focusing in a dipole. Launching a particle with $(y, y') = (1, 0)$ and $(y, y') = (0, 1)$, the values of the position y and the divergence y' at the end of the pole are the columns of the vertical transfer matrix and the physical problem consists in the tracking of the particle around the trajectory previously calculated. The vertical equation of motion is (see Figure 4.10):

$$\ddot{y} = \frac{ec^2}{p_0}(\dot{\mathbf{r}} \times \mathbf{B})_y = \frac{ec^2}{p_0} B_z \sin\theta; \tag{4.11}$$

and by derivating with respect to z as in Eq. 4.8:

$$\cos^4\theta \frac{d^2y}{dz^2} = \frac{e}{p_0} B_z \sin\theta; \tag{4.12}$$

and eventually:

$$\frac{d^2y}{dz^2} = \frac{1}{B\rho}\left[1 + \left(\frac{dx}{dz}\right)^2\right]^{3/2} \frac{dx}{dz} B_z(x,z); \tag{4.13}$$

where dx/dz is the derivative of the horizontal wiggling trajectory $x(z)$ already integrated from Eq. 4.9.

For linear modelling the field components at position y can be estimated expanding the magnetic field to first order around the midplane ($y = 0$), where the field is known. Using also Maxwell's equations:

$$B_x(x,y,z) = y\left(\frac{\partial B_x}{\partial y}\right)_{y=0} = y\left(\frac{\partial B_y}{\partial x}\right)_{y=0} \tag{4.14}$$

$$B_y(x,y,z) = y\left(\frac{\partial B_y}{\partial y}\right)_{y=0} = -y\left(\frac{\partial B_x}{\partial x} + \frac{\partial B_z}{\partial z}\right)_{y=0} = 0 \tag{4.15}$$

$$B_z(x,y,z) = y\left(\frac{\partial B_z}{\partial y}\right)_{y=0} = y\left(\frac{\partial B_y}{\partial z}\right)_{y=0}. \tag{4.16}$$

The behaviour of $B_y(x,z)$ has been measured and fitted and the vertical trajectory can be numerically integrated with the same procedure followed for the wiggling trajectory. The dipole lengths and the fint parameters are then fixed pole by pole fitting the matrix elements by using the matching tools of the MAD program as described below.

Inner Poles

In the model the inner poles are assumed to be equal among them and the physical parameters are obtained from the measurements performed on the central pole. The

deflection angle of the central pole comes out to be $\theta_C = 0.2375$ rad and the entrance and exit angles are half the deflection angle: $e_1 = e_2 = \theta/2$. Since the dipole has parallel ends, in the horizontal plane there is no focusing effect and the horizontal transport matrix does not depend on L_h but only on the total pole length L_p that is fixed. Therefore the dipole length and the edge focusing parameter fint have been chosen in order to match the vertical transfer matrix of the single pole calculated from the measured field map. The obtained values are $L_h = 0.2355$ m and $fint = 0.315$.

End Poles

One of the end poles (B type or "right") has a strong sextupole field index useful to improve the dynamic aperture: as a consequence the poles A and B, which are powered by the same supply, have slightly different field integrals and different deflection angles between them. The supplied current is such that the field integral along the wiggler axis vanishes ($\int B_y dz = 0$). The deflection angle of the right pole is $\theta_B = -0.1196$ rad and the left one $\theta_A = -0.1167$ rad. The entrance and exit angles are: $e_1 = 0$, $e_2 = \theta_{A,B}$. The end dipole length and the fint parameter chosen with the same procedure followed for the central poles are $L_h = 0.1368$ m and $fint = 0.213$.

4.3.2 Linear and non-linear field perturbations as thin lenses

Finite horizontal pole width in a wiggler magnet creates a roll-off in $B_y(x)$ which generates linear and non-linear perturbations to particle dynamics [2, 40]. The Figure 4.11 shows $B_y(x)$ at the wiggler centre fitted from measurements: the 14 cm pole width results in the field rolling off quickly at $\pm$ 50 mm. The final step for the complete modelling is to consider the linear corrections to transfer matrix integrating the complete equation of motion that takes in account the horizontal roll off of the field, which generates multipole terms. In the model this is realized adding thin lenses at the dipole edges, whose integrated gradient

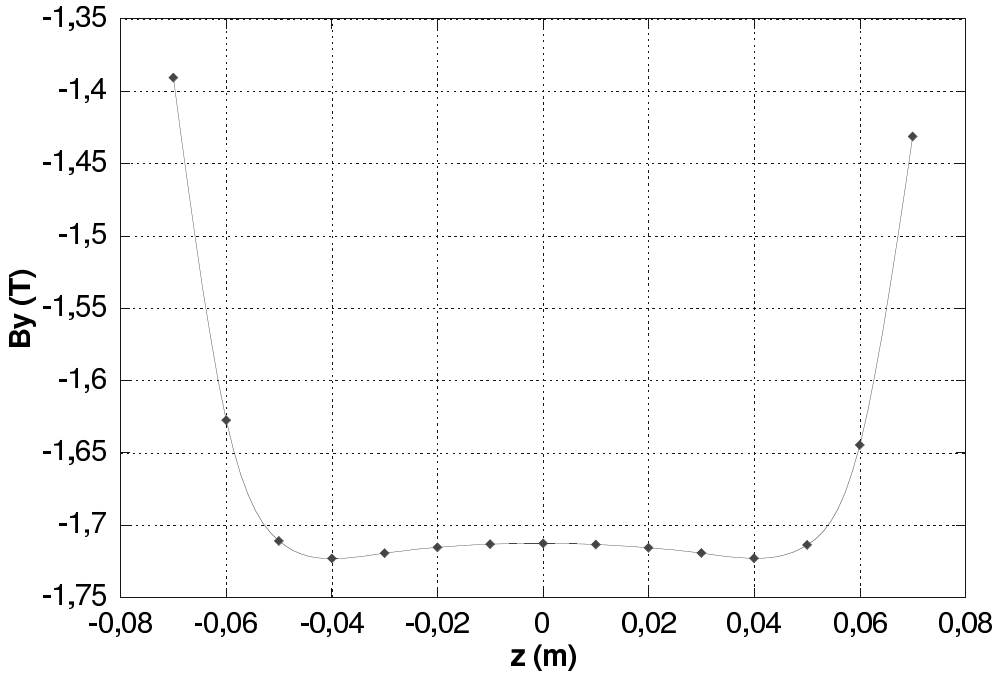

Figure 4.11: Transverse field roll-off at the centre of the wiggler.

values $K1$ have been found matching again the corrected transfer matrix calculated from the equation of motion:

$$\ddot{y} = \frac{ec^2}{p_0}(\dot{\mathbf{r}} \times \mathbf{B})_y = \frac{ec^2}{p_0}(B_z \sin\theta - B_x \cos\theta); \tag{4.17}$$

which gives:

$$\frac{d^2y}{dz^2} = \frac{1}{B\rho}\left[1 + \left(\frac{dx}{dz}\right)^2\right]^{3/2}\left(\frac{dx}{dz}B_z(x,z) - B_x\cos\theta\right). \tag{4.18}$$

The final integrated vertical trajectories $y(z)$ through the single poles are shown in Figures 4.13 and 4.12.

The transverse polynomial expansion of the field [37] shows up a small but not negligible sextupole term and higher multipoles that give linear and non-linear perturbations to both the horizontal and the vertical motion around the trajectory. All these effects are taken in account in the model embedding each dipole in two thin lenses with integrated

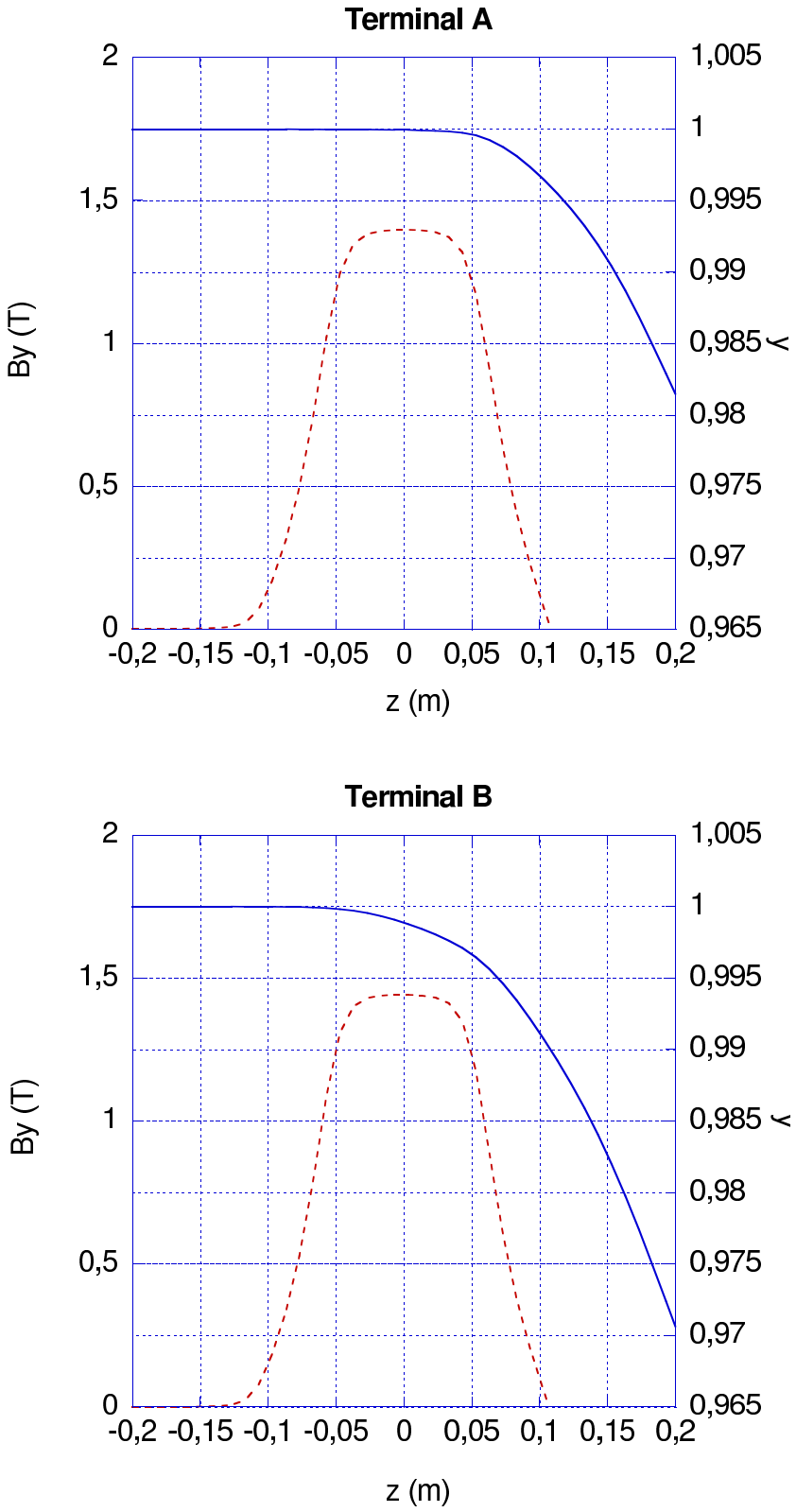

Figure 4.12: The vertical trajectory (full line) in the terminal poles starting with $(y, y') = (1, 0)$: the terminal B has an extra-focusing term due to the sextupole; the dashed line is the magnetic field.

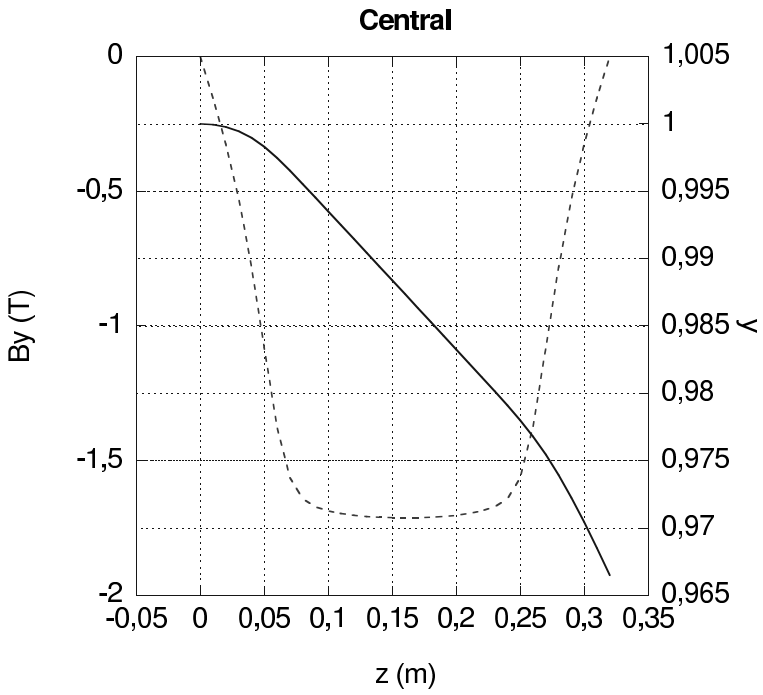

Figure 4.13: The vertical trajectory (full line) in the central pole entering in the pole with $(y, y') = (1, 0)$; the dashed line is the magnetic field.

	End Pole A	Inner Poles	End Pole B
L_h (m)	0.1368	0.2355	0.1368
L_p (m)	0.2000	0.3200	0.2000
θ (rad)	0.1167	0.2375	0.1196
fint	0.384	0.317	0.384
K1 (m^{-1})	0.0	-0.0022	0.0260
K2 (m^{-2})	0.23	± 0.78	34.4 (m^{-1})
K3 (m^{-3})	23.0	-34.4	15.0
K4 (m^{-4})	-0.0025	± 0.0045	-0.0014

Table 4.5: The MAD parameters of the wiggler

gradients along the trajectory:

$$K1 = \frac{1}{B\rho}\int \frac{dB_y}{dx}\,ds = \frac{1}{B\rho}\int \left(\frac{\partial B_y}{\partial x} + \frac{\partial^2 B_y}{\partial x^2}x + \frac{\partial^3 B_y}{\partial x^3}\frac{x^2}{2} + \frac{\partial^4 B_y}{\partial x^4}\frac{x^3}{6}\right)dz; \quad (4.19)$$

$$K2 = \frac{1}{B\rho}\int \frac{d^2 B_y}{dx^2}\,ds = \frac{1}{B\rho}\int \left(\frac{\partial^2 B_y}{\partial x^2} + \frac{\partial^3 B_y}{\partial x^3}x + \frac{\partial^4 B_y}{\partial x^4}\frac{x^2}{2}\right)dz; \quad (4.20)$$

$$K3 = \frac{1}{B\rho}\int \frac{d^3 B_y}{dx^3}\,ds = \frac{1}{B\rho}\int \left(\frac{\partial^3 B_y}{\partial x^3} + \frac{\partial^4 B_y}{\partial x^4}x\right)dz; \quad (4.21)$$

$$K4 = \frac{1}{B\rho}\int \frac{d^4 B_y}{dx^4}\,ds = \frac{1}{B\rho}\int \frac{\partial^4 B_y}{\partial x^4}dz. \quad (4.22)$$

The $K1$ coefficients are chosen fitting the single pole transfer matrices , while $K2$, $K3$ and $K4$ come from the magnetic measurements fit ([37] Table I). In the model of the inner poles the average value among the five poles is taken for each Kn coefficient. Only in the end pole B, where the sextupole term is strong and quite constant (see [37] Fig. 32), the sextupole gradient $K2$ is spread out along the whole dipole.

4.3.3 Results of the MAD model

The model reproduces with very good accuracy the linear matrix elements calculated from the measurements ($\Delta R_{ij} \approx 10^{-4}$). After the whole map of the field on the midplane was measured (October 2003), the fint parameters have been further finely readjusted in order to match the whole wiggler transfer matrix obtained from the magnetic measurements [37]

and are reported below. The central pole matrix:

$$\begin{matrix} 1.0007 & 0.3189 & 0.0000 & 0.0000 \\ 0.0044 & 1.0007 & 0.0000 & 0.0000 \\ 0.0000 & 0.0000 & 0.9647 & 0.3184 \\ 0.0000 & 0.0000 & -0.2174 & 0.9647 \end{matrix} \tag{4.23}$$

The end pole A matrix (travelling towards the inside of the wiggler):

$$\begin{matrix} 0.9928 & 0.2004 & 0.0000 & 0.0000 \\ 0.0000 & 1.0072 & 0.0000 & 0.0000 \\ 0.0000 & 0.0000 & 0.9981 & 0.2000 \\ 0.0000 & 0.0000 & -0.0822 & 0.9853 \end{matrix} \tag{4.24}$$

The end pole B matrix (travelling towards the inside of the wiggler):

$$\begin{matrix} 0.9989 & 0.2006 & 0.0000 & 0.0000 \\ 0.0520 & 1.0115 & 0.0000 & 0.0000 \\ 0.0000 & 0.0000 & 0.9923 & 0.1997 \\ 0.0000 & 0.0000 & -0.1307 & 0.9813 \end{matrix} \tag{4.25}$$

The whole wiggler from A to B:

$$\begin{matrix} 1.1230 & 2.0465 & 0.0000 & 0.0000 \\ 0.0745 & 1.0263 & 0.0000 & 0.0000 \\ 0.0000 & 0.0000 & -0.0851 & 1.1980 \\ 0.0000 & 0.0000 & -0.8327 & -0.0266 \end{matrix} \tag{4.26}$$

The whole wiggler from B to A:

$$\begin{matrix} 1.0263 & 2.0465 & 0.0000 & 0.0000 \\ 0.0745 & 1.1230 & 0.0000 & 0.0000 \\ 0.0000 & 0.0000 & -0.0266 & 1.1980 \\ 0.0000 & 0.0000 & -0.8328 & -0.0851 \end{matrix} \tag{4.27}$$

Notice that because of the asymmetry between the pole A and B, exchanging the direction of motion in the case of the whole matrix, diagonal elements are exchanged in the horizontal and vertical blocks, while off diagonal ones are unchanged.

4.3.4 Radiation integrals and other remarks

Two important remarks on the accuracy of the model: the first about the dependence of the wiggler optics on the orbit and the second on the contribution to the radiation integral.

As seen in Section 2 the terminal pole B has a strong sextupole, which generates linear focusing depending on the horizontal trajectory. A horizontal displacement of the trajectory of the order of the r.m.s. orbit value changes the effective $K1$ coefficient by about $K1 \approx K2 \cdot x = 4.7\ \mathrm{m}^{-2} \cdot 1.5\ \mathrm{mm} \approx 0.007\ \mathrm{m}^{-1}$. This variation affects mainly the horizontal dispersion function of the ring, which has its maximum right near the wigglers. The model is indeed corrected adding one further thin lens with a strength $K1$ adjusted fitting the measured dispersion.

The curvature of the poles should reproduce the wiggler contribution to quantum excitation, damping of the beam emittance and beam energy spread. The quantum excitation is in first approximation proportional to the third power of the curvature (the

	Beam property
$I_1 = \int D/\rho \; ds$	$\alpha_c = I_1/L$
$I_2 = \int 1/\rho^2 \; ds$	$U_0 = C_\gamma E^4 I_2/2\pi$
$I_3 = \int 1/\lvert\rho\rvert^3 \; ds$	$(\sigma_E/E)^2 = C_q \gamma^2 I_3/(2I_2 + I_4)$
$I_4 = \begin{cases} \int D/\rho \; (1/\rho^2 + 2K_1) \; ds \\ \int 2DK_1/\rho \; ds \end{cases}$	$\mathcal{J}_x = 1 - I_4/I_2$ $\mathcal{J}_E = 2 + I_4/I_2$
$I_5 = \int \mathcal{H}/\lvert\rho\rvert^3 \; ds$	$\epsilon_x = C_q \gamma^2 I_5/(I_2 - I_4)$

Table 4.6: Radiation integrals and their effects on beam properties. The entries for I_4 are for rings with sector magnets (upper) and rectangular (lower) magnets respectively.

radiation integrals I_3 and I_5 [28]). The value reproduced by the model for one wiggler is:

$$I_{3,\,model} = \sum_{poles} \frac{L_h}{\rho^3} = 1.381 \; m^{-2}; \tag{4.28}$$

while integrating the data measurements:

$$I_{3,\,actual} = \frac{1}{(B\rho)^3} \int_{wiggl} B^3(s) ds = 1.135 \; m^{-2}; \tag{4.29}$$

with a mismatch between model and actual wiggler of the 17 % that must be considered correcting the natural energy spread and the emittance calculated by MAD (see Tables 4.6-4.7).

		wigglers			bends + wigglers		
		actual	model	mismatch	actual	model	mismatch
I_2	(m^{-1})	4.937	5.603	13%	9.691	10.357	6%
I_3	(m^{-2})	4.540	5.524	17%	7.868	8.852	11%
I_4	(m^{-1})					1.222	
I_5	(m^{-1})	7.311	8.297	17%	10.316	11.302	9%

Table 4.7: Contribution to the DAΦNE radiation integrals only from wiggler magnets and both from bending and wiggler magnets. Contribution to I_1 and I_4 from wigglers is negligible.

Chapter 5

Lattice setting for FINUDA and KLOE

The model of the DAΦNE rings, which describes the new interaction regions and the modified wigglers discussed in the previous Chapter, has been used to calculate with the MAD program a new lattice for the FINUDA experiment installed in the second interaction region (IR2) in 2003. Some detail on the optics used in 2004 for KLOE is also reported.

5.1 Lattice set-up for collisions in FINUDA

The main optics features of the ring lattice are a lower emittance with respect to the original one ($\epsilon_0 = 0.4 \cdot 10^{-6}$ m·rad) and smaller beta functions ($\beta_x^* = 2$ m, $\beta_y^* = 2.5$ cm) at the FINUDA interaction point (IP2).

All these parameters contribute to increase the geometrical luminosity and to decrease the effect of parasitic crossings in IR2 as discussed in Chapter 3. In fact the smaller transverse bunch sizes improve the beam separation in the transverse plane measured in units of σ_x and σ_y, while the reduced horizontal beta further reduce the strength of the

parasitic beam-beam kicks.

The two interaction regions are not identical to each other, hence there is no periodicity or symmetry in the lattice of the DAΦNE rings, which in general helps the operation of a machine and also the optics calculation. Since the IRs take a large fraction of the ring circunference ($\approx 20\%$), it is not trivial at all to calculate betatron and dispersion functions symmetric as much as possible in the Long and Short sections of the ring and also around the IRs. In this way the operation and the handling of the machine is as much effective and simple as possible (calculation and application of closed orbit bumps with steering magnets, correction of the betatron tunes with quadrupoles...). The beta functions, the dispersion and the $\mathcal{H}$-invariant all along the ring are showed in Figures 5.1-5.2.

5.1.1 Injection section: betas, phase advance and dispersion

The horizontal beta function at the injection septum must be high enough to perform an efficient injection ($\beta_x > 6$ m). Nevertheless experimental observation has showed that the electromagnetic background in the experimental detectors is enhanced by high beta function values at the septum: the chosen value is then $\beta_x = 8$ m. Another constraint in the horizontal plane is the horizontal beta phase advance $\phi_x = \pi$ between the two injection kickers to produce a horizontal closed orbit bump of the stored beam at the injection. Two more quadrupoles with large aperture have been installed on the two kickers in order to improve the flexibility of the straight section set-up.

The section has non-vanishing dispersion, which does not affect the injection efficiency due to the small energy spread $\sigma_E/E_0 = 0.0004$ of the beam coming from the Accumulator. The value of the dispersion in the adjacent bending determines the momentum compaction α_c (Eq. 2.9), which is chosen as 0.02.

The horizontal optical functions (β_x, ϕ_x and D_x) are plotted in Fig. 5.3.

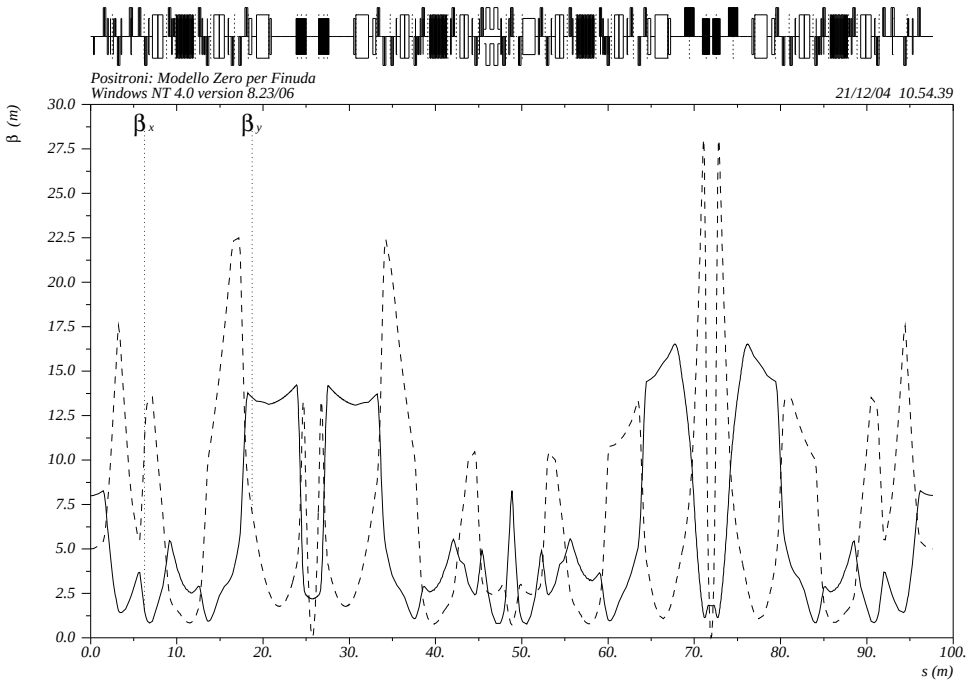

Figure 5.1: The beta functions along the main rings. The starting point is the at the injection septum, IP1 (KLOE) is at $s = 26$ m and IP2 (FINUDA) at $s = 72$ m.

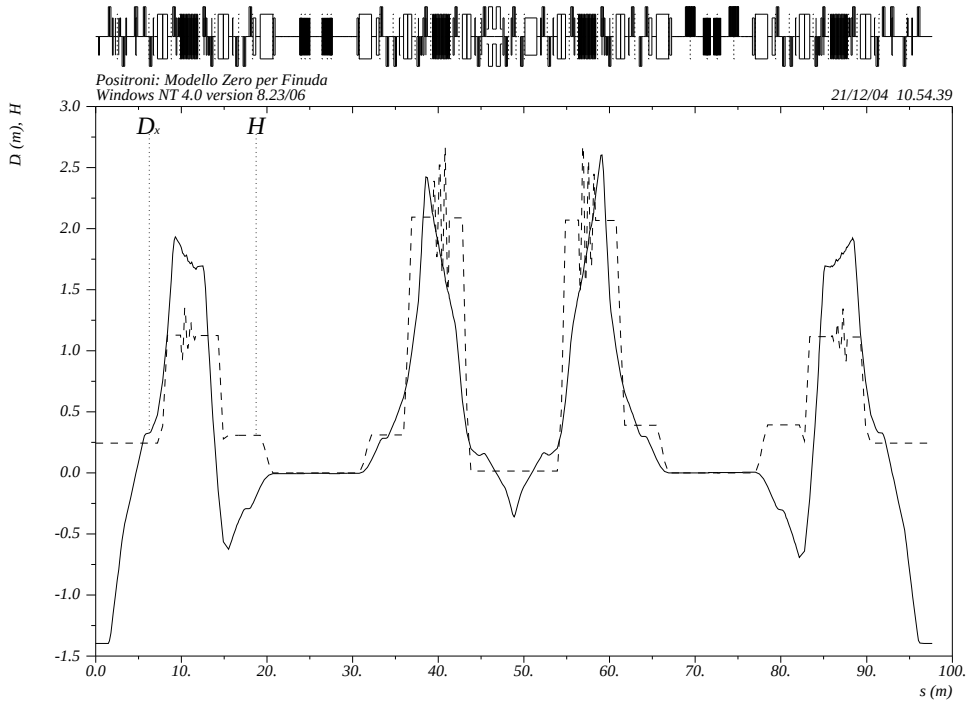

Figure 5.2: The dispersion function and the $\mathcal{H}$-invariant in the main rings.

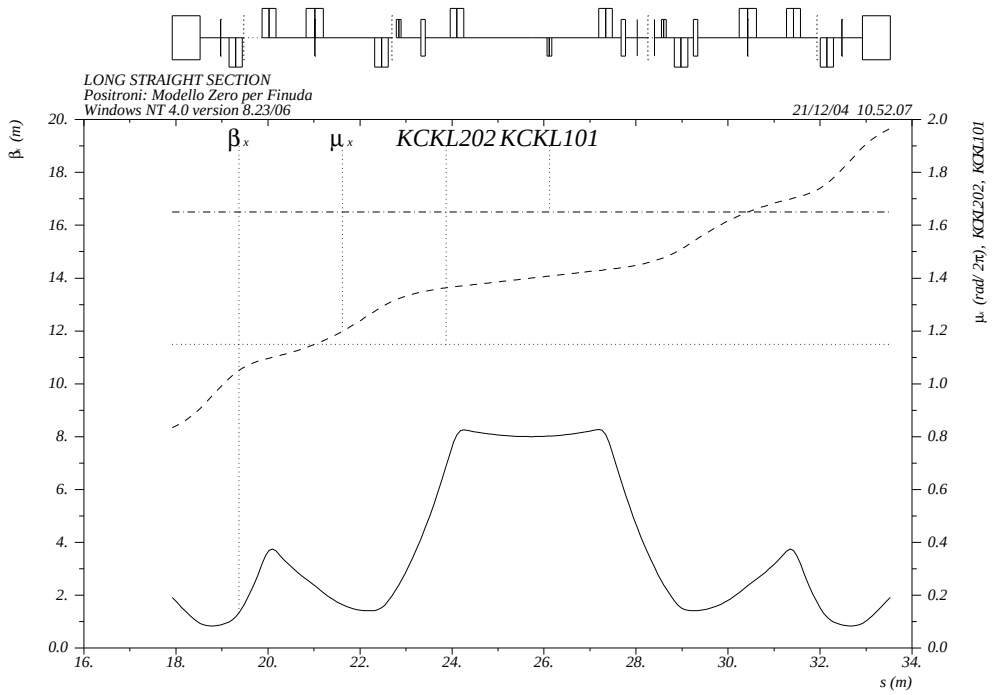

Figure 5.3: The horizontal beta function and phase advance in rad/π along the injection section: two horizontal markers indicate the phase at kickers locations, the phase is calculated from IP2.

5.1.2 Arc cell: chromatic sextupoles, dispersion and emittance

The arcs are the sections of the ring where the $\mathcal{H}$-invariant (Eq. 2.8) is different from zero (see Fig. 5.2). The wiggler magnets, positioned where the dispersion is maximum, increase the beam emittance up to an order of magnitude with respect to the emittance generated only by bending magnets. The wigglers work always near the maximum field to obtain strong damping, hence the emittance is modulated by varying the behaviour of the horizontal beta function and its derivative (β_x and α_x) in the dipoles in order to change the $\mathcal{H}$-invariant, whose integral throughout the ring determines the beam emittance as expressed in Eq. 2.7.

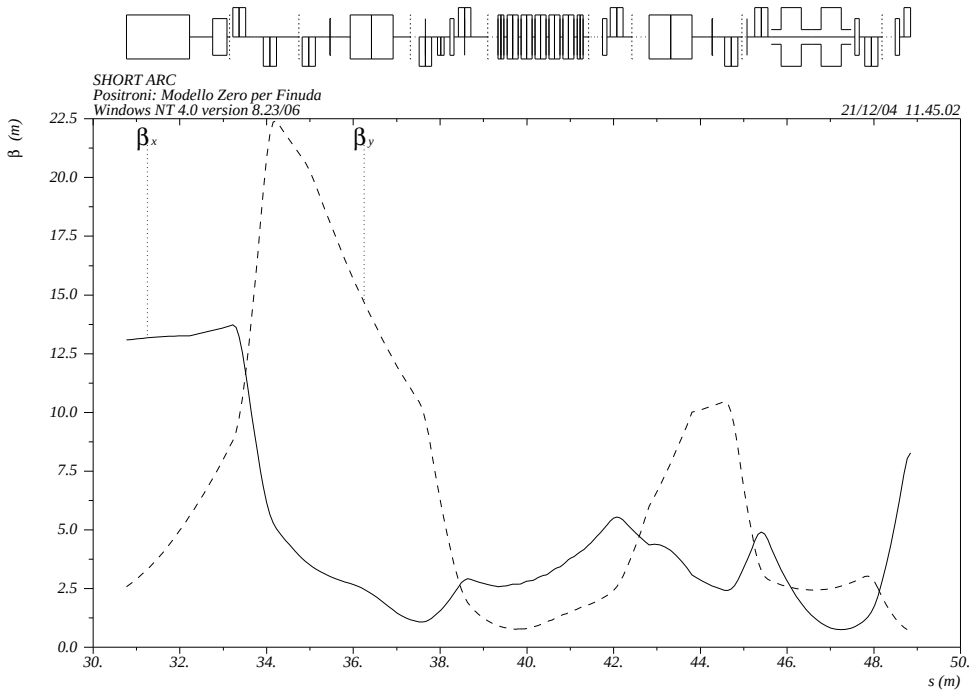

Figure 5.4: The beta functions in the Short arc and half the Short straight section where the RF cavity is located.

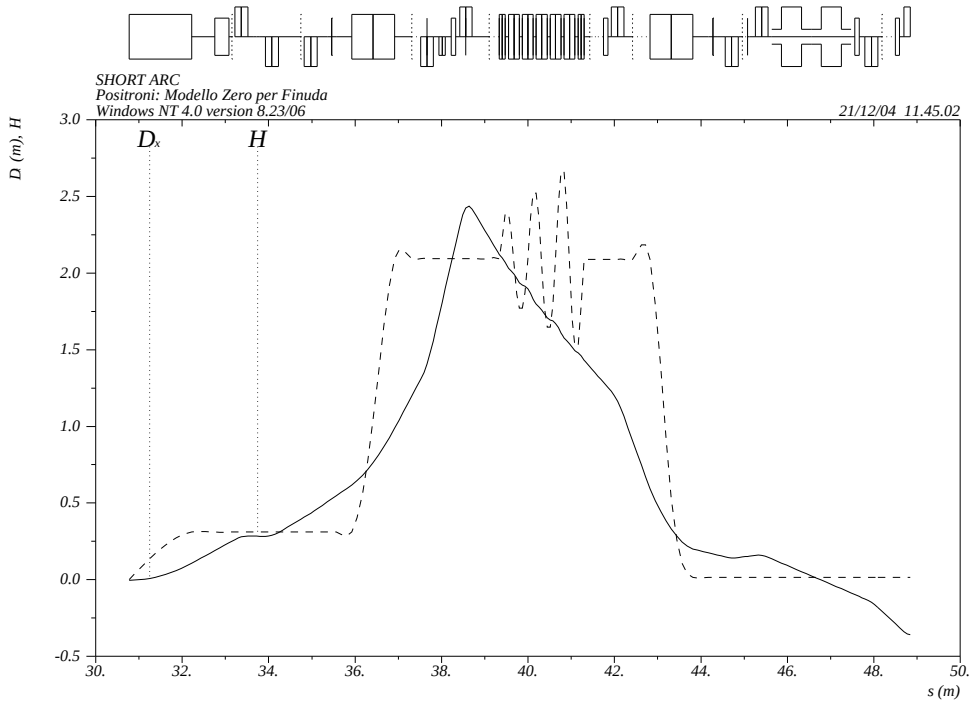

Figure 5.5: The dispersion function and the $\mathcal{H}$-invariant in the Short arc and half the Sort straight section where the RF cavity is located.

In each arc there is also a couple of sextupoles placed where the dispersion is not null to correct the horizontal and vertical natural chromaticity of the ring. The beta functions are well separated at sextupoles positions in order to have $\beta_x \geq \beta_y$ (at least 4 times) at the position of the sextupole used to correct the horizontal chromaticity and the converse at the position of the sextupole correcting the vertical chromaticity. Finally another constraint is given by the narrow vertical aperture of the vacuum chamber in the wigglers (35 mm, while the average aperture along the ring is 80 mm) for which a low vertical beta is needed ($\beta_y \approx 1$ m in the wiggler). Figures 5.4-5.5 show as an example β_x, β_y, D_x and $\mathcal{H}$ in more detail for one of the Short arcs.

5.1.3 Interaction regions: betas and trajectories

During the FINUDA run the FINUDA detector is installed in IR2 while in IR1 the KLOE detector cannot rolled off. Therefore the two interaction regions are low-beta insertions.

The vertical beta function at IP2 for collisions in FINUDA is $\beta_y^* = 2.5$ cm and the peak value at the D quadrupole $\beta_y^{max} = 28.5$ m.

The other interaction region (IR1) is also a low-beta insertion (the quadrupoles being permanent magnets), but the vertical beta function at the interaction point (IP1) is increased as much as possible ($\beta_y^* = 8$ cm) in order to limit the vertical chromaticity generated by the first D permanent quadrupole where the vertical beta is maximum ($\beta_y^{max} = 13$ m) .

The crossing angle in IR2 is 13.5 mrad because of the FD doublet, while the crossing angle in IR1 is increased to 16.5 mrad thanks to the new DF configuration. The horizontal and vertical betatron functions of the two low-beta regions are summarized in Table 5.1.

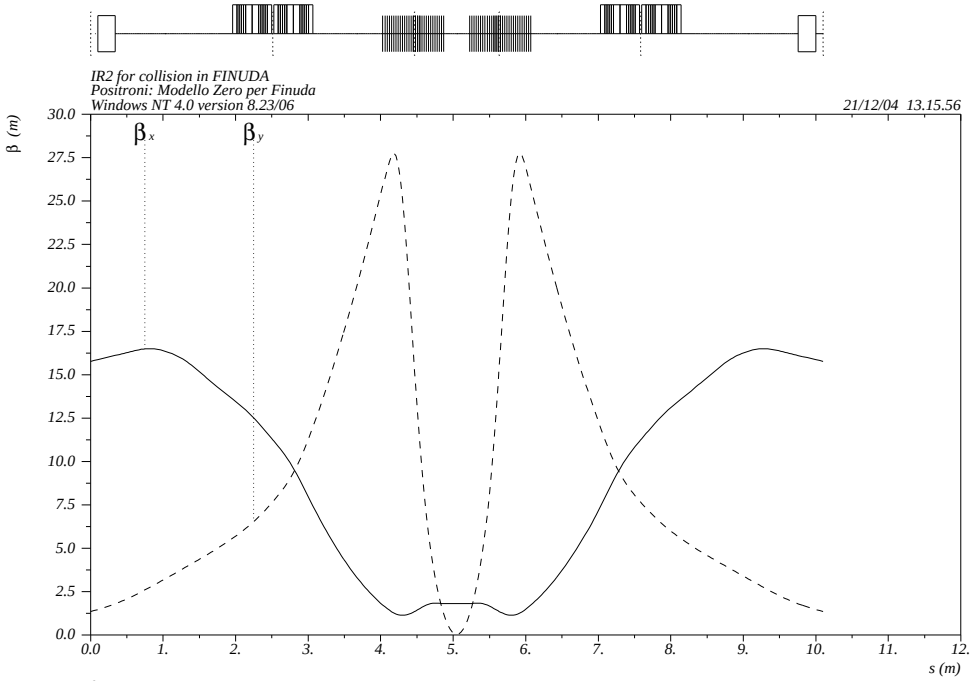

Figure 5.6: The beta functions in IR2 for collision in FINUDA.

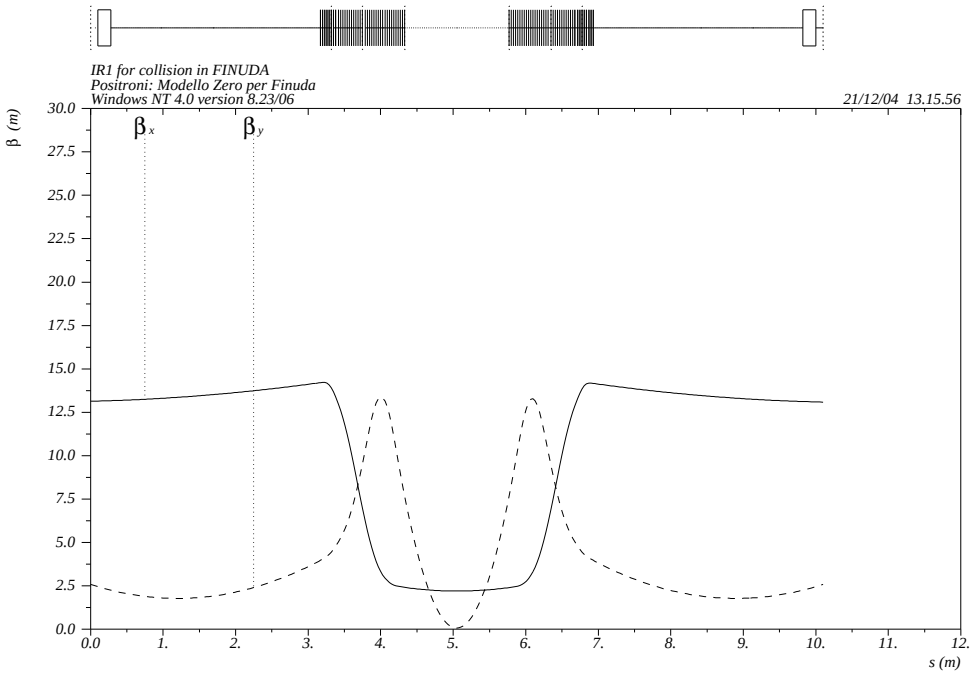

Figure 5.7: The beta functions in IR1 for collision in FINUDA.

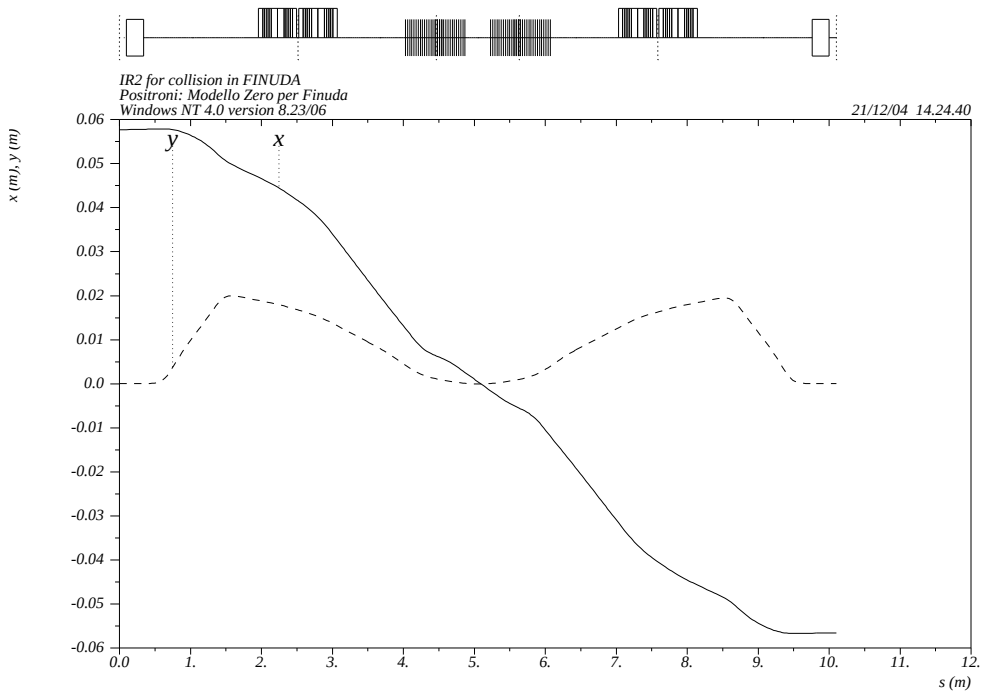

Figure 5.8: The horizontal and vertical trajectory along IR2 for collisions in FINUDA. The horizontal crossing angle is 13.5 mrad.

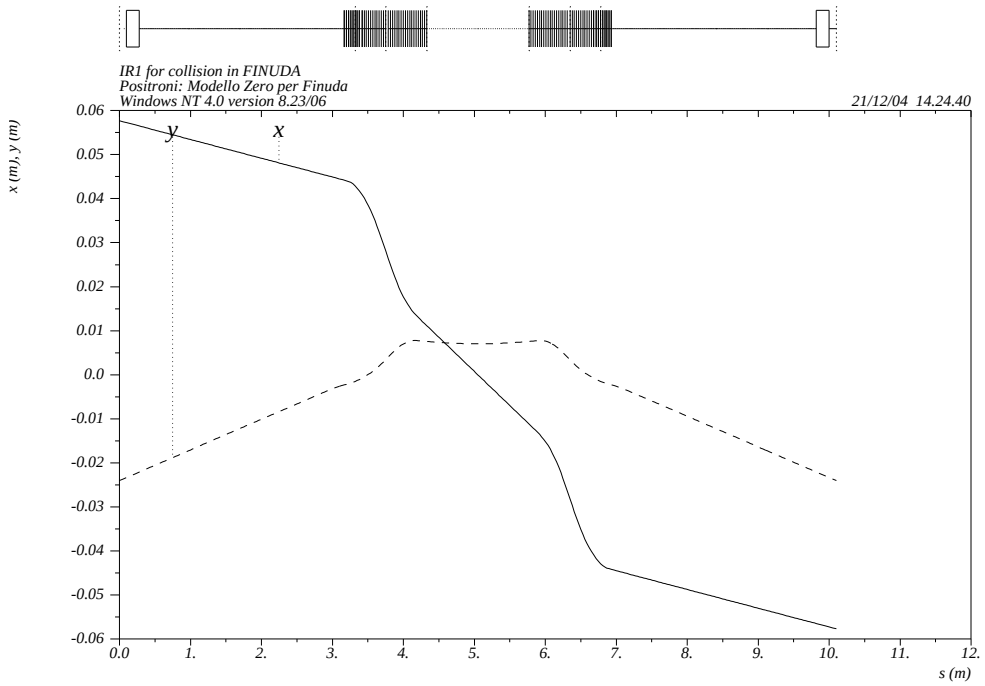

Figure 5.9: The horizontal and vertical trajectory along IR1 for collisions in FINUDA. The horizontal crossing angle is 16.5 mrad and the vertical separation between the beams at IP1 is ± 2 mm.

5.2 Interaction regions for collisions in KLOE

The lattice that has been used for the KLOE run in 2004 is very similar to the lattice used for FINUDA in 2003, except for the interaction regions. In the first interaction region the KLOE solenoid and the compensators are switched on, while in the second interaction region the FINUDA detector and the low-beta permanent quadrupole doublet are rolled out and replaced by a drift section.

The vertical beta function at the KLOE interaction point is squeezed up to the hour-glass limit ($\beta_y^* \approx \sigma_z$) and the horizontal crossing angle (tuneable in a large range between 11.5 and 18.5 mrad) has been tuned at 16.5 mrad in the first weeks of operation as the best compromise between the luminosity performances (geometrical reduction and low effect of the parasitic crossings) and the electromagnetic background in the experimental detector.

The opposite interaction region is not a low-beta insertion, on the contrary the minimum of the beta functions are increased resulting in a lowering ("detuning") of the phase advances. This configuration [8, 9] allows a large vertical separation of the opposing beams in the interaction regions (up to ± 10 mm at IP2, to be compared with the horizontal size $\sigma_x^* \approx 1$ mm) where the beams are not in collision decreasing the effect of parasitic crossing and chromaticity in IR2.

	Collisions in FINUDA		Collisions in KLOE	
	IR1	IR2	IR1	IR2
β_x^* (m)	2.5	2.0	2.0	12.5
β_y^* (m)	0.0080	0.0025	0.0017	2.8
β_y^{max} (m)	13.4	28.5	33.2	9.2

Table 5.1: The beta functions at the interaction points and at the first D quadrupole of the low-beta insertion for collision in FINUDA (2003) and in KLOE (2004).

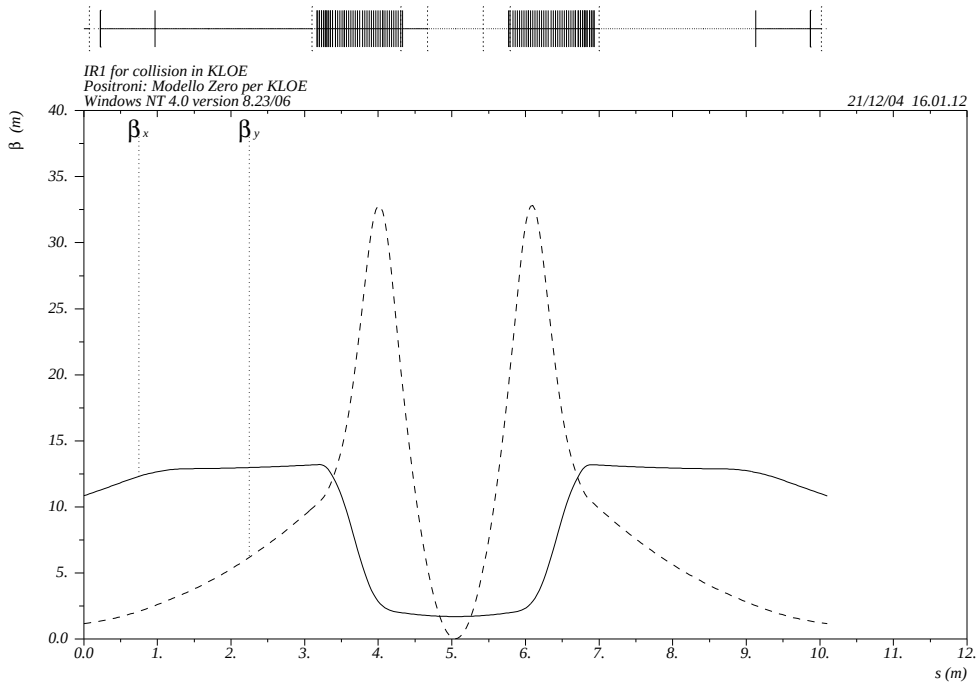

Figure 5.10: The beta functions in IR1 for collision in KLOE.

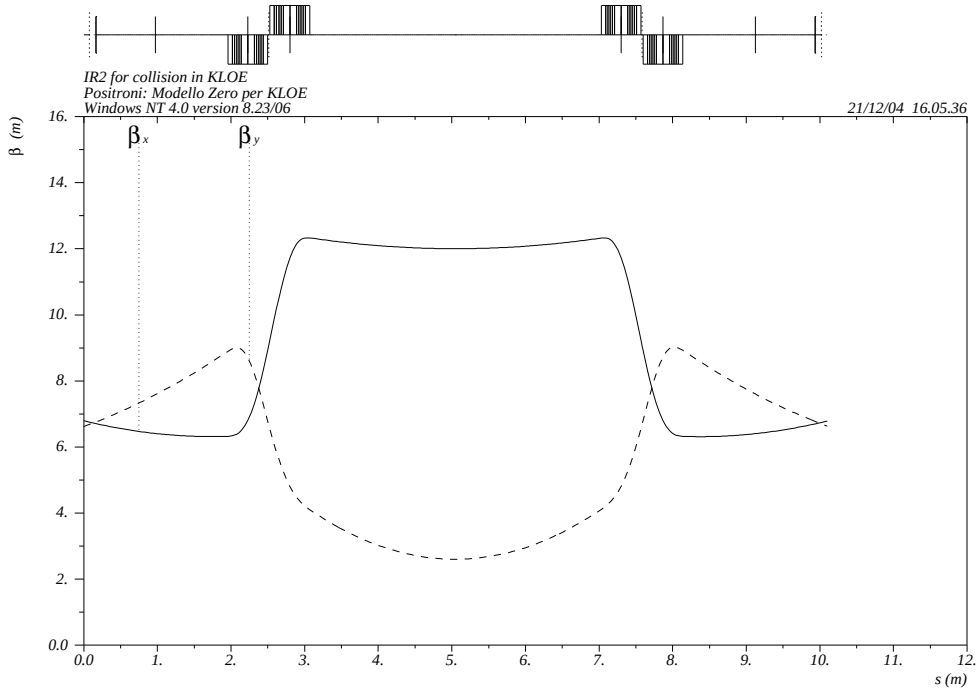

Figure 5.11: The "detuned" beta functions in IR2 for collision in KLOE.

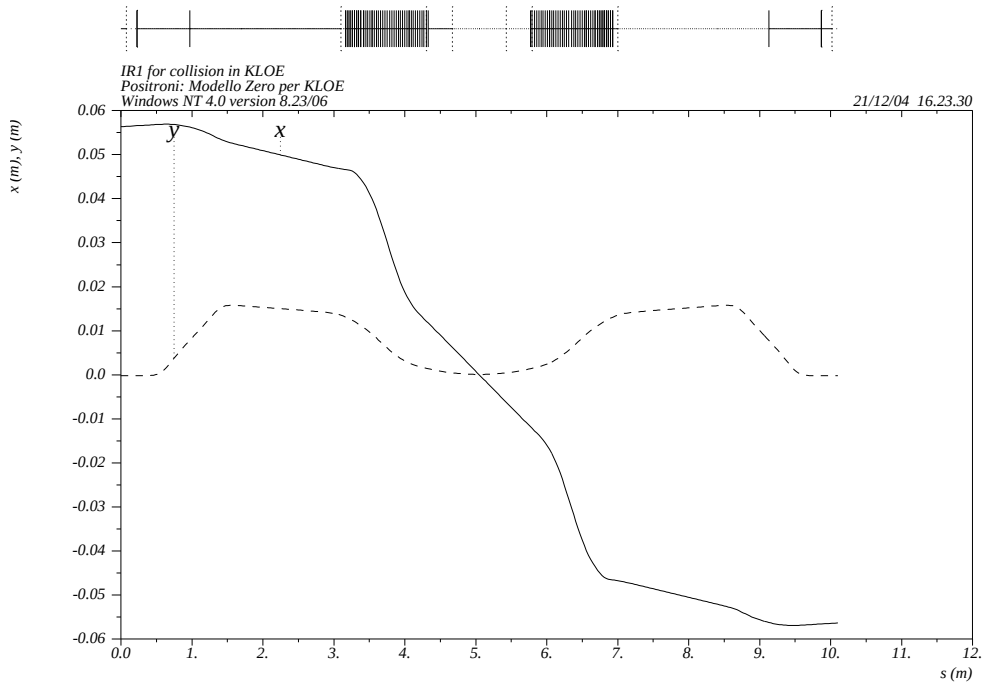

Figure 5.12: The horizontal and vertical trajectory along IR1 for collisions in KLOE. The horizontal crossing angle is 16.5 mrad.

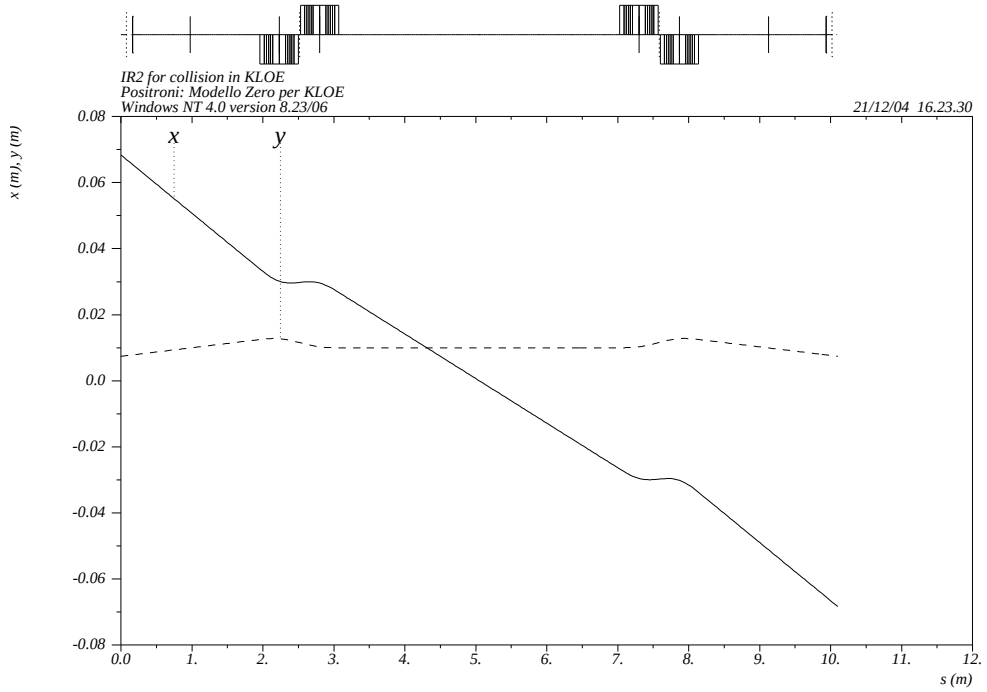

Figure 5.13: The horizontal and vertical trajectory along IR2 for collisions in KLOE. The horizontal crossing angle is 13.5 mrad and the vertical separation between the beams at IP2 can be varied easily up to ± 10 mm.

Chapter 6

Optics measurements and model results

After a short presentation of the main techniques used at DAΦNE for the beam optics measurements, the dispersion and betatron functions measured both in the electron and the positron ring are compared with the beta functions calculated with the MAD model described in the Chapter 5.

6.1 Optics measurements at DAΦNE

6.1.1 Beam position monitors

In DAΦNE there are 37 beam postion monitors (BPM) of electrostatic pick-up type per ring and 6 + 4 in the interaction regions, with different designs, that fit the dimensions and the shape of the vacuum chamber along the rings.

The horizontal and vertical beam positions are calculated from the induced voltages on the BPM electrodes. For instance for the monitor scheme in Fig. 6.1 the transverse

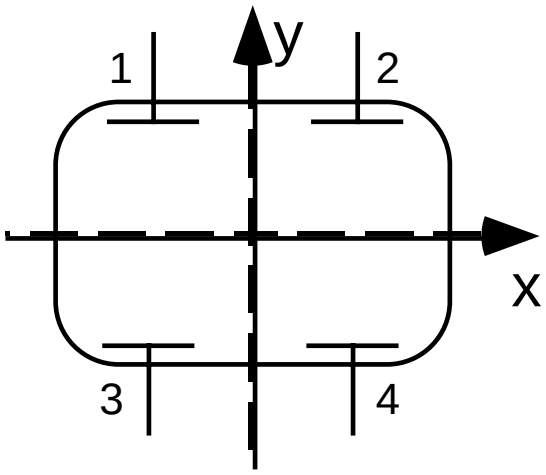

Figure 6.1: Schematic view of a BPM rectangular type. From voltages V_1, V_2, V_3, V_4 on the electrodes the transverse positions are deduced.

coordinates of the beam are:

$$U = \frac{V_2+V_4-V_1-V_3}{V_2+V_4+V_1+V_3}$$
$$V = \frac{V_1+V_2-V_3-V_4}{V_2+V_4+V_1+V_3}. \tag{6.1}$$

Because of the non-linear response of the monitor with respect to the beam displacement, the pseudo-positions U and V are corrected using a non-linear function that reconstructs accurately the beam position:

$$x = g_x(U,\ V)$$
$$y = g_y(U,\ V) \tag{6.2}$$

The $g(U,\ V)$ functions are polynomials whose coefficients are obtained from a least squares fit of the calibration measurements of the monitors [44]. The detecting electronics has been developed by Bergoz Beam Instrumentation System for DAΦNE [25]: it is made by a superheterodyne receiver which converts the 240^{th} harmonic frequency (twice the accelerating RF frequency) of the induced beam signal in a intermediate frequency of 21.4 MHz before the amplitude measurement. The line output provides two voltages U,

V that are processed by the software to obtain the horizontal and vertical positions x and y.

The acquisition system is developed in the VME standard. The signals are measured by a multiplexer FET HP E1352A and a digital multimeter HP 326B, controlled by dedicated processors. The DAΦNE second level control system collects the position data from these peripheric units and they are used by the third level for the reconstruction of the orbit and for the analysis programs. The beam orbit (i.e. the horizontal and vertical positions at every BPM) is acquired with frequency of 5 Hz.

The error on the measurement of the beam position with respect to the centre of the vacuum chamber depends on several factors: mechanical tolerances of the monitor installation, electrical offsets due to mismatch between the capacitances of the buttons, error from the reconstruction function and the electronic noise. In the orbit difference measurements only the error from the electronic noise remains (also from the reconstruction function if the orbit displacement is beyond ±10 mm from the centre) and r.m.s. errors of 15 μm are obtained averaging over 10-15 orbit measurements [45].

	r.m.s error
Mech. tolerances	100 μm
Electrical offsets	10 μm
Recontruct. function ($\|x\| < 10\ mm$)	2 μm
Recontruct. function ($10\ mm < \|x\| < 20\ mm$)	25 μm
Electronic noise	10 μm

Table 6.1: R.m.s errors on the measured beam position with respect to the centre of the vacuum chamber (averaged over the different BPM types).

6.1.2 Dispersion measurements

The dispersion function in a ring is obtained from the orbit change induced by varying the radio-frequency. A shift of the radio-frequency Δf_{RF} changes the beam energy by a quantity[1]:

$$\frac{\Delta E}{E_0} = -\frac{1}{\alpha_c}\frac{\Delta f_{RF}}{f_{RF}}. \tag{6.3}$$

Since $x_\epsilon(s) = D_x(s) \cdot \Delta E/E_0$, the dispersion function at the beam position monitors is deduced from the measured orbit change $x_\epsilon(s)$:

$$\eta(s) = -\alpha_c \frac{x_\epsilon(s)}{\Delta f_{RF}/f_{RF}}. \tag{6.4}$$

The radio-frequency $f_{RF} = 368.268\ MHz$ is generally varied by $\Delta f_{RF} = 0.010\ MHz$ and is known with an accuracy of 2 Hz. The corresponding orbit displacement x_ϵ varies along the ring from some micron to 1-2 mm with an error of the order of $5 - 10\ \mu$m.

The value of the momentum compaction is deduced from the expression [22]:

$$\alpha_c = \frac{f_{sin}^2}{f_{rev}^2}\frac{2\pi E_0}{h\ eV_{cav}\cos\phi_s} \tag{6.5}$$

where f_{sin} is the synchrotron frequency (a typical value is about 30 KHz), which is measured with a spectrum analyzer with an error of the order of 0.1 KHz, f_{rev} is the revolution frequency (known with an accuracy of 1 Hz, $h = 120$ is the harmonic number, $V_{cav}\cos\phi_s$ is the RF voltage slope known with an accuracy of 5 %, which thus gives the main contribution to the error on α_c. A typical measurement of the momentum compaction for the

[1]The betatron oscillations around the reference orbit does not produce at first order in x and y a change in the trajectory length. On the contrary the trajectory given by the dispersion $D_x(s)$, generated by a displacement of the energy, changes the length of the equilibrium orbit. The *momentum compaction* factor is:

$$\alpha_c = \frac{\Delta L/L}{\Delta E/E_0} = \frac{1}{L}\oint \frac{D_x(s)}{\rho(s)}ds\ .$$

The orbit length is $L = c\,\frac{h}{f_{RF}}$, then $\Delta L/L = -\Delta f_{RF}/f_{RF}$.

DAΦNE rings gives $\alpha_c = 0.020 \pm 0.001$.

The contribution due to f_{RF} in the error propagation in the dispersion measurement is negligible, thus the error on D_x is:

$$\delta(D_x) = \left| \frac{x_\epsilon}{\Delta f_{RF}/f_{RF}} \right| \delta(\alpha_c) + \left| \frac{\alpha_c}{\Delta f_{RF}/f_{RF}} \right| \delta(x_\epsilon) \tag{6.6}$$

the first term is the 5% of the dispersion (from few millimetres to $5 - 10$ cm), the second is about 7 mm.

Betatron tunes Q

The fractionary part of the horizontal and vertical betatron tune Q_x and Q_y is measured giving to the beam a RF transverse excitation with two stripline kickers and measuring

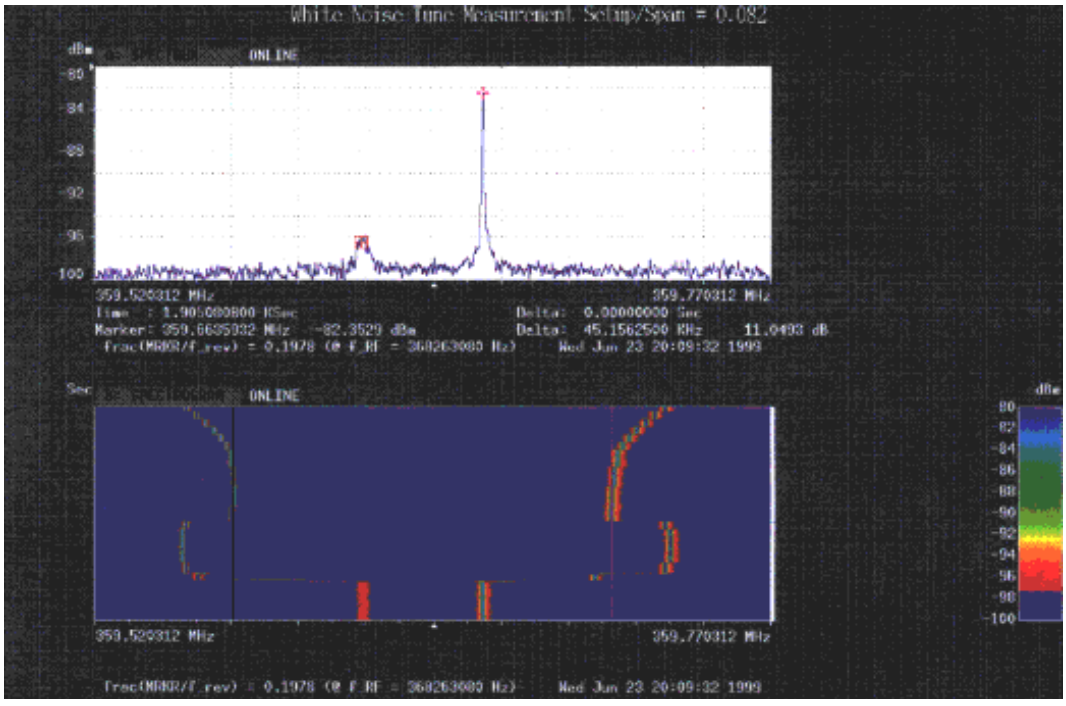

Figure 6.2: An example of the frequency spectrum as it is shown by the spectrum analyzer: the two peaks correspond to the horizontal and vertical betatron tunes.

the response of the beam in the excited plane with a electrostatic button monitor similar to the beam position monitors described above.

The beam is excited at all frequencies with a white noise generator and it responds only at its own oscillation frequencies. The signal is extracted with wide band button electrodes and is sent to an spectrum analyzer (HP 70000 system). The output at a intermediate frequency is processed by a FFT analyzer HP 3587S.

Figure 6.2 represents the beam spectrum as is shown by the DAΦNE control system. The measurement resolution of Q is $1 \cdot 10^{-4}$.

6.1.3 Beta measurements

In a storage ring the betatron functions can be measured at the quadrupole positions. The value of the beta function is obtained from the betatron tune shift when the quadrupole strength is varied.

In thin lens approximation, a quadrupole gradient change Δk generates a betatron tune shift $\Delta Q_{x,y}$ [23, 41, 52] proportional to the beta function at the quadrupole position:

$$\Delta Q_{x,y} = \pm \frac{1}{4\pi} \Delta k L \, \beta_{x,y} \tag{6.7}$$

where L is the magnetic length of the quadrupole.

The main contribution to the measurement error comes from the thin lens approximation used to estimate the beta. A reliable value of the error on the measured beta functions is 1 m [5] for all DAΦNE quadrupoles.

6.2 DAΦNE model results

Two sets of measurements taken on November 25 2003 (electron ring) and December 4 2003 (positron ring) are reported as an example. The horizontal and vertical beta functions from the model are in very good agreement with the measured beta functions.

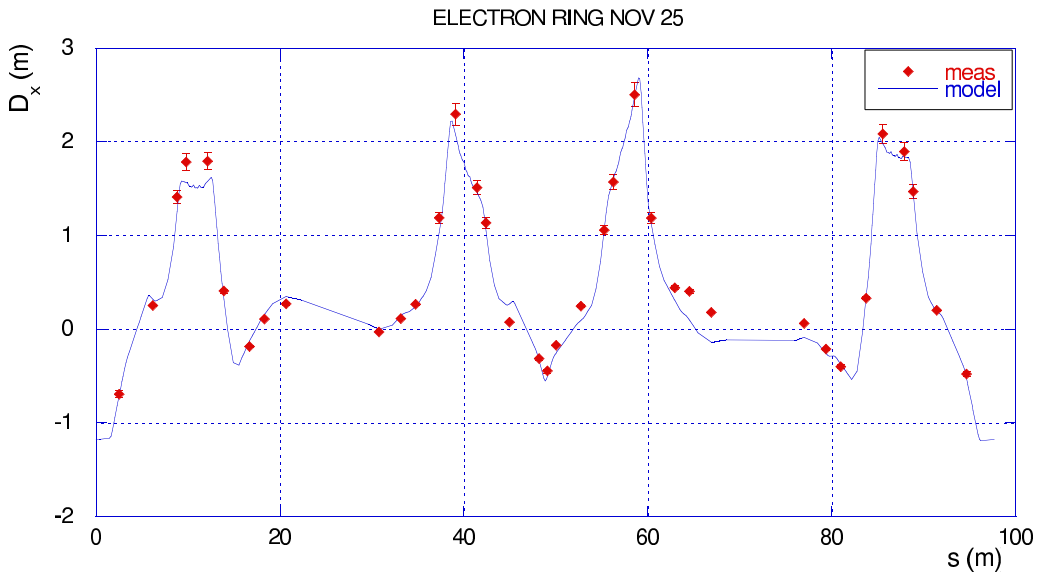

Figure 6.3: Dispersion function in the electron ring: $\chi^2/dof = 3.04$.

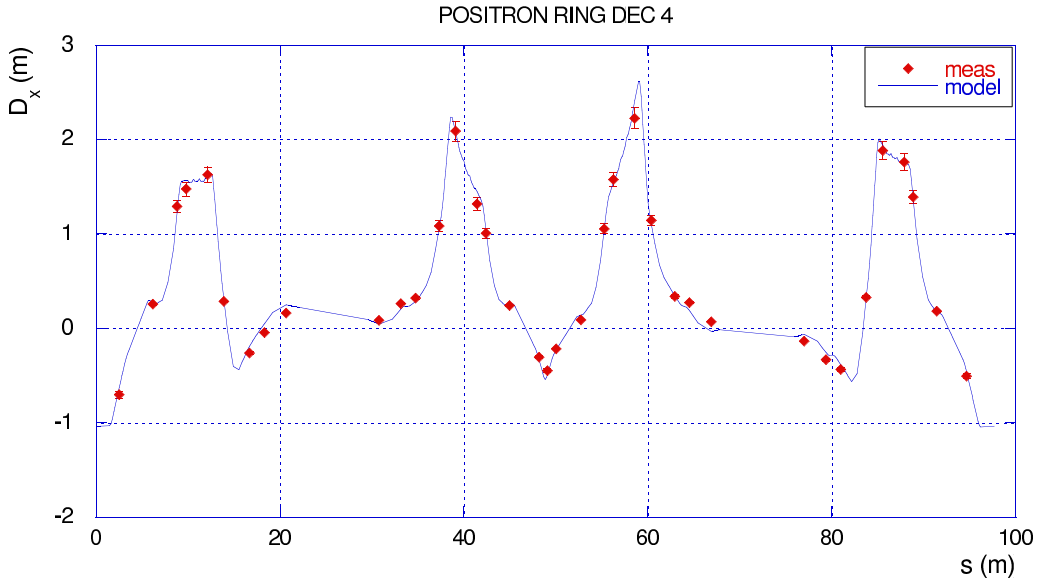

Figure 6.4: Dispersion function in the positron ring: $\chi^2/dof = 2.11$.

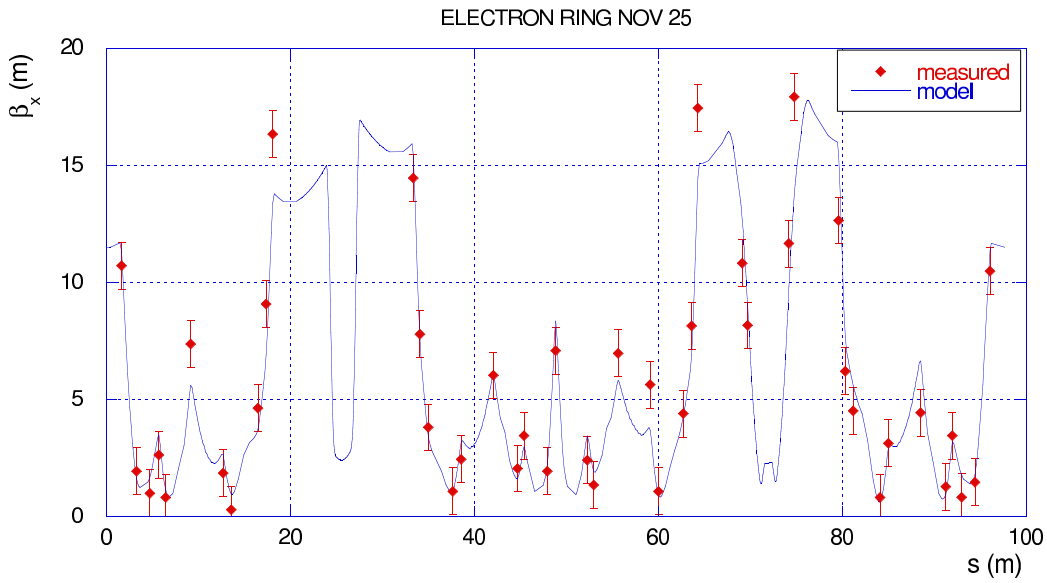

Figure 6.5: Horizontal beta function in the electron ring: $\chi^2/dof = 1.62$.

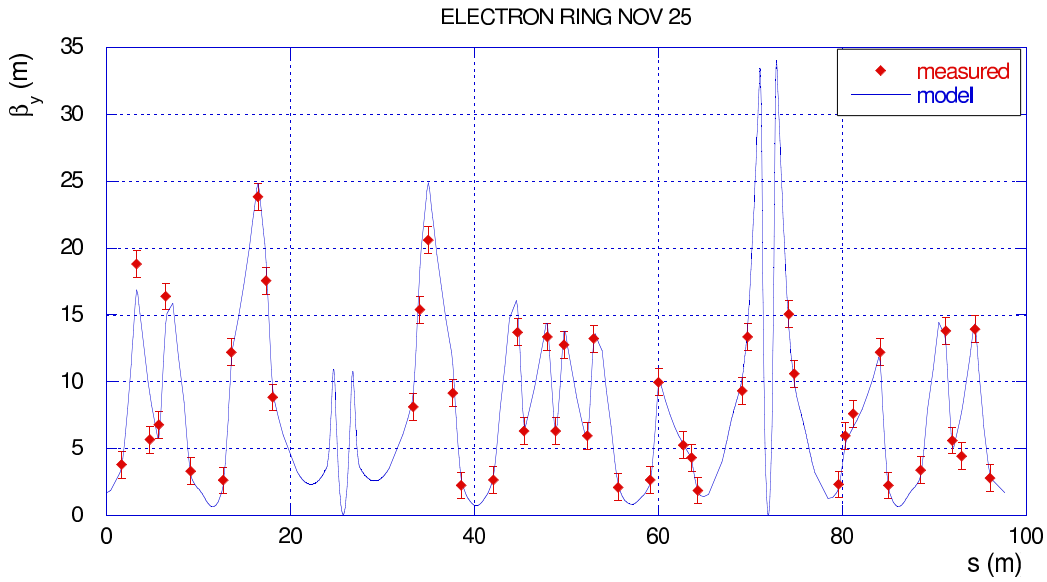

Figure 6.6: Vertical beta function in the electron ring: $\chi^2/dof = 1.33$.

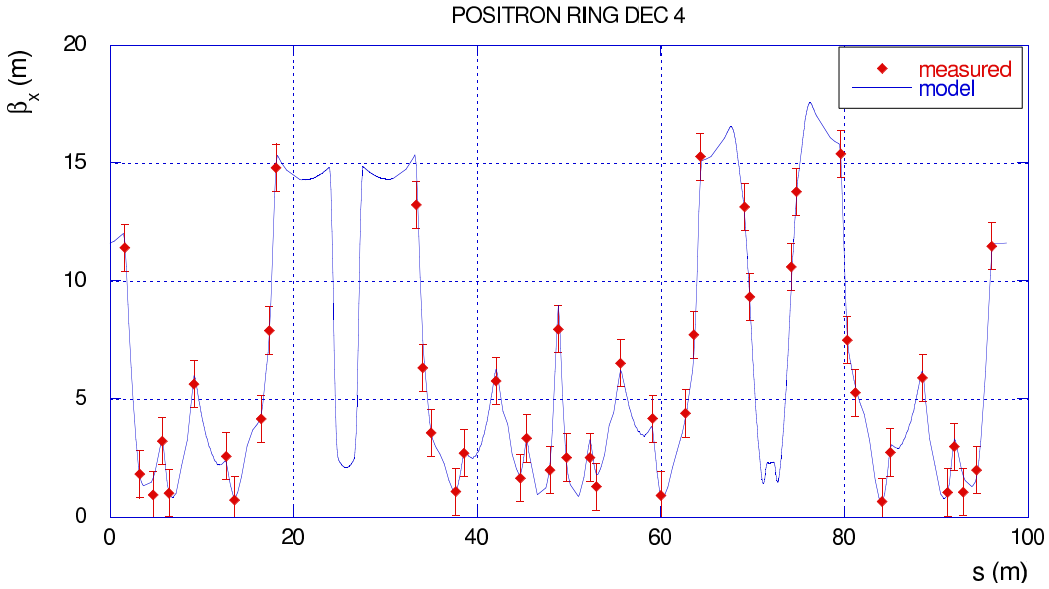

Figure 6.7: Horizontal beta function in the positron ring: $\chi^2/dof = 1.44$.

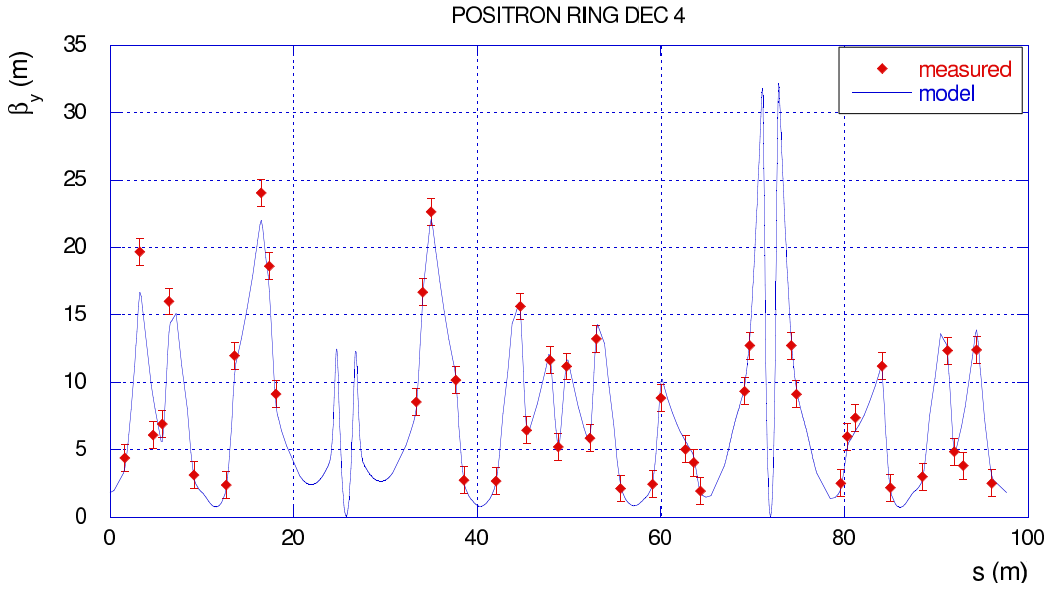

Figure 6.8: Vertical beta function in the positron ring: $\chi^2/dof = 1.19$.

Chapter 7

Beam based alignment

A Beam Based Alignment (BBA) procedure has been implemented for the DAΦNE quadrupoles in 2003.

The motivations for a set of BBA measurements at DAΦNE is the optimization of the orbit correction with the dipole correctors. Large horizontal quadrupole misalignments need large kicks from the corrector dipoles to steer the orbit distortion, which perturb the optics of the rings and generate additional spurious dispersion. These model dependent measurements are aimed at identifying particularly large misalignments of the quadrupole centres with respect to the adjacent beam position monitors (BPM) so that they may be mechanically realigned.

The typical data acquisition process takes 12-15 minutes per ring (41 quads and 37 BPMs). The lattice is simulated with the MAD model and the analysis performed with an algorithm written with Matlab.

The first BBA data were taken in September 2003 at the start of the run for FINUDA. The analysis revealed a short circuit in the winding of two quadrupoles of the electron ring just installed in the previous machine shutdown and a 2.5 mm horizontal displacement of

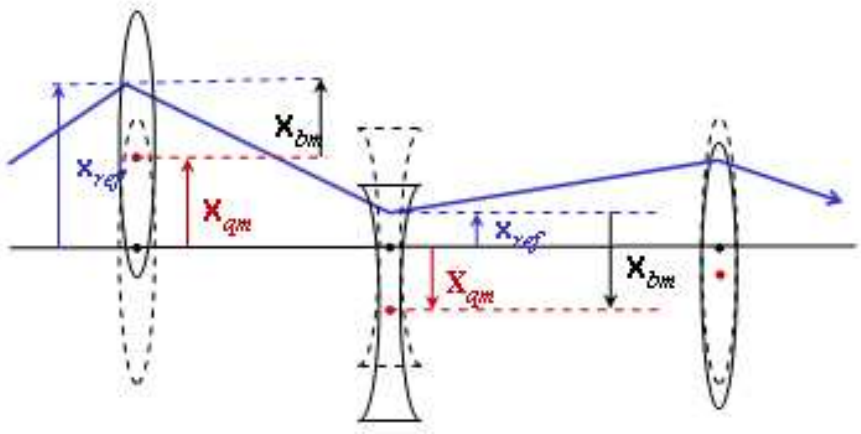

Figure 7.1: Definition of the BPM-to-quadrupole and Beam-to-quadrupole offsets.

the quadrupoles in the Long straight section of the electron ring also rearranged during the shutdown.

After the adjustment of the alignments further sets of measurements, taken in December 2003 and at the start of the KLOE run in April 2004, confirm that the residual beam to quadrupole horizontal offsets are smaller than 2 mm and the vertical ones smaller than 1 mm in both rings.

The BBA is a technique of great interest for future linear collider that will have demanding alignment and stability requirements in order to achieve the low vertical emittance necessary for very high luminosity [39, 51].

7.1 The BBA technique

Beam based alignment technique in storage rings commonly uses the closed orbit change with respect to variations of the quadrupole strength to determine the beam position with respect to the magnetic centre of the quadrupole. Typically BPMs are located near the quadrupole magnets. This configuration allows a direct measure of the BPM to quadrupole offset by steering the closed orbit at the quadrupole position with the dipole

correctors until there is no response to the change in quadrupole strength. The reading recorded at the adjacent BPM is the quadrupole to BPM offset. Figure 7.1 shows a schematic view of the offset definitions.

In DAΦNE the nearest BPM is in general some distance d from the middle of the quadrupole (about 12-15 cm apart), thus, even if the beam is passing through the quadrupole centre, it may be passing through the BPM with an angle x' which can produce an error $\delta x_{qb} = x' \cdot d$ in the offset measurements. Moreover there are 4 quadrupoles in each Long straight section which do not have any BPM nearby.

Hence in the DAΦNE case it is better to determine the beam offsets with respect to the quadrupole centres for a *given reference orbit* using the ability to calculate the change in closed orbit throughout the ring lattice with the optics model. In a second step an assessment of the BPM to quadrupole offsets is possible under some assumption and approximation that are discussed below.

7.1.1 Closed orbit response to quadrupole strength variation

The horizontal case is discussed. Similar considerations hold also for the vertical case.

In a linear machine without coupling, a beam passing through a quadrupole with a horizontal offset x_{bq} with respect to the magnet centre receives a kick $\Delta x'_0 = -K x_{bq}$, where K is the integrated quadrupole strength (Eq. 4.3), correspondig to an effective dipole error located at the quadrupole position s_0. The closed orbit distortion generated by the quadrupole kick all along the ring is expressed by the well known formula for a small dipole error [23]:

$$\Delta x(s) = \frac{\Delta x'_0 \sqrt{\beta_x(s)\beta_x(s_0)}}{2 \sin \pi Q_x} \cos\left(\phi_x(s) - \phi_x(s_0) - \pi Q_x\right). \tag{7.1}$$

For a beam off-centre with respect to the quadrupole we distinguish three terms coming

respectively from the offset, from the closed orbit response, from the focusing:

$$\Delta x(s) = -x_{bq} C_{12}(s; s_0) K; \tag{7.2}$$

where the closed orbit response $C_{12}(s; s_0)$ is:

$$C_{12}(s; s_0) = \frac{\sqrt{\beta_x(s)\beta_x(s_0)}}{2 \sin \pi Q_x} \cos\left(\phi_x(s) - \phi_x(s_0) - \pi Q_x\right). \tag{7.3}$$

Hence the beam to quadrupole offset x_{bq} can be deduced from the response of the closed orbit to a change in the quadrupole strength K.

The measurement procedure is carried out in three steps:

1. starting from a given reference orbit in the machine, the strengths of the quadrupoles are individually varied and the respective difference orbits at each BPM are recorded in a matrix format;

2. the same orbit changes are simulated in the MAD model simulating an arbitrary displacement of the regarded quadrupole;

3. the beam to quadrupole offsets x_{bq} are determined scaling the modelled orbit changes in order to fit the measured orbit changes in a least squares sense.

Fitting the changes in the orbit due to a change in the quadrupole strength must take into account two contributions: the first is from the change in the field seen by the beam off-centre with respect to the quadrupole; the second is from the change in the focusing.

The expression for the change in the horizontal orbit is then [50]:

$$\Delta x_{co}(s) = -x_{bq} \frac{C_{12}^{(1)}(s; s_0) K^{(1)} - C_{12}(s; s_0) K}{1 - C_{12}(s_0; s_0) K}; \tag{7.4}$$

where $\Delta x_{co}(s)$ is the change in the closed orbit at location s in the lattice, x_{bq} the initial offset of the beam with respect to the quadrupole centre (which we want to measure), K the initial integrated quadrupole focusing, $K^{(1)}$ the integrated focusing after the change in quadrupole strength. The closed orbit response C_{12} must be calculated both for the original quadrupole setting and for the quadrupole strength after variation. A similar expression holds for the vertical plane:

$$\Delta y_{co}(s) = -y_{bq}\frac{C_{34}^{(1)}(s;s_0)K^{(1)} - C_{34}(s;s_0)K}{1 - C_{34}(s_0;s_0)K}. \tag{7.5}$$

7.2 Experimental equipment and data taking

The BBA data taking is fully integrated in the DAΦNE control system and is performed with the same program adopted for the usual acquisition of the closed orbit response matrix to dipole correctors changes. The program has been upgraded adding the option of selecting either the dipole corrector currents or the quadrupole ones to be varied.

The DAΦNE beam position monitors used for orbit measurements have been already presented in Section 6.1.1.

7.2.1 Power supply control

There two types of quadrupole power supplies, one for the Small quadrupoles and another for the Large quadrupoles. The setting resolution and the readout resolution of the current for the different types are reported in Table 7.1 [42]. Errors coming from the resolution of power supplies in the alignment measurement are in general negligible. The power supplies are controlled through a serial board on VME bus. Dedicated CPUs of the second level of the control system set and read the currents.

Quad type	Max current	Setting resolution	Readout resolution
Small	585 A	±6 mA	±6 mA
Large	175 A	±2 mA	±2 mA

Table 7.1: The power supply technical specifications for the DAΦNE quadrupoles.

7.2.2 Closed-orbit response measurement

Figure 7.2 shows the window of the LabView program of the DAΦNE control system that measures the closed orbit response. The procedure carried out by the program for the orbit response to quadrupole changes is the following:

- reference (horizontal and vertical positions) orbit acquisition, averaging over a given number of orbits (10-15);
- reading of the current provided by the power supply to the quadrupole;
- change in quadrupole current is applied;
- new closed orbit is acquired;
- the difference $x_{new} - x_{ref}$ is written as a row of the response matrix;
- back to the original quadrupole current value.

This sequence is iterated for each one of the 41 quadrupoles and finally all the orbit changes are saved in a matrix format: one row each quadrupole orbit change and one column each BPM. The complete data acquisition takes about 10-15 min. per ring.

7.3 Analysis and errors

The BBA procedure has been applied to all electromagnetic quadrupoles in the DAΦNE rings but the four ones of the second interaction region where the design trajectory passes

Figure 7.2: The LabView program window of the DAΦNE control system that measures the closed orbit response matrix.

of axis. Closed orbit changes are formed with the MAD optics model of the main rings by simulating a fictitious displacement of the beam with respect to the quadrupole centre of 1 mm in the horizontal and vertical direction.

The analysis is performed assuming the local betatron coupling is corrected (that means the horizontal and vertical orbit changes are generated respectively only by the horizontal and vertical offset of the quadrupoles), otherwise the sources of coupling should be modelled and a coupled x-y analysis, that takes into account the simultaneous change in horizontal and vertical orbit, must be adopted as described in [50]. This condition is checked directly for the DAΦNE rings from the usual measurements of closed orbit response to the dipole correctors: orbit changes in one plane due to dipole kicks in the

other transverse plane must be negligible.

7.3.1 BBA analysis

The analysis algorithm has been written in Matlab and consists of:

1. download the file of the reference orbit x_{ref};
2. download the file of measured closed orbit changes x_{meas};
3. download the file of modelled closed orbit changes x_{mod};
4. for each quadrupole fit x_{meas} versus x_{mod} in a least-squares sense: $x_{meas} = k \cdot x_{mod}$;
5. $x_{bq} = k \cdot 1$ mm is the beam-to-quad offset;
6. $x_{mq} = x_{bq} + x_{ref}$ gives an assessment of the BPM-to-quad offset;

For very small kicks sizes the model converges almost to the electronic noise level of the measurements, which means the residual error in the fit is dominated by random noise. As the quadrupole strength changes increase, the optics functions and the betatron tunes of the ring change too much and the beam can be lost.

The quadrupole strength changes are chosen as a trade-off between the effective signal-to-noise of the measurements, which profits from large kicks, and the perturbation to the ring optics due to the focusing change.

Assuming typical values for a DAΦNE quadrupole $\beta = 10$ m and $x_{bq} = 1$ mm, a maximum orbit displacement of the order of 200 μm is obtained with a current variation in the quadrupole of about 2 A.

Within this range of orbit displacements the effect on the orbit due to the sextupoles is very small, so that they can be kept on during the measurements with large beam lifetime and without affecting the orbit changes. Other nonlinearities in the ring lattice

(the most important are represented by the field of the wiggler magnets) and systematic errors from the non linear response of the BPMs are completely negligible as well.

The scaling parameter of the fit k ($x_{meas} = k \cdot 1$ mm) is calculated by the alghoritm of analysis in order to minimize the deviation χ^2 between the measured orbit response and the modelled one:

$$\chi^2 = \sum_i \frac{(x_i^{meas} - kx_i^{mod})^2}{\sigma_x^2}; \tag{7.6}$$

that gives:

$$k = \frac{\sum_i (x_i^{meas} x_i^{mod})}{\sum_i x_i^{mod}}. \tag{7.7}$$

The error on x_{bq} is calculated assuming as errors on the fitted orbit changes [51]:

$$\sigma_x^2 = \sum_i \frac{1}{N} (x_i^{meas} - kx_i^{mod})^2; \tag{7.8}$$

and propagating them on k:

$$\sigma_k^2 = \frac{\sum_i (x_i^{meas} - kx_i^{mod})^2}{\sum_i (x_i^{mod})^2}. \tag{7.9}$$

The offsets between the beam positions and the quadrupole centres are thus determined with an average resolution of about 100 μm.

The assessment of the offset x_{mq} between the BPM and the centre of the adjacent quadrupole is carried out adding x_{bq} to the reference orbit value at the BPM of interest (see Fig. 7.1). The error on x_{mq} is given by the sum of all terms in Table 6.1 and the aforementioned error generated when the beam passes through the quadrupole with an angle x'. A direct measurement of the orbit slope is not possible, since two consecutive monitors would be needed between the quadrupole of interest and the following magnetic

element. However we can estimate the maximum value the angle can have all along the reference orbit as the maximum position range between two consecutive BPMs divided by their distance. Typically the worst value expected for x' will be (see for instance the reference orbits in Figures 7.4-7.7):

$$x'_{max} = 3.5mm/2m = 1.7\ mrad; \tag{7.10}$$

and multiplying x'_{max} by the distance d between the quadrupole centre and the BPM, a pessimistic estimate of the contribution to the error on x_{mq} comes out to be:

$$\delta x_{mq} = x'_{max} \cdot d = 1.7\ mrad \cdot 0.12\ m = 200\ \mu m. \tag{7.11}$$

For the quadrupoles positioned in the Long sections QUAPL103, QUAPL104, QUAPL207, QUAPL208 and QUAEL103, QUAEL104, QUAEL207, QUAEL208, which have no adjacent monitor, the BPM-to-quadrupole offset is not measured.

7.3.2 BBA results

Three sets of measurements have been performed on both rings: two with the optics for FINUDA and one with the KLOE optics. The agreement between measured orbit changes and that predicted from the model using Equations 7.4-7.5 is very good for most quadrupoles. Figure 7.3 shows as an example the agreement between the measured change in vertical orbit and the fit from the MAD model for QUAPL114. The BPM readings are averaged over 10 orbits.

There are however some quadrupoles whose orbit responses are fitted with large errors, such quadrupoles are in general positioned in the "Y" sections. Bad orbit fits are explained with non-zero local coupling at the interested quadrupole: in the "Y" sections coupling was not perfectly corrected because of the residual coupling of the adjacent interaction

	average error
Fitted orbit changes	16 μm
Beam-to-quad offsets	100 μm
BPM-to-quad offsets	300 μm

Table 7.2: Average errors obtained on the fitted orbit changes and on the measured offsets. Error on BPM-to-quad offset includes the statistical error from the fit and the error δx_{mq} from the orbit passing through the quadrupole with an angle.

region or because of the coupling generated by the "C" steering correctors used to adjust the beam trajectories through the interaction regions [6].

The existence of local coupling in the "Y" sections is confirmed also by the usual measurement of the closed orbit response to dipole correctors.

Plots and Tables in next pages summarize the results of the three sets of measurements on both rings.

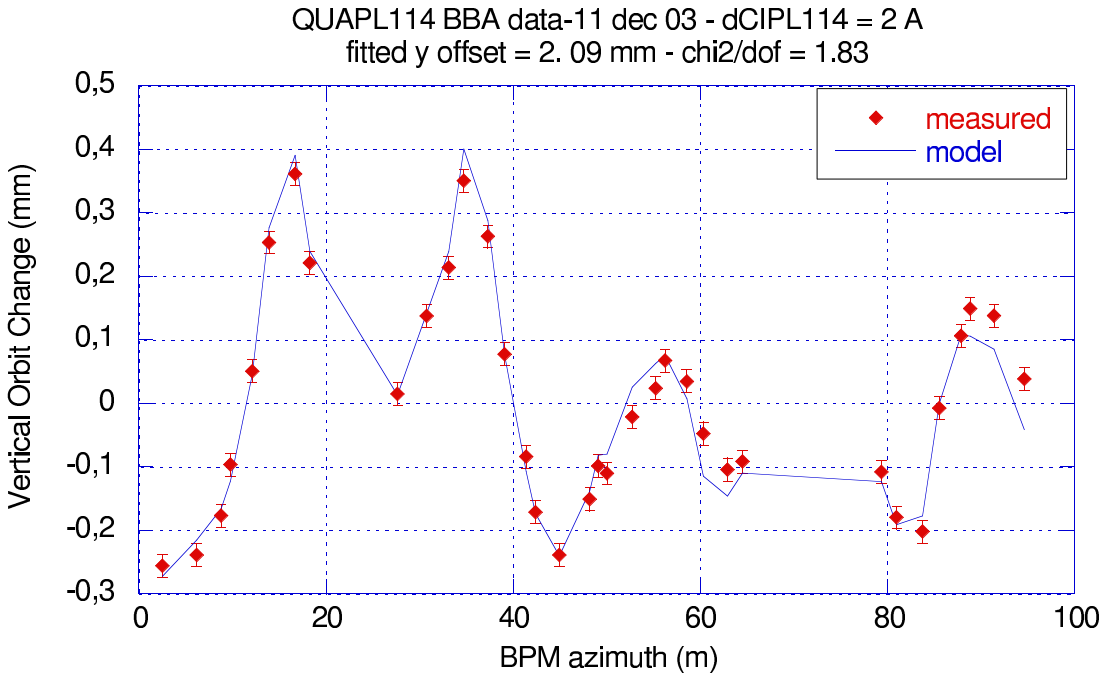

Figure 7.3: Agreement between the measured and the fitted orbit change for QUAPL114.

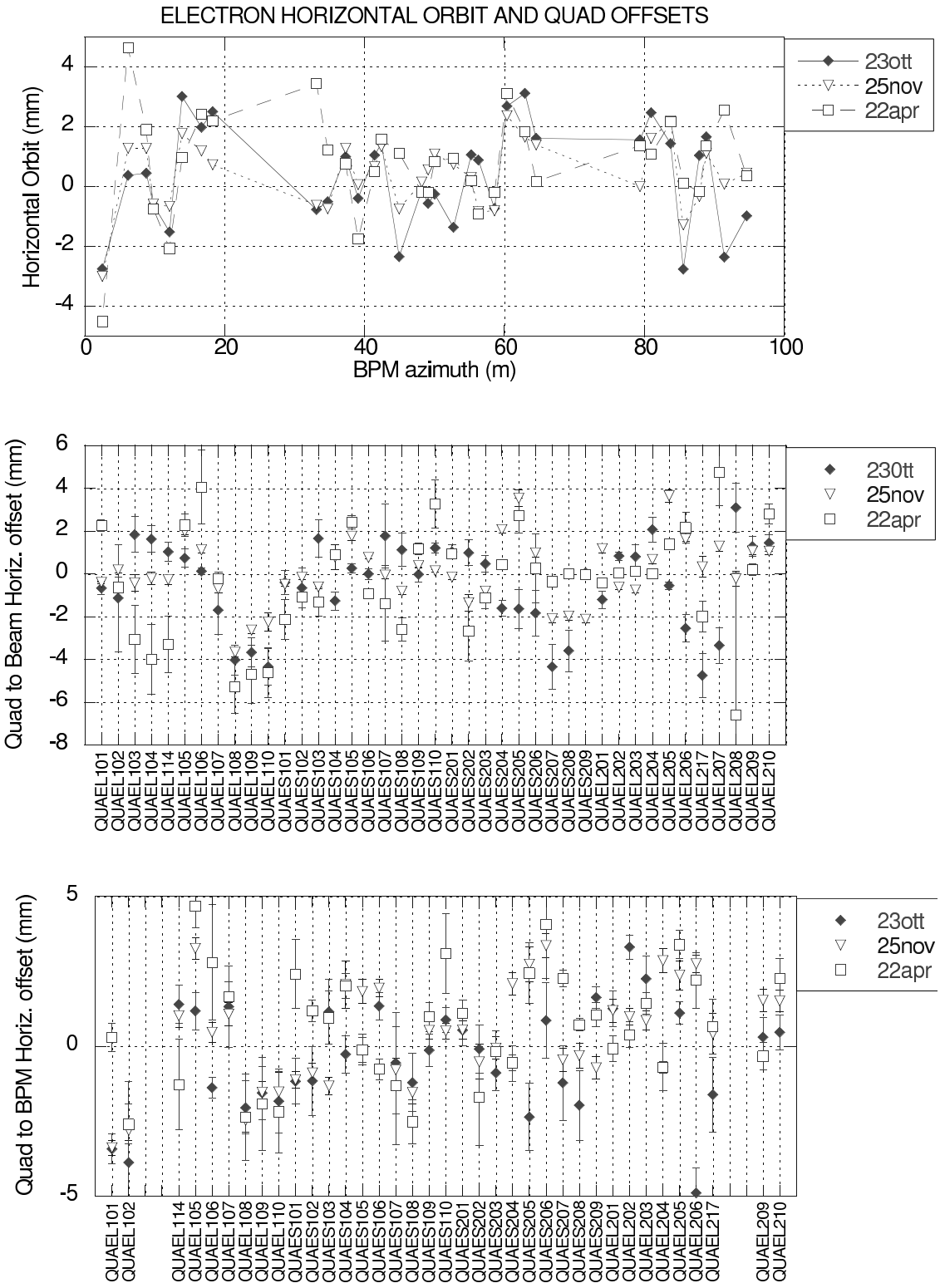

Figure 7.4: Horizontal BBA measurements in the electron ring.

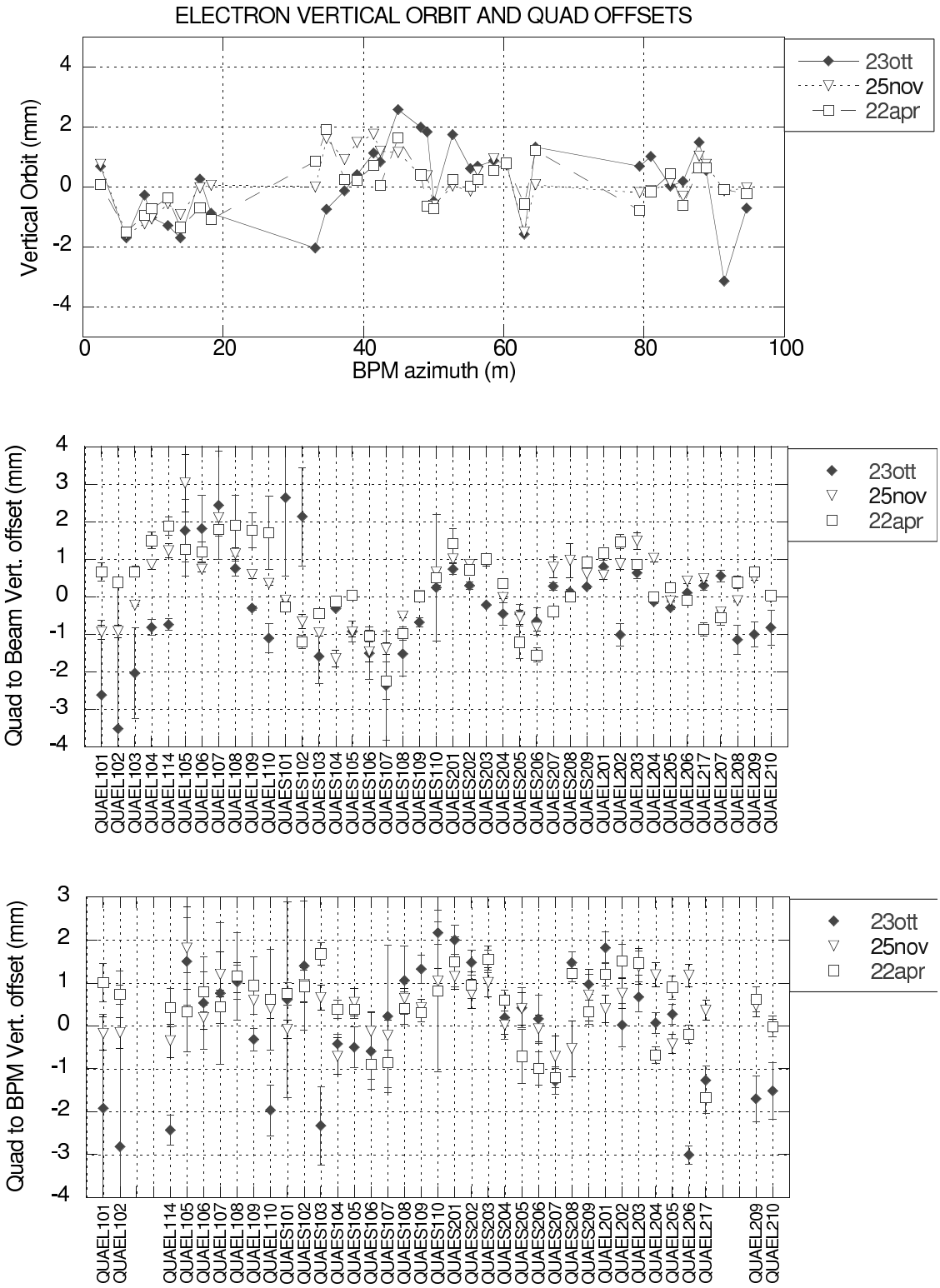

Figure 7.5: Vertical BBA measurements in the electron ring.

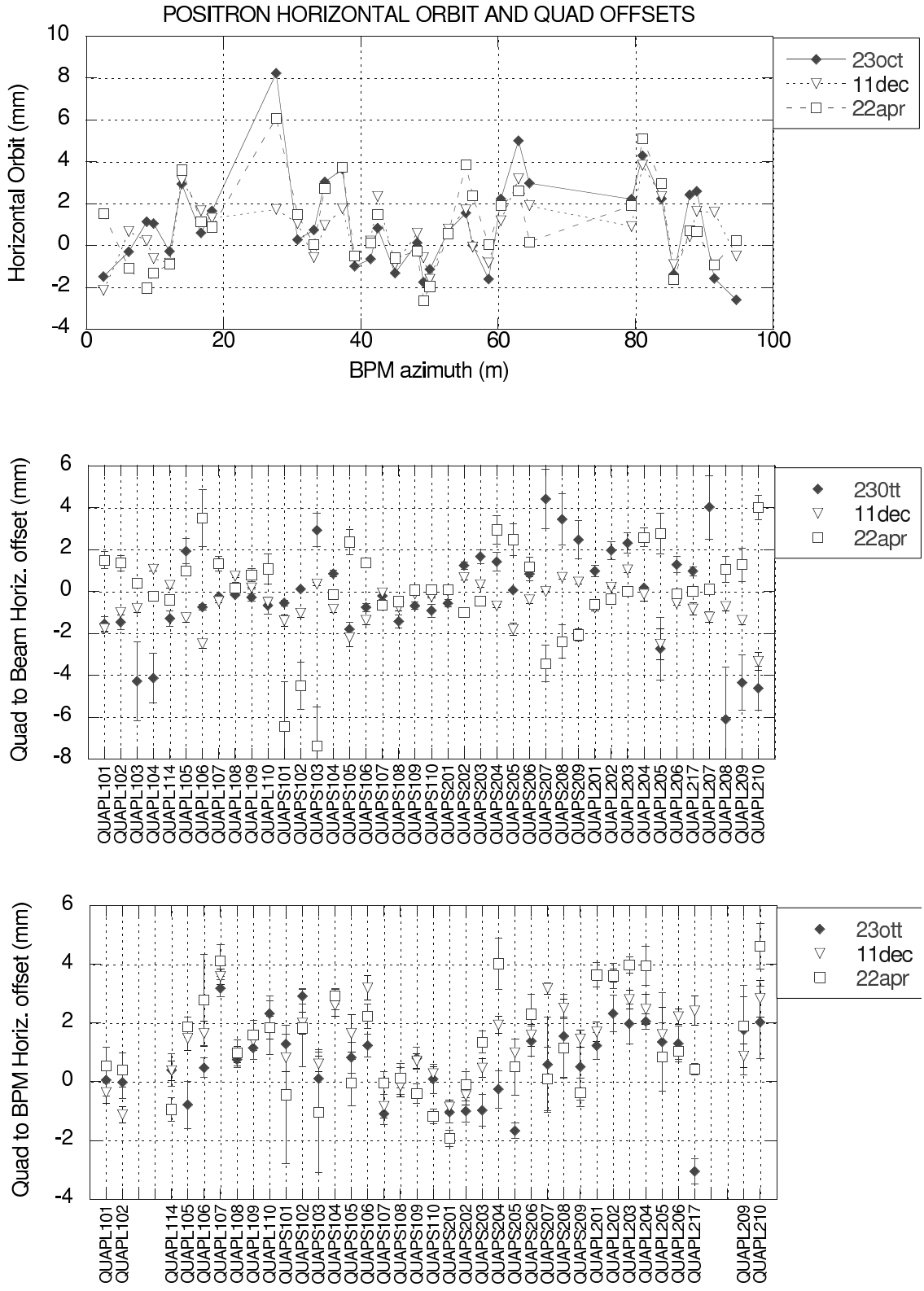

Figure 7.6: Horizontal BBA measurements in the positron ring.

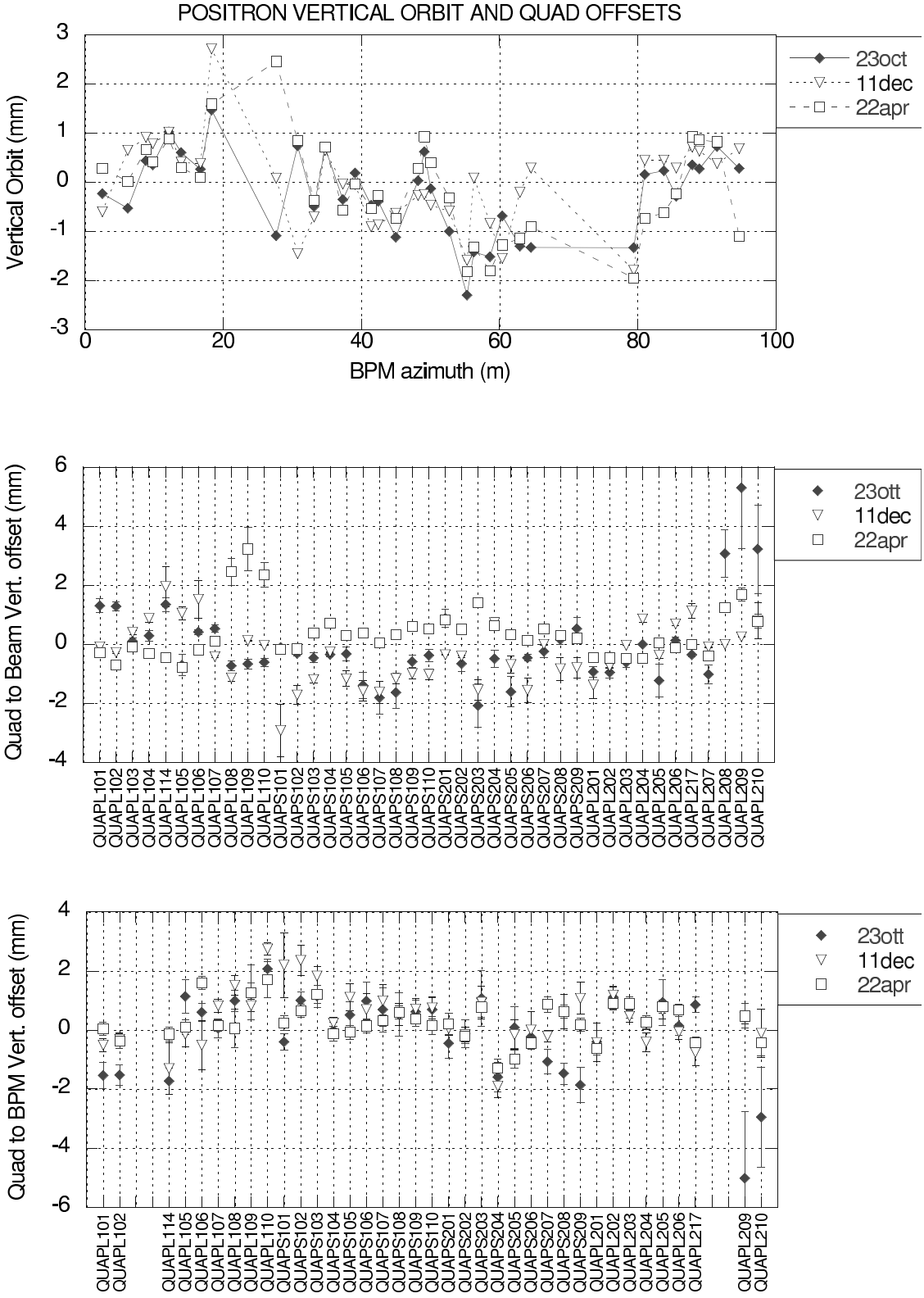

Figure 7.7: Vertical BBA measurements in the positron ring.

The first measurement was taken in September 2003 at the beginning of the FINUDA run. The BBA analysis revealed an anomalous beam to quadrupole horizontal offset of 8 mm and a vertical offset of 6 mm for QUAEL204, too large to be real misalignments. The measurement was repeated for the quadrupole of interest obtaining every time unexplainable large and different values. Inspecting directly the quadrupole, we discovered that there was a short circuit in the winding that changed the field calibration in an unpredictable way.

Generally a short circuit in a quadrupole represents a large change in the magnetic lattice that make impossible to store the beam in the ring. However this case was much subtle since the powered current in QUAPL204 was only 20 A (while typical values for DAΦNE quadrupoles are around 60-100 A) and the beam was stored even though the quadrupole was shorted and the optical functions were mismatched.

The second observation was that all the quadrupoles in the Long straight section of the electron ring had BPM-to-quadrupole vertical offsets of 2-2.5 mm. Alignment survey was then performed and confirmed that the vacuum chamber, where the BPMs are installed, was 2 mm lowered in that section [46]. In fact the Long sections were just been rearranged during the previous machine stop.

Two more BBA measurements have been taken during the run for FINUDA between October and December 2003. The comparison between these two sets of measurements shows that beam to quadrupole offsets have been reduced during the machine set-up and that the BPM to quadrupole offset measurements are reproducible until the analysis resolution for most quadrupoles. It is apparent (Fig. 7.5) that the BPM-to-quadrupole vertical offsets for the electron Long section (QUAEL101, QUAEL102, QUAEL114, QUAEL105, QUAEL106, QUAEL117, QUAEL209, QUAEL210) have been corrected from about 2 mm to less than 0.3 mm after the realignment.

Furthermore it is apparent that the quality of the fit is improved for the measurements

	r.m.s. offsets	Positron ring			Electron ring		
		23 oct	11 dec	22 apr	23 oct	25 nov	22apr
Horiz	Beam-to-quad (mm)	2.33	1.10	2.31	1.51	2.06	2.57
	BPM-to-quad (mm)	1.53	1.88	2.14	1.71	1.93	2.36
Vert.	Beam-to-quad (mm)	1.38	1.05	0.92	0.99	1.32	1.06
	BPM-to-quad (mm)	1.40	1.00	0.68	0.74	1.59	0.90

Table 7.3: Measured quadrupole offsets of the DAΦNE main rings.

taken on December, 11 due to the coupling correction during the commissioning resulting in a better accuracy of the optics model.

One further BBA measurement has been performed at the beginning of the KLOE run in april 2004. This measurement is not completely comparable with the previous ones, since several quadrupoles have been realigned in the winter shutdown.

Table 7.3 summarize the results for the different sets of measurements for both rings. The horizontal and vertical offsets and the relative error of each quadrupole for both rings are plotted in the Figures 7.4-7.7 of this Chapter.

Chapter 8

Summary

The model of the DAΦNE main rings has been updated describing the second interaction region, where the FINUDA detector was installed in 2003, and the modified wiggler magnets.

Wiggler modelling is a one of issues that are studied at presently in the accelerator community. Our choice (hard-edge model) proved to be very flexible and easy to use and gives very reliable results for all the parameters determined by the linear dynamics in differents configurations of the machine. Suitable corrections, which have been estimated, must be taken in account to calculate the synchrotron radiation integrals that determine the natural energy spread and the emittance of the main rings.

The calculation of a lattice that completely fit the numerous constraints necessary for the DAΦNE rings was performed with this new model developed for the MAD program. Once applied the calculated settings, we have verified an excellent agreement between the model predictions and the measurements of all the optics paramenters: betatron and dispersion functions, betatron tunes, emittance and closed orbits.

Concerning the beam based alignment, the introduction of a BBA procedure at DAΦNE demonstrated that this technique is a powerful diagnostic tool to find large quadrupole

misalignments. Furthermore BBA has been able to easily check the correct operation of the quadrupoles. More investigation is needed to estimate the reproducibility and the stability of these measurements.

Until now an orbit correction with the steering dipoles that takes into account the BBA results in order to determine an orbit passing close to the centres of the quadrupoles has not yet been implemented, since DAΦNE is not so demanding for the correction of spurious dispersion generated by quadrupole offsets as on the contrary will be next linear colliders.

A further development that can be implemented is a procedure of orbit correction to minimize the offsets of the beam with respect to the quadrupoles. From a calibrated lattice model we are able to calculate the response matrix between the orbit corrector magnets and the beam position in the quadrupoles. Inverting the matrix and applying to the measured beam offsets, we could determine steering changes for minimizing the beam offsets with respect to the quadrupole centres. It will likely be necessary to iterate this procedure, because effects such as coupling, beam offsets in sextupoles, spurius dispersion etc. will limit the precision with which the beam offsets in the quadrupoles may be measured. At DAΦNE there are a fewer correctors magnets (37) than there are quadrupoles (41). The matrix inversion will therefore need to be performed using singular value decomposition [38] and one can expect to minimize the beam offsets rather than steer the beam exactly to the centres.

Currently DAΦNE is running with the KLOE experiment with an optics very similar to that used for FINUDA and the machine luminosity is going better and better. The luminosity peak value has just achieved (December 2004) $1.30 \cdot 10^{32}$ $\mathrm{cm}^{-2}\mathrm{s}^{-1}$.

Acknowledgements

This work has been made possible by the support from the University of Florence and the Frascati National Laboratories (LNF) of the National Institute for Nuclear Physics (INFN). In particular I want to sincerely acknowledge Prof. Annamaria Cartacci and Dr. Sergio Bertolucci, who encouraged my partecipation to the PhD program and to the DAΦNE study, and Prof. Mario Calvetti for his wise guide and supervision. My work has been carried out at the LNF in the Accelerator Division. I would like to thank very much Dr. Caterina Biscari, supervisor of my work, for her smart suggestions, for sharing with me her knowledge and for the careful reading of my thesis.

I would like also to aknowledge the other members of the DAΦNE beam optics team. In particular, I am very grateful to Pantaleo Raimondi, for many interesting discussions and for sharing with me his experience on colliders, and to Catia Milardi, who always strongly supported my work. The wiggler modelling has been possible thanks to the fit of the multipolar components by Miro Preger, I appreciate him very much for his fruitful help.

I would like to thank all my collegues of the Accelerator Division. In this group I found an excellent environment for a student to learn. I want to mention David Alesini, Manuela Boscolo, Bruno Buonomo, Daniele Filippetto, Maurizio Incurvati, Carlo Ligi, Ruggero Ricci and many others. From the other Divisions, I want to thank Barbara Sciascia for many enjoyable discussions.

My work has taken profit from the collaboration with Mark Woodley from SLAC, who was patient enough to help me in the set-up of the beam based alignment analysis.

I cannot avoid mentioning Simone Di Mitri, we worked together during our graduate thesis at Frascati, and I know that I can call him at Trieste for any problem on accelerator physics every time I need.

My family has always been close to me and supported me since I left Florence to come in Rome. I want to sincerely thank Angela (mamma), Giovanni, Sara, David and Angelo.

I conclude thanking my friends Chiara, Diego, Goffredo, Manuela, Michele, Dario and Alessia. They made my staying in Rome so enjoyable and I feel at home when I am with them.

And many thanks to Maria Velia, for the happiness she gives me by staying by my side.

Bibliography

[1] D. Alesini, M.E. Biagini, A. Gallo, P. Raimondi, and M. Zobov. *Estimate of Hourglass Effect in DAΦNE*. Dafne Technical Note G-62, 2004.

[2] M. Bassetti, C. Biscari, and M. Preger. *Optical characteristics of the DAΦNE wiggler*. Dafne Technical Note G-27, 1994.

[3] M. Bassetti and G.A. Erskine. *Close Expression for the Eletrical Field of a Two-Dimentional Gaussian Charge*. CERN-IRS-Th/80-06, 1980.

[4] M. Bassetti et al. *DAΦNE Interaction Region Design*. Proceedings of the 1993 Particle Accelerator Conference, Washinton, D.C., pag. 2048-2051. IEEE, 1993.

[5] G. Benedetti. *Il Modello dell'Ottica di DAΦNE*. Graduate Thesis at the Università di Firenze, 2001.

[6] G. Benedetti. *Sextupole in the "C" Corrector Magnet*. Dafne Technical Note BM-5, 2001.

[7] C. Biscari. *Quadrupole Modelling*. Dafne Technical Note L-25, 1996.

[8] C. Biscari. *Detuned Lattice for DAΦNE Main Rings*. Dafne Technical Note L-32, 2001.

[9] C. Biscari. *First results of Luminosity on the detuned lattice*. Dafne Technical Note BM-6, 2001.

[10] C. Biscari. *Linear Optics Model for DAΦNE Main Rings*. Dafne Technical Note L-33, 2001.

[11] C. Biscari. *Half β_x^* at IP2*. Dafne Technical Note BM-9, 2002.

[12] C. Biscari et al. *Measurements on TESLA splitter prototype for the DAΦNE Main Rings*. Dafne Technical Note MM-20, 1996.

[13] B. Bolli et al. *The "long" dipoles of the DAΦNE Main Rings achromats*. Dafne Technical Note MM-25, 1996.

[14] B. Bolli et al. *The "short" dipoles of the DAΦNE Main Rings achromats.* Dafne Technical Note MM-19, 1996.

[15] B. Bolli et al. *The Large Aperture Quadrupole Prototype for the DAΦNE Interaction Regions.* Dafne Technical Note MM-22, 1997.

[16] B. Bolli et al. *Magnetic measurements on the four splitters prototype of the DAΦNE interaction regions.* Dafne Technical Note MM-28, 1997.

[17] M. Boscolo. *Beam-beam Interaction Effects in DAΦNE.* PhD. Thesis at the Università di Roma "La Sapienza", 2000.

[18] A. Chao. *Physics of Collective Beam Instabilities in High Energy Accelerators*, page 371. Wiley, 1993.

[19] DEAR collaboration. *The DEAR case.* Riv. del Nuovo Cimento, Vol. 22, N. 11, 1999.

[20] FINUDA Collaboration. *FINUDA, a detector for nuclear physics at DAΦNE.* LNF-93/021, 1993.

[21] KLOE Collaboration. *KLOE, a general Purpose Detector for DAΦNE.* LNF-92/109, 1993.

[22] M. Conte and W.W. MacKay. *Physics of Particle Accelerators.* World Scientific, 1991.

[23] E.D. Courant and H.S. Snyder. *Theory of the Alternating-Gradient Syncrotron.* Annals of Physics 3, Vol. 1, 1958.

[24] M.A. Furman. *The Hourglass Reduction Factor for Asymmetric Colliders.* SLAC-ABC-41-REV, 1991.

[25] A. Ghigo et al. *DAΦNE Beam Instrumentation.* Beam Instrumentation Workshop, Stanford 1998,pag. 183-190. AIP, 1998.

[26] H. Grote and F.C. Iselin. *The MAD Program, User's Reference Manual.* CERN/SL/90-13(AP), 1996.

[27] S. Guiducci and M. Preger. *Calibration constants and nominal set points for the Day-One lattice of the DAΦNE Main Rings.* Dafne Technical Note C-18, 1997.

[28] R. H. Helm, M. J. Lee, P. L. Morton, and M. Sands. *Evaluation of Synchrotron Radiation Integrals.* IEEE Trans. Nucl. Sc., NS-20, 1973.

[29] K. Hirata. *Beam-beam Interaction with a Crossing Angle.* KEK-93-190, 1994.

[30] F.C. Iselin. *The MAD Program, Physical Methods Manual.* CERN/SL/92(AP), 1994.

[31] F. Iungo et al. *DAΦNE Magnetic Measurements System.* Dafne Technical Note MM-1, 1993.

[32] S.Y Lee. *Accelerator Physics.* World Scientific, 1999.

[33] C. Milardi et al. *Effects of Nonlinear Terms in the Wiggler Magnets at DAΦNE.* PAC2001 - Chicago, 2001.

[34] C. Milardi et al. *Developments in Linear and Non-Linear DAΦNE Lattice.* PAC03, Portland, Oregon, 2003.

[35] A. Piwinski. *Storage Ring Luminosity as a Function of Beam to Beam Space and Crossing Angle.* SLAC-TRANS-0067, 1969.

[36] M. Preger et al. *Magnetic Measurements on the Permanent Magnet Quadrupoles of the FINUDA Interaction Region.* Dafne Technical Note MM-32, 2000.

[37] M. Preger et al. *The Modified Wiggler of the DAΦNE Main Rings.* Dafne Technical Note MM-34, 2004.

[38] W.H. Press et al. *Numerical Recipes (Fortran).* Cambridge, 1989.

[39] M. Ross et al. *Beam Based Alignment at the KEK Accelerator Test Facility.* EPAC02, Paris, France, 2002.

[40] J. Safranek et al. *Non Linear Dynamics in a SPEAR Wiggler.* Phys. Rev. Vol. 5, 010701, 2002.

[41] M. Sands. *The Physics of Electron Storage Rings.* SLAC Report 121, 1970.

[42] C. Sanelli et al. *DAΦNE Magnet Power Supply System.* EPAC98, Stockolm, 1998.

[43] J.T. Seeman. *Observations of the Beam-beam Interaction.* SLAC-PUB-3825, 1985.

[44] A. Stella. *Analysis of the DAΦNE Beam Position Monitors with a boundary elements method.* Dafne Technical Note CD-10, 1997.

[45] A. Stella et al. *Beam Position Monitor System of DAΦNE.* Beam Instrumentation Workshop, Stanford 1998,pag. 378-386. AIP, 1998.

[46] DAΦNE Team. *DAΦNE logbook, March 24-25, 2001.* LNF-INFN.

[47] G. Vignola et al. *The Φ-Factory Storage Rings.* pag. 325-364. LNF-90/031(R), 1990.

[48] G. Vignola et al. *DAΦNE, Design Criteria and Project Overview.* Workshop on Physics and Detectors for DAΦNE, Frascati, pag. 11-27. LNF-INFN, 1991.

[49] H. Wiedemann. *Particle Accelerator Physics.* Springer-Verlag, 1999.

[50] A. Wolski and F. Zimmermann. *Closed Orbit Response to Quadrupole Strength Variation.* LBNL-54360, 2004.

[51] M. Woodley et al. *Beam Based Alignment at the KEK-ATF Damping Ring.* EPAC04, Lucerne, Switzerland, 2004.

[52] F. Zimmermann. *Measurements and Correction of Accelerator Optics.* Proceedings of the 1998 Joint US-CERN-Japan-Russia School on Particles Accelerators, Montreux, pag. 17-20. World Scientific, 1999.

[53] M. Zobov et al. *Bunch Lengthening and Microwave Instability in the DAΦNE Positron Ring.* e-Print Archive: physics/0312072.

[54] M. Zobov and K. Hirata. *Beam-beam Interaction Study for DAΦNE.* EPAC96, Sitges, Barcelona, 1996.

Appendix A

Transport matrices of the magnetic elements

When a particle with position vector $(x_0, x_0'; y_0, y_0', t_0, \delta_0)$ at a given azimuth s_0, goes through a sequence of magnetic elements up to the azimuthal position s, each element can be described by means of a matrix 6×6, which transform the position vector before the element in the the vector after it.

The transport matrix from s_0 to s will be the product of the matrix of the sigle elements:

$$M(s, s_0) = M(s, s_n)M(s_n, s_{n-1}) \cdots M(s_1, s_0) \tag{A.1}$$

The form of the representative matrices of the different types of magnetic elements are reported [22, 30]; those matrices are obtained calculating the solution of the Hill equation which describes betatron oscillations.

Drift section of length L:

$$M_{drift} = \begin{pmatrix} 1 & L & 0 & 0 & 0 & 0 \\ 0 & 1 & 0 & 0 & 0 & 0 \\ 0 & 0 & 1 & L & 0 & 0 \\ 0 & 0 & 0 & 1 & 0 & 0 \\ 0 & 0 & 0 & 0 & 1 & 0 \\ 0 & 0 & 0 & 0 & 0 & 1 \end{pmatrix}. \tag{A.2}$$

It leaves invaried the slope z' and increases the displacement z by $z'L$.

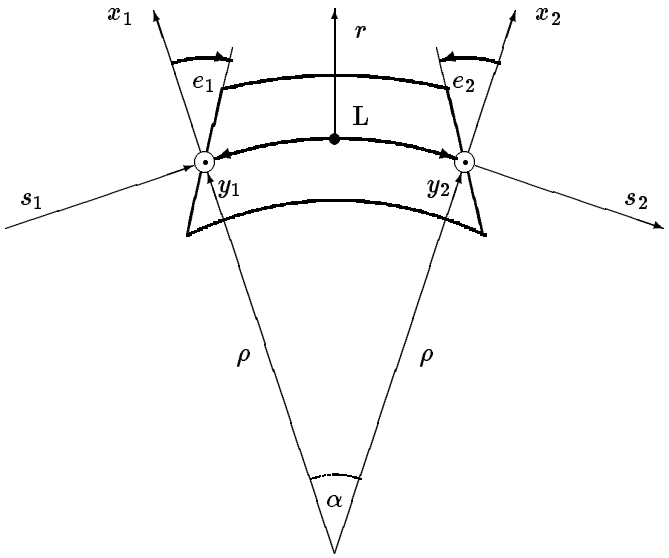

Figure A.1: Reference system fot a bending magnet.

Dipoles: for a dipole the contribution to the dispersion due to the energy deviations of the particle must be considered. The transport matrix of a bending dipole consists of three terms: the fringing field at the magnet entrance F_1, the body of the dipole B and the fringing field at the magnet exit F_2:

$$M_{bend} = F_1 B F_2 \tag{A.3}$$

The pole-face roation angles determine the focusing effects of the fringing and are denoted with e_1 and e_2 (Fig. A.1).

In a sector dipole helds $e_1 = e_2 = 0$, while in a rectangular dipole $e_1 = e_2 = \alpha/2$.

If the fringing have finite extension the focusing angle in the vertical matrix element is changed:

$$\overline{e}_i = e_i - hgI_1(1 + \sin^2 e_i) \tag{A.4}$$

where h is the orbit curvature through the dipole, g is the magnetic gap, e I_1 the first integral of the fringing field (called *fint*):

$$fint = I_1 = \int_{-\infty}^{+\infty} \frac{B_y(s)(B_0 - B_y(s))}{g \cdot B_0^2} ds \tag{A.5}$$

The entrance/exit transport matrix is then:

$$F_i = \begin{pmatrix} 1 & 0 & 0 & 0 & 0 & 0 \\ h\tan e_i & 1 & 0 & 0 & 0 & 0 \\ 0 & 0 & 1 & 0 & 0 & 0 \\ 0 & 0 & -h\tan \overline{e}_i & 1 & 0 & 0 \\ 0 & 0 & 0 & 0 & 1 & 0 \\ 0 & 0 & 0 & 0 & 0 & 1 \end{pmatrix} \tag{A.6}$$

which corresponds to a thin lens with focal length $f = \rho \cot e_i$.

The magnet body with angle and curvature ρ e α and uniform field has transport

matrix:

$$B = \begin{pmatrix} \cos\alpha & \rho\sin\alpha & 0 & 0 & 0 & \rho(1-\cos\alpha) \\ -\frac{1}{\rho}\sin\alpha & \cos\alpha & 0 & 0 & 0 & sin\alpha \\ 0 & 0 & 1 & \rho\alpha & 0 & 0 \\ 0 & 0 & 0 & 1 & 0 & 0 \\ -\sin\alpha & -\rho(1-\cos\alpha) & 0 & 0 & 1 & -\rho(\alpha-\sin\alpha) \\ 0 & 0 & 0 & 0 & 0 & 1 \end{pmatrix} \tag{A.7}$$

In the bending plane gives a focusing contribution due to a geometric effect of the magnet: the trajectories entering closer to the centre of curvature travel a shorter stretch of the magnet and are thus less bent, the converse occurs entering more distant to the centre of curvature. In the vertical plane it acts as a drift section of length $\rho\alpha$.

Quadrupole F (horizontal focusing and vertical defocusing) of strength $k^2 = \frac{ec}{E_0}\frac{\partial B_y}{\partial x}$ and length L:

$$M_F = \begin{pmatrix} \cos(kL) & \frac{1}{k}\sin(kL) & 0 & 0 & 0 & 0 \\ -k\sin(kL) & \cos(kL) & 0 & 0 & 0 & 0 \\ 0 & 0 & \cosh(kL) & \frac{1}{k}\sinh(kL) & 0 & 0 \\ 0 & 0 & -k\sinh(kL) & \cosh(kL) & 0 & 0 \\ 0 & 0 & 0 & 0 & 1 & 0 \\ 0 & 0 & 0 & 0 & 0 & 1 \end{pmatrix} \tag{A.8}$$

while if $\frac{\partial B_y}{\partial x}$ is negative, the quadrupole is D (horizontal defocusing and vertical focusing) and the trigonometric functions and the hiperbolic ones are exchanged in matrix elements. In the *thin lens* approximation (i.e. $kL \ll 1$ con $L \to 0$ e k^2L constant) the matrix come

out to be:

$$M_{F,D} = \begin{pmatrix} 1 & 0 & 0 & 0 & 0 & 0 \\ \mp k^2 L & 1 & 0 & 0 & 0 & 0 \\ 0 & 0 & 1 & 0 & 0 & 0 \\ 0 & 0 & \pm k^2 L & 1 & 0 & 0 \\ 0 & 0 & 0 & 0 & 1 & 0 \\ 0 & 0 & 0 & 0 & 0 & 1 \end{pmatrix} = \begin{pmatrix} 1 & 0 & 0 & 0 & 0 & 0 \\ \mp \frac{1}{f} & 1 & 0 & 0 & 0 & 0 \\ 0 & 0 & 1 & 0 & 0 & 0 \\ 0 & 0 & \pm \frac{1}{f} & 1 & 0 & 0 \\ 0 & 0 & 0 & 0 & 1 & 0 \\ 0 & 0 & 0 & 0 & 0 & 1 \end{pmatrix} \tag{A.9}$$

where f is the focal length of the lens.

Skew quadrupole: when a quadrupole is tilted by an angle θ around the longitudinal axis:

$$M_{quad}(\theta) = R(\theta) M_{quad} R^{-1}(\theta) \tag{A.10}$$

where M_{quad} is matrix of an upright quadrupole and $R(\theta)$ represents a rotation in the transverse plane x, y e x', y' by an angle θ:

$$R(\theta) = \begin{pmatrix} \cos\theta & 0 & \sin\theta & 0 & 0 & 0 \\ 0 & \cos\theta & 0 & \sin\theta & 0 & 0 \\ -\sin\theta & 0 & \cos\theta & 0 & 0 & 0 \\ 0 & -\sin\theta & 0 & \cos\theta & 0 & 0 \\ 0 & 0 & 0 & 0 & 1 & 0 \\ 0 & 0 & 0 & 0 & 0 & 1 \end{pmatrix} \tag{A.11}$$

Solenoid of strength $k_s = \frac{1}{2}\frac{ec}{E_0}B_s$ and length L:

$$M_{sol} = \begin{pmatrix} \cos(k_s L)Q & \sin(k_s L)Q & 0 & 0 \\ -\sin(k_s L)Q & \cos(k_s L)Q & 0 & 0 \\ 0 & 0 & 1 & 0 \\ 0 & 0 & 0 & 1 \end{pmatrix} \tag{A.12}$$

where Q is a 2×2 matrix focusing quadrupole-like:

$$Q = \begin{pmatrix} \cos(k_s L) & \frac{1}{k_s}\sin(k_s L) \\ -k_s \sin(k_s L) & \cos(k_s L) \end{pmatrix} \tag{A.13}$$

Thus a solenoid acts focusing in both planes and rotating the beam by an angle $k_s L$.